Surface Forces and Structures in Complex Electrolytes

A thesis presented for the degree of

Doctor of Philosophy



Timothy S. Groves

Physical and Theoretical Chemistry

Worcester College

University of Oxford

6st December 2023

Declaration

This thesis is submitted for the degree of Doctor of Philosophy in Physical and Theoretical Chemistry at the University of Oxford. I confirm that the work presented here is my own. Where information has been derived from other sources, I confirm that this has been indicated in the thesis.

One of the surface force measurements at 4.5 mol kg^{-1} detailed in chapter 3 were performed as part of my masters project in Physical and Theoretical Chemistry at the University of Oxford, in collaboration with Dr Romain Lhermerout. Neutron scattering measurements described in chapter 4 were performed alongside Dr Tom Headen at ISIS Neutron and Muon Source, and in collaboration with Dr James Hallett and Kieran Agg. In all cases, the experiments were devised by the author, and all data analysis and interpretation is the author's own work.

Abstract

Electrolytes, environments in which ions are free to move, are found throughout the natural and the human-centred world. The biochemistry that allows for life, alongside many of the innovations that make modern life so convenient, rely on the physical chemistry of these substances. Despite this, the behaviours of many complex and high concentration electrolytes are relatively poorly understood. This thesis investigates the forces and structures present in three examples of complex, high concentration electrolytes in order to better the understanding of these fascinating systems.

First, we present measurements of surface forces present in water-in-salt electrolytes, high concentration aqueous electrolytes with potential applications in next generation energy storage devices. We find evidence for a layered structure of aqueous and non-aqueous domains within the confined electrolyte films. These domains are maintained in the bulk liquid, and our analysis of the clustering of the domains suggests consequences for the mechanism of ion transport in water-in-salt electrolytes. We also studied ionic liquids, liquid electrolytes consisting solely of ions. We show that different layered structures can form in ionic liquids confined between surfaces, where the structure adopted depends on the nature of the ions. On studying mixtures of ionic liquids that form different interfacial structures, we find that the mathematical expressions describing the mixtures can be written as a linear combination of the terms describing pure ionic liquids. These results have important implications for the interpretation of correlation lengths within liquid mixtures, and for the optimisation of surface properties by creating liquid mixtures. Finally, we investigate the modifications of sur-

face forces that occur in the presence of the high-concentration protein denaturant guanidinium chloride. We find varying behaviour across a broad concentration range that suggests strong time and concentration dependence in the action of guanidinium chloride at protein surfaces.

Together, the results of this thesis highlight the complexities of high concentration and poorly understood electrolyte solutions, and shed light on their interactions and behaviours. This work will be important in fully understanding the role these complex systems play, both in the devices and conveniences that allow modern life to function, and in the complex chemistries that govern life at a molecular level.

Acknowledgements

This thesis was only possible because of the work of a whole host of people supporting me along the way, so a massive thank you to all of you for your patience, support, trust, advice, genuine help, friendship, tea, pub trips, zoom quizzes, early morning online Catan sessions, and much much more. Your contributions have been invaluable.

First off, I'd like to thank my supervisor Professor Susan Perkin for her unwavering support, limitless enthusiasm and extraordinary insight. It would of course be untrue to say I have enjoyed every minute, I am sure every PhD comes with its ups and downs, but you have re-inspired me in the lows and ridden the highs alongside me. It has been an absolute pleasure to work in your lab, both as a Part II student and as a PhD student, and I look forward to continuing to do so as a post doctoral researcher.

Next up, I must thank the Doctors Romain Lhermerout, Carla Perez-Martinez, James Hallett, Catherine Fung, and Shurui Miao. Romain, you got me started, and got me so enthusiastic in SFB experiments that I've just signed up to do another two years on top of the one I did with you and the four that made up my PhD. J'espere que la prochaine fois qu'on se retrouve, je peux parler avec toi en français! Carla, you taught me so much about the ins and the outs of our technique and our lab! I'm so glad we've stayed friends and I'm always looking forward to our next coffee morning. James, thank you so much for all your help in getting the neutron scattering stuff out of the starters box, I'm excited to continue working on it together! Catherine, your knowledge and advice at sticking points in my research have been exceptionally helpful and are always appreciated. Shurui, thanks for all your counsel

on writing up bits and bobs about neutron scattering, for working your Python magic and providing a sane and knowledgeable second pair of eyes. Many thanks also to the team at ISIS for our fun little school trips there, in particular Dr Tom Headen and Dr Tristan Youngs, without whom chapter 4 would have been much less interesting.

Hannah, Kieran and Astrid, it's been great to work alongside you guys as a fellow PhD student. You've always had a helpful word, an excellent joke, and a top tier tip (even if it is just 'have you tried turning it off and on again?'). It's been a riot to get to know and distract you guys, and I shall maintain our ritual of doing the crossword as long as I can. Thanks also to all the others who've made up the research group such a fun place to work, hang out, and distract colleagues: Aurora, Weichao, Lauriane, Ilaria, Alex, Rachel, Josie, Daniel, Louis, and Xiaoyue.

Everyone who makes the PTCL so welcoming and keeps it running smoothly, in particular Paul and Leigh. Without all your hard work, nothing in this building could possibly get done.

Thanks to all my friends, both at Uni and at home. The opportunities to relax with you guys are worth more than your weight in gold. I have special shout-outs to the Fajitamigos and the grizzled veterans of Sammij and Amsterdam. Erin, I hope you regain some motion in your finger one day soon!

Finally, thanks to my family. Mum and Dad, you guys are great. Alex, Matt and David, I'm bound to win at Catan one of these days so watch this space!

Contents

Declaration iii

Abstract v

Acknowledgements vii

Table of Contents x

1 Introduction 1
- 1.1 Intermolecular Interactions and Forces . . . 1
  - 1.1.1 Dispersion Forces in Dielectric Media . . . 2
  - 1.1.2 Interactions between Ions . . . 4
  - 1.1.3 DLVO Theory and Surface Interactions in Electrolytes 6
  - 1.1.4 Non-DLVO Forces and Structural Forces . . . 8
- 1.2 Complex and Concentrated Electrolytes . . . 9
  - 1.2.1 Water-in-Salt Electrolytes . . . 10
  - 1.2.2 Ionic Liquids and Ionic Liquid Mixtures . . . 11
  - 1.2.3 Molecular Ion Denaturants and Guanidinium Chloride 11
- 1.3 Surface Forces Measurement Techniques . . . 12
  - 1.3.1 The Atomic Force Microscope . . . 12
  - 1.3.2 The Surface Force Balance . . . 13
- 1.4 Bulk Structure Measurement Techniques . . . 14
  - 1.4.1 Scattering Experiments . . . 15
  - 1.4.2 Computer Simulations . . . 15
- 1.5 Overview . . . 17

2 Experimental Methods 18
- 2.1 Surface Force Measurements . . . 18
  - 2.1.1 Surface Properties and Preparation . . . 20
  - 2.1.2 Derjaguin Approximation . . . 23
  - 2.1.3 Lens Mounts and Motion . . . 23
  - 2.1.4 Optical Pathway and Image Analysis . . . 27
  - 2.1.5 Force Profiles . . . 30
  - 2.1.6 Experimental Error Analysis . . . 34
- 2.2 Bulk Measurements . . . 38
  - 2.2.1 Neutrons and Neutron Production . . . 38
  - 2.2.2 Diffraction and Neutron Scattering . . . 42
  - 2.2.3 The NIMROD Instrument . . . 47
- 2.3 Additional Measurements . . . 48
  - 2.3.1 Refractive Indices . . . 49
  - 2.3.2 Densities . . . 50

3 Surface Forces in a Water-in-Salt Electrolyte 52
3.1 Background and Motivation 52
3.1.1 Aqueous Lithium-Ion Batteries 53
3.1.2 Water-in-Salt Electrolytes at Interfaces 54
3.2 Experimental Details 55
3.2.1 Materials and Solution Preparation 55
3.2.2 Refractive Indices 57
3.3 Surface Forces Measurements and Discussion 57
3.3.1 Fitting Normal Force Profiles 59
3.3.2 Structural Forces 62
3.3.3 Long Range Forces 68
3.4 Summary 70

4 Bulk Structure of a Water-in-Salt Electrolyte 71
4.1 Experimental Details 73
4.1.1 Materials and Solution Preparation 73
4.1.2 Empirical Potential Structure Refinement and the Dissolve Package 74
4.1.3 Densities 76
4.1.4 Dissolve Model Details 77
4.2 Bulk Structure Measurements and Discussion 77
4.2.1 Interactions in the bulk liquid 81
4.2.2 Cluster Analysis 89
4.2.3 Void Analysis 96
4.3 Summary 101

5 Oscillatory Forces in Ionic Liquid Mixtures 102
5.1 Background and Motivation 103
5.1.1 Designer Ionic Liquids 103
5.1.2 Ionic Liquid Structure 104
5.1.3 Mixtures of Ionic Liquids 105
5.2 Experimental Details 107
5.2.1 Material and Mixture Preparation 108
5.2.2 Refractive Indices 108
5.3 Pure Ionic Liquids - Measurements and Discussion 109
5.3.1 Fitting Pure Ionic Liquid Force Profiles 110
5.3.2 Forces in Pure Ionic Liquids 112
5.3.3 Non-equilibrium Structural Transitions 119
5.4 Ionic Liquid Mixtures - Measurements and Discussion 121
5.4.1 Fitting Structural Forces 126
5.4.2 Long Range and Total Forces 130
5.5 Summary 132

6 Guanidinium Ions at Charged Surfaces 134
6.1 Background and Motivation 134
6.1.1 The Guanidinium Ion and Guanidinium Chloride 135
6.1.2 Behaviour of Guanidinium Chloride 138

6.2 Experimental Details 140
6.2.1 Materials and Solution Preparation 140
6.2.2 Refractive Indices 141
6.3 Surface Force Measurements and Discussion 141
6.3.1 1-2 molal GdmCl 143
6.3.2 2-4.5 molal GdmCl 146
6.3.3 6 molal GdmCl 148
6.3.4 Interpretation of Forces 150
6.4 Summary 155

7 Conclusions and Outlook **157**

Bibliography **162**

1 | Introduction

The interactions within liquids are complex, diverse, and critical to life on this planet. For countless generations, evolutionary pressures have utilised these forces to design replicating molecules, organise them into complex structures and organelles, and sustain biochemical life[1]. More recently, research and investigation by modern humans into these interactions has lead to developments across a wide spectrum of fields, including in medicine, such as advances in drug design and delivery[2,3]; in energy storage, where interactions between ions and electrodes play a critical role[4]; and even in astronomy, where the study of extraterrestrial water is revealing the processes through which solar systems form[5].

This thesis aims to continue and build upon this tradition of studying and understanding interactions within liquids by investigating the interactions present in the complex and poorly understood regime of high concentration electrolytes. In such liquids, high ion densities and low solvent concentrations mean that non-ideal effects can dominate, giving rise to varied and intricate behaviours. The interactions between surfaces across thin films of high concentration electrolyte will be studied, and related to the behaviour of these systems in the bulk. This chapter will introduce some of the wider themes studied, and provide a background upon which the rest of the work is built.

1.1 | Intermolecular Interactions and Forces

Whether uncharged or charged, stationary or mobile, the interactions between molecules essentially all arise from electrostatic forces[6]. This means that, if the electron distribution about any pair of molecules

was known exactly, then their interactions could also be solved exactly. However, for systems containing many electrons, it is not possible to obtain an exact solution for electron distributions. As such, intermolecular interactions are often separated into many different classes which may be measured and described in different ways, and are treated as individual components in the total interaction potential.

1.1.1 | Dispersion Forces in Dielectric Media

Perhaps the simplest case of intermolecular interactions is between two isolated, uncharged molecules in a vacuum. In this case, the only mechanisms by which the molecules can interact are through steric effects, or an asymmetric charge distribution. Steric interactions arise from quantum and electrostatic effects that prevent the electron clouds about atoms and molecules from overlapping. The resulting repulsion is very short ranged, and prevents atoms from coming into contact. Interactions between asymmetric charge distributions, or dipoles, give rise to longer range forces. These interactions may be between two permanent dipoles, a permanent dipole and an induced dipole, or between two induced dipoles. In each case, as long as the dipoles are free to rotate, the interactions follow a simple pair potential, $w(r)$:

$$w(r) \propto -\frac{1}{r^6} \tag{1.1}$$

where r is the separation between the dipoles. Together, these interactions are known as the Van der Waals interaction, after Johannes Diderik van der Waals, and occur between all atoms and molecules, regardless of charge. Note the negative sign in equation 1.1: the Van der Waals interaction between any atom or molecule with any other in a vacuum is always attractive.

This pair potential provides a pathway to find the interaction energy U between macroscopic objects: simplistically, we can sum the pair interactions between a single molecule with each molecule in a surface, which gives a $U \propto -1/r^3$ dependence. Continuing this argument further leads to the prediction that $U \propto -1/r^2$ for two planar macroscopic surfaces, and that $U \propto -1/r$ for a macroscopic sphere interacting with a surface. These interactions are shown in figure 1.1. This simple calculation shows that forces arising from the Van der Waals interaction can act over a range of length scales, from the short range r^{-6} interaction between single molecules, to a relatively long range r^{-1} dependence between large spheres and surfaces. More rigorously, the interactions between macroscopic bodies are not so trivially related to the pair potentials between isolated molecules. Nonetheless, these scaling arguments still yield experimentally verifiable distance dependences that become longer and longer ranged as more molecules are taken into account.

Once these systems are immersed in a dielectric medium, the pic-

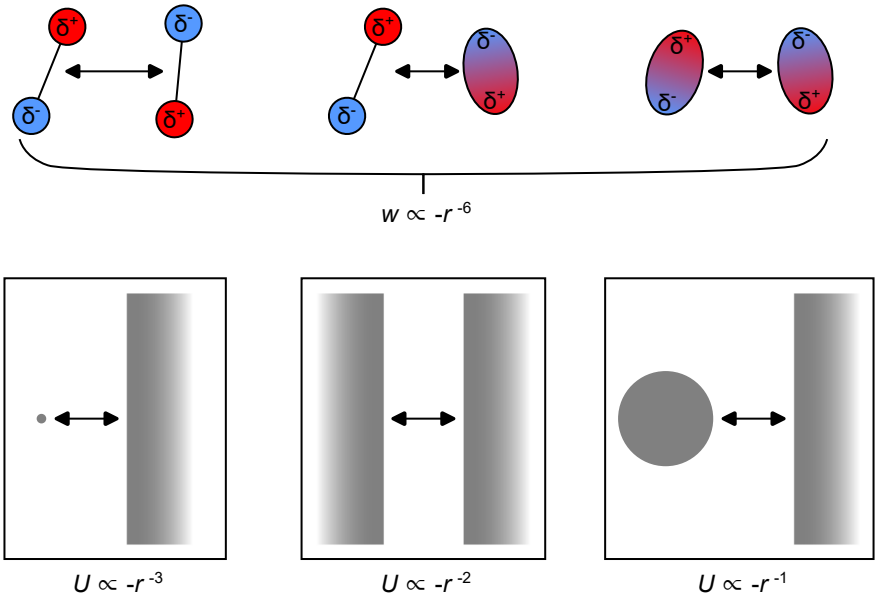


Figure 1.1: Varying separation dependence of Van der Waals interactions.

ture becomes more complex. The presence of multiple pair potentials between the two surfaces and between each surface with the solvent can lead to competing interactions. Whilst the Van der Waals attractions between two like surfaces remain always attractive, competition with solvent molecules can mean that Van der Waals forces are not always attractive between surfaces of different material.

1.1.2 | Interactions between Ions

The presence of full ionic charges adds further electrostatic interactions to the picture. For an isolated pair of ions in a dielectric medium, the interaction force between two ions is given by Coulomb's law:

$$F(r) = \frac{q_1 q_2 e^2}{4\pi\epsilon_0\epsilon r^2} \tag{1.2}$$

where q_i is the valence of ion i, e is the electronic charge, ϵ_0 is the permittivity of free space, and ϵ is the dielectric permittivity of the medium. The inverse square distance interaction force was first described by Charles-Augustin Coulomb in his free time during military postings in revolutionary France. The force arises from the interaction energy w of a charge $q_1 e$ with the electric potential ψ of a charge $q_2 e$:

$$w(r) = q_1 \cdot \psi(r) = \frac{q_1 q_2 e^2}{4\pi\epsilon_0\epsilon r} \tag{1.3}$$

The system becomes increasingly more complicated as additional ions are added, however an exact solution to this problem at infinite dilution was found by Peter Debye and Erich Hückel, and is encapsulated within Debye-Hückel theory[7]. In this theory, an ion attracts around itself ions of the opposite charge, counterions, in order to lower its energy. The counterions form an 'ionic atmosphere' that has the effect of

screening the charge of the central ion, giving rise to a screened electric potential. In the linearised theory for interactions between ions in a 1:1 monovalent electrolyte, this gives:

$$\psi(r) = \frac{qe}{4\pi\epsilon_0\epsilon r} e^{-\kappa r} \tag{1.4}$$

where κ is a constant with units of m^{-1}. Thus, inverse κ can be understood as the length scale over which the charge on the central ion is screened, and is known as the Debye length, λ_D, given by:

$$\kappa^{-1} = \lambda_D = \sqrt{\frac{\epsilon_0\epsilon k_B T}{2e^2 n_0}} \tag{1.5}$$

where k_B is the Boltzmann constant and T is the temperature. n_0 is the bulk number density of ions, so the Debye length is inversely proportional to the root of the ion concentration, and increasing ion concentration causes charge interactions to decay over smaller distances.

The linearised Debye-Hückel theory can also be used to understand the interactions between charged surfaces across films of electrolytes. When immersed in an electrolyte solution, surfaces tend to become charged, either by the dissolution or adsoption of ions to the surface, or by acidic effects of surface groups (for example,potassium ions dissolve from muscovite mica, while silica becomes charged due to deprotonation of surface hydroxyl groups). These charged surfaces attract first a layer of tightly bound counterions known as a Stern layer, then an ionic atmosphere of counterions that decays exponentially away from the surface, in a similar manner to the ionic atmosphere about a central ion in solution. This outer, decaying layer of counterions is known as the diffuse layer. As two surfaces approach each other, the diffuse layers overlap, giving rise to an increased counterion concentration in

the confined region. This leads to an osmotic pressure Π that forces the surfaces apart, as there is an entropic drive to prevent concentration rises. The osmotic pressure at the midpoint between the surfaces at a distance D apart can be derived by considering the arguments discussed above, and is found to be:

$$\Pi = \frac{2\sigma^2 e^{-D/\lambda_D}}{\epsilon\epsilon_0} \tag{1.6}$$

where σ is the surface charge, and λ_D is the Debye length, as defined in equation 1.5. This interaction is often given the name 'double layer repulsion'.

The linearised Debye-Hückel theory is exact at infinite dilution, but breaks down at relatively low salt concentrations ($\sim$ 1 mM) as ion size and correlation effects become important[8]. If the theory is treated in its non-linearised form, it can provide a reasonable description of electrolyte solutions to much higher concentrations[6,9], but experimental measurements still show substantial deviations from Debye-Hückel theory at concentrations greater than $\sim$ 1 M.

At concentrations greater than 1 M, the picture of electrolytes becomes increasingly complex, with ions occupying a large volume within the solution and substantial concentrations of contact ion pairs. Lots of research effort has gone into studying and describing the behaviour of these systems[10–12], but as yet there is no universally accepted and applicable theory that describes the behaviour of highly concentrated electrolytes in all circumstances.

1.1.3 | DLVO Theory and Surface Interactions in Electrolytes

The double layer interaction between charged surfaces and Van der Waals interactions between macroscopic objects can be unified into a

single theory of surface interactions in electrolyte solutions. This is the much celebrated DLVO theory, named for Boris Derjaguin and Lev Landau, who first published this idea in the Soviet Union in the 1940s[13], and Evert Verwey and Theodoor Overbeek, who independently found the result while working in the Netherlands seven years later[14]. The forms of interaction potential that may resolve from this combination are shown in figure 1.2.

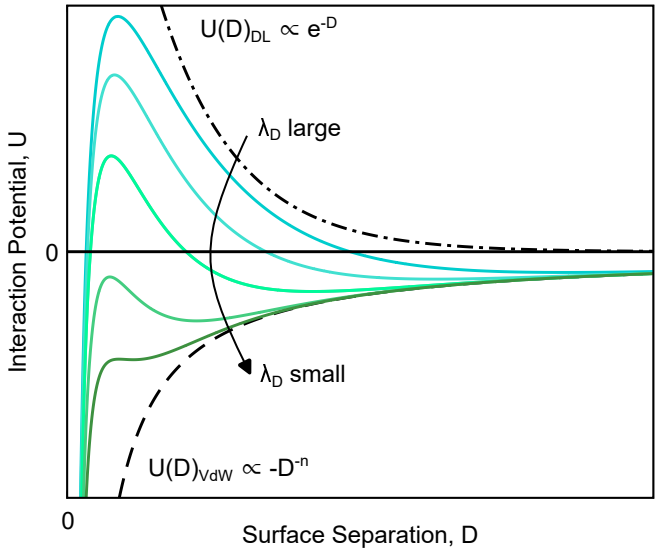


Figure 1.2: Forms of interaction potentials (solid lines) between two surfaces that may arise from combinations of the double layer (U_{DL}, dot-dashed line) and Van der Waals (U_{VdW}, dashed line) interactions. The effect of reducing Debye length λ_D, equivalent to raising ion concentration, is shown.

The Van der Waals term has an D^{-n} dependence (n depends on the geometry of the system) and the double layer term has an e^{-D} dependence. This means that the Van der Waals contribution dominates both at the very short range, where a deep adhesive minimum is predicted, and at the very long range, meaning long range interactions between surfaces are attractive. However, it is possible under certain ion concentrations and surface charges for the double layer term to dominate at intermediate ranges. This can give rise to a large energy barrier to adhesion, and can introduce a secondary, or flocculation, minimum

to the interaction potential. In the years since their prediction, these forces have been probed and measured using surface forces measurement techniques, and by studying the interactions between colloidal particles[15–18].

1.1.4 | Non-DLVO Forces and Structural Forces

Both the Van der Waals and double layer interactions are founded on continuum theories for the solvent. This naturally breaks down in thin films between surfaces where molecular size effects become important, and in high concentration systems where a solute occupies a substantial fraction of the volume of the system. In these cases, forces that are outside of the DLVO prediction can arise from ordering of molecules within the system. These forces are often known as ‘structural’ or ‘solvation’ forces.

The most common form of structural forces that arise when liquids are close to a smooth solid surface are oscillatory, and decay with increasing distance from the surface. These arise in a similar way to the solvation spheres that exist around solute or solvent molecules in the bulk liquid. This is determined by the structure and geometry of the molecules themselves, and their ability to pack around each other and against surfaces[6]. In simple spherical liquids in the bulk, this leads to a decaying series of density oscillations about a central molecule[19,20]. At surfaces, this gives rise to similarly decaying density oscillations away from the surface as the liquid molecules form layers at the liquid-solid interface[21–23]. At large distances from the central molecule or from the surface the bulk density of the liquid is recovered. These phenomena are shown in figure 1.3.

The wavelength of the oscillations from the surface will depend on

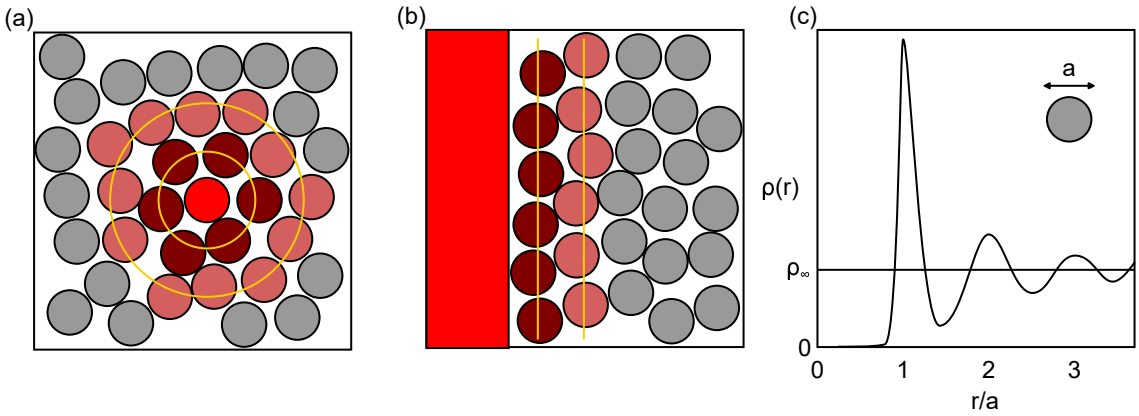


Figure 1.3: Structuring of molecules with diameter α around a central molecule or a hard surface give rise to a decaying series of density oscillations. (a): Hydration shells around a central molecule in bulk fluid. (b): Layering of solvent molecules at a smooth surface. (c): Density profile from (a) showing oscillations decaying to a bulk density value ρ_∞ with a wavelength given by the diameter of the molecule. (b) gives rise to a similar density profile but the definition of the surface position can give rise to phase shifts in $\rho(r)$. Normalising this density profile by ρ_∞ gives rise to the pair distribution function $g(r)$.

the exact nature of liquid at the interface. In the example shown in figure 1.3, oscillations arise from simple steric arguments in a hard sphere liquid, and such profiles can be measured by investigating the forces at surfaces[22], however liquids can show more complex behaviours, including regions with oscillating charge or solvent affinity[24].

1.2 | Complex and Concentrated Electrolytes

Traditional theories of electrolytes have described the behaviour of the ideal case in terms of Debye-Hückel theory[7], and examined the deviations from this behaviour[10–12]. Experimentally, much of this ideal behaviour has been verified in the dilute regime. There has also been a strong drive from electrochemists to study the behaviour of electrolytes at concentrations ~ 1 M, where ionic conductivity of liquid electrolytes generally peaks due to the competition between increasing concentration of charge carriers with decreasing ion mobility as concentration is increased. Beyond these concentrations, electrolyte structure, beha-

viour and properties can change dramatically, giving rise to unexpected forces and unique structures[25]. This is the regime of complex electrolytes.

As ion density in a solution is increased, the complexity begins to emerge. The mean separation between ions falls, until ions are likely to be in contact, or separated by single solvent molecules. Correlations between multiple ions must be considered, rather than the pair potentials which govern ion interactions at lower concentrations. In these cases, the shape and charge distribution of an ion will also play a significant role in the interactions between ions and between surfaces immersed in electrolytes, alongside classical electrostatic and Van der Waals forces. Such interactions compete over similar length and energy scales, so small perturbations to the system, such as in temperature or concentration, can lead to dramatic effects in the structure and behaviour of an electrolyte in the complex regime. The work of this thesis focuses on studying electrolytes in this complex regime.

1.2.1 | Water-in-Salt Electrolytes

Water-in-Salt (WiS) electrolytes represent a clear deviation from the well understood dilute electrolytes. In these systems, the typical salt/solvent ratio is overturned, such that the salt makes up the majority of the electrolyte solution in terms of both the mass and the volume of the solution. They were first described by Liumin Suo in 2015, and have shown promise as a safe, non-flammable alternative to organic electrolytes currently used in high energy density electrochemical energy storage[26] due to their ability to form passivating films at electrode surfaces and to rapidly conduct charge. After almost a decade of study, questions remain about the behaviours and structures within the elec-

trolyte that give rise to these unique properties.

In chapter 3, we discuss measurements of WiS electrolytes at surfaces, and in chapter 4, we present measurements of the bulk WiS electrolytes. These measurements shed light on the origins of the desirable properties of these solutions, and will be important in the further design of WiS based devices.

1.2.2 | Ionic Liquids and Ionic Liquid Mixtures

Ionic liquids are liquids composed purely of ions, and are perhaps the clearest departure from the classical theories of electrolytes. They are often called 'designer solvents' as the anion and cation can be chosen to give specific properties, and can be further designed by mixing ionic liquids with different properties[27]. One aspect of ionic liquids that clearly varies depending on the nature of the ions is the structure adopted by the liquid in the bulk. Ionic liquids can separate on the nano-scale into domains of high charge density and low charge density, which can be a desirable quality for electrochemical energy storage[28].

In chapter 5, we investigate how ionic liquids can show different structural behaviours at surfaces, and study the effects of mixing two such ionic liquids together on the structures and properties of the liquid mixture at solid interfaces. These measurements study to what extent surface structure is a tunable property within mixed ionic liquids, with consequences for the applications of such liquids.

1.2.3 | Molecular Ion Denaturants and Guanidinium Chloride

The behaviour of proteins in electrolytes is known to be very dependent on the nature of the ions present, and ions can be ordered into a series by the extent to which they precipitate proteins[29]. However, the pre-

cise reasons for the ordering of ions within this series remains poorly understood, particularly in the area of molecular ion denaturants such as the guanidinium ion[30]. Guanidinium chloride solution at concentrations of 3 M, far in excess of the well understood dilute electrolyte regime, is routinely used within biochemistry to unfold and denature proteins, yet precisely how it acts at protein surfaces and leads to unfolding remains an open question.

In chapter 6, we present measurements of the forces present in guanidinium chloride solutions confined between negatively charged surfaces that serve as a simple model for negatively charged protein exteriors. These measurements have implications for the mechanism by which this molecular ion works to denature proteins.

1.3 | Surface Forces Measurement Techniques

DLVO and non-DLVO forces present in a liquid can be measured by confining the liquid between two surfaces and measuring the force acting between the surfaces. As the distance between the surfaces is varied, a picture of the total force profile $F(D)$ can be determined. Multiple techniques have been developed to study these forces, and two common examples, the atomic force microscope and the surface force balance, are briefly discussed here.

1.3.1 | The Atomic Force Microscope

One common method of surface force measurement is the Atomic Force Microscope (AFM). The technique was invented in 1986 by Binnig, Quate and Gerber[31]. In brief, an atomically sharp tip on the end of a cantilever spring is scanned across or approached towards the surface of interest using a piezoelectric actuator. Any changes in the interaction forces

between the surface and the sharp tip cause the cantilever to deflect, which can be measured using a laser and photodetector. This allows for images of surfaces with atomic resolution to be built up by scanning laterally at the surface, or for profiles of the forces as the separation between the surface and the tip changes to be built up by scanning vertically towards and away from the surface. The core features of an AFM are shown in figure 1.4.

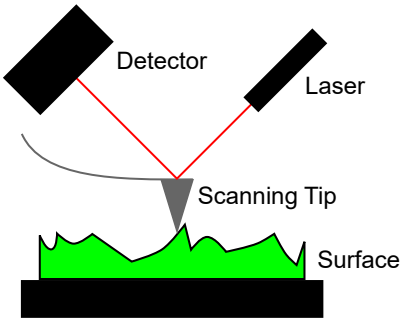


Figure 1.4: Simple schematic of an AFM measurement.

The AFM is a very versatile tool: it can provide a three-dimensional surface profile, can work in vacuum, air or liquid environments and on conductors or insulators, and is relatively insensitive to contamination as the cantilever tip can simply be moved to an uncontaminated region of the surface.

1.3.2 | The Surface Force Balance

Another very sensitive method of measuring forces close to surfaces is the Surface Force Balance (SFB), or Surface Force Apparatus (SFA). In this technique, smooth transparent surfaces are moved together and apart, and the forces between them are directly measured by the deflection of a spring. Silver mirrors behind the surfaces form an interferometric cavity, allowing the separation between the surfaces to be measured accurately and precisely using multiple beam interferometry. In this manner, normal and lateral forces between surfaces in air or

across liquid films can be measured to a high degree of sensitivity. The core features of the SFB are shown in figure 1.5.

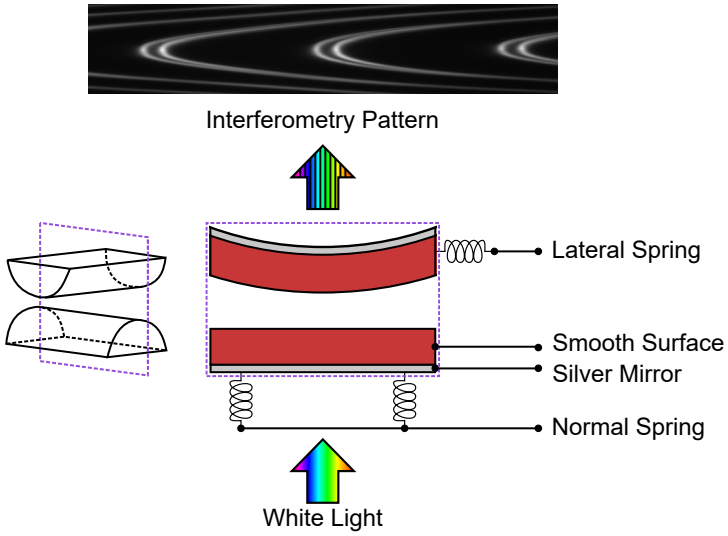


Figure 1.5: Simple schematic of an SFB experiment.

The SFB has several key advantages over the AFM: the SFB gives accurate knowledge of surface separation, which allows for meaningful comparisons between measurements and systems; further, the forces measured by the SFB can be simply related to the free energy of interaction between parallel surfaces, allowing for a greater thermodynamic understanding of the processes and behaviours observed. All of the surface force measurements contained within this work were performed using the SFB, and an in depth description of the technique is provided in chapter 2.

1.4 | Bulk Structure Measurement Techniques

The nature of the force profile measured at liquid-solid interfaces is intrinsically related to the behaviour of the liquid in the bulk[23], and as such techniques like the SFB are powerful tools in the quest to understand liquid behaviour. However, they become even more useful when applied in combination with bulk measurement techniques. These bulk

techniques study the properties of a liquid at large distances from any interface, and produce a picture of the liquid structure that is independent of interface effects. Some of these techniques are discussed here.

1.4.1 | Scattering Experiments

Particles and waves can be scattered or diffracted by the atoms, molecules and structures present in a liquid. By shining a beam of these particles or waves through a liquid, and measuring the resulting scattering pattern, information about the nature of the liquid structure can be obtained. Perhaps the most famous example of early scattering experiments is the gold foil experiment, in which Hans Geiger and Ernest Marsden, under the supervision of Ernest Rutherford, measured the scattering of alpha particles by gold foil[32]. Most alpha particles were unscattered by the foil, but some where deflected by a small amount, and very few were significantly deflected or even rebounded. This led to the idea of the atomic nucleus, a small region of an atom in which the majority of the mass is concentrated.

Scattering experiments have seen significant development in the past century, and measurements of the scattering patterns of x-rays and neutrons are now common in investigations of the bulk structure of liquids. In this work, we utilise elastic coherent neutron scattering to measure bulk structures, and this technique is described in detail in chapter 2.

1.4.2 | Computer Simulations

Simulations are an incredibly versatile tool for studying liquids, and allow direct examination of aspects of liquids that are difficult or impossible to study experimentally. The first computer simulations of li-

quids were carried out at the Los Alamos National Laboratories in the USA in the early 1950s for a hard sphere liquid[33]. Since then, the fall in price and rise in prevalence of computers has allowed ever more complex and precise simulations[34]. In simulations, the liquid is defined by a configuration of molecules, and interaction potentials within and between molecules are specified. From this simulated box of molecules, predictions about real systems can be made, and models for molecular properties can be tested. Stable configurations and behaviours are found by various methods, which broadly fall into two categories: Monte Carlo, MC, where random numbers are used to move single particles within a liquid configuration, then the probability of finding the new configuration is assessed by looking at the Boltzmann distribution[33,35]; and Molecular Dynamics, MD, where the particles within a liquid are treated with classical equations of motion in order to determine their positions at the next time step[36].

Simulations remain small scale due to the demands of computing power, and currently the largest and most powerful simulations can model up to $\sim 10^{12}$ atoms[37] and can follow dynamics over the millisecond range[38]. Experiments are able to probe real interactions in molar quantities of atoms over many thousands of seconds, so simulations are often coupled with experimental observations to give a complete picture. In this work, we use simulations only to compare with experimental results. We use the simulation tool Dissolve[39], in conjunction with data from scattering experiments, to interpret the bulk structure of liquids.

1.5 | Overview

In this thesis, we study surface forces and structures in three cases of complex electrolytes at high concentrations: we investigate water-in-salt electrolytes at surfaces and in thin films as well as in the bulk liquid phase; we investigate how mixtures of ionic liquids differ from the pure liquids and the effect the mixture has on solid-electrolyte interfacial structure; and we study the behaviour of guanidinium chloride against surfaces and discuss the implications for the mechanisms of protein denaturing in aqueous guanidinium chloride. We study these effects using the surface force balance, neutron scattering, and additional techniques which are discussed in detail in chapter 2, then move on to present results in chapters 3, 4, 5 and 6. Finally, we present our conclusions and discuss directions of future work opened up by this thesis in chapter 7. These investigations provide clues as to the nature of concentrated electrolytes across a wide range of behaviours, from structure at equilibrium, to action at surfaces, and will be influential in the future study of these fascinating and complex liquids.

2 | Experimental Methods

The measurements carried out in this work focus on the behaviour of liquids either at surfaces or in a bulk environment. The techniques used to probe these aspects of liquid behaviour, as well as several supporting techniques, are described in detail in this chapter.

2.1 | Surface Force Measurements

The investigations of liquid structure at surfaces carried out in this work were performed using the Surface Force Balance (SFB), which is described here.

The SFB has its origins in the work of Anita Bailey and J. S. Courtney-Pratt[40], who first used interferometry to determine the separation between smooth mica surfaces whilst simultaneously measuring the forces acting between the surfaces. Development of their ideas by Tabor and Winterton allowed for the direct measurements of Van der Waals forces in air between mica surfaces[41], and further work by Israelachvili and colleagues extended the use of the SFB and introduced the idea of performing measurements across thin films of liquids[15,16]. Since these initial efforts, many extensions to the SFB have followed, allowing for measurements of different forces across a wide range of systems and length scales[42,43]. To date, the SFB has been used to study forces across films of polar[44,45] and apolar liquids[22,46,47], liquid crystals[48–51], dilute[16,52–57] and concentrated[58–61] aqueous electrolytes and water-in-salt electrolytes[62,63], deep eutectic solvents[64,65], ionic liquids[24,66–73], and even household foodstuffs such as chocolate[74] and mayonnaise[75]. In this work, we use the version of the surface force balance described by Jacob Klein[76].

In brief, the SFB consists of a pair of back-silvered mica surfaces, glued onto a cylindrical silica lens using an epoxy resin. The lenses are mounted in a crossed cylinder configuration within the instrument. The surfaces may be moved closer together or further apart using either a mechanical or piezoelectric drive, and their separation can be measured through an interferometric technique with sub nanometer precision. The normal forces acting across the fluid film can be measured through the deflection of a Hookean spring. The surfaces may also be moved laterally with respect to one another, allowing lateral, friction forces between the surfaces to be measured by the deflection of a second spring. These key features are shown in figure 2.1.

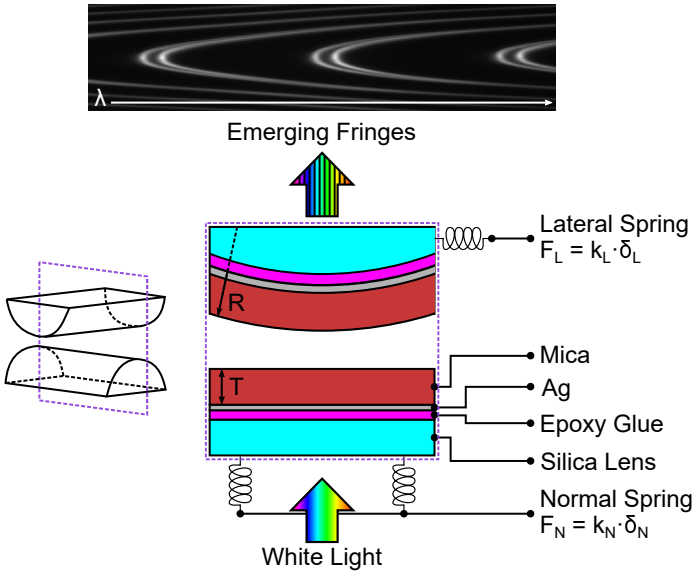


Figure 2.1: Summary of the SFB. Mica surfaces are back-silvered and glued onto cylindrical lenses with radii ∼ 1 cm. The lenses are mounted in a crossed cylinder configuration to give a single point of closest approach. They can be moved together and apart using a mechanical or piezoelectric drive. The lower lens is mounted on a normal spring and the upper lens is mounted on a lateral spring with spring constants k_N and k_L respectively. The radius of curvature of the surfaces, the mica thickness, the surface separation, and the deflection of the normal spring and therefore force can all be measured from the wavelength λ of the emerging fringes of equal chromatic order. Lateral spring deflections and forces can be measured using an air-gap capacitor.

2.1.1 | Surface Properties and Preparation

In order to study forces in a confined liquid using the surface force balance with molecular resolution and precision, the surface material must possess certain qualities. It must be transparent to visible light, and able to be prepared in atomically smooth sheets with centimetric areas and micrometric thicknesses. Muscovite mica, a naturally occurring mineral, ideally meets these requirements[77]: it can be easily cleaved to reveal regions with centimetric areas completely free of steps on both exposed faces, with thicknesses as little as 1 µm.

Mica is by no means the only surface substrate available for use in the SFB, and many researchers have modified the SFB to allow for other surface materials and properties. Mica can be treated with adsorbates to produce different surface behaviours[78,79], while SFB experiments have been performed using surfaces made from sapphire[80], silica[81,82], gold[83–85], graphene[86,87], liquid mercury[88], and even human hair[89].

Mica surfaces are vulnerable to contamination, and an important aspect of working with the SFB is an understanding of and minimisation of potential contaminants. Freshly cleaved mica is a high energy surface, and it will adsorb contaminants from the air or from tools and glassware used in the preparation process, to lower its surface energy. Further, the cleaving process can leave a charge on the mica surface, so the mica can attract particulate contamination carrying the opposite charge[90]. In order to minimise contamination, special care must be taken while cleaving the mica and setting up the experiment.

Preparation work takes place in a laminar flow hood (LFH), which draws air through a high-efficiency particulate air (HEPA) filter and directs the air in a laminar fashion towards the user. The HEPA filter re-

moves particles with radii greater than 5 µm, while the laminar flow ensures introduced particles do not contaminate regions upwind within the hood, producing a clean and particle free environment in which to work. All glassware that could introduce contamination to the experiment is cleaned with a hydrogen peroxide and sulfuric acid 1:3 mixture (piranha solution, a strong oxidiser) to remove all organic residues, while stainless steel parts and tools are cleaned in nitric acid. The equipment is then rinsed in ultrapure water (18.2 MΩ cm, < 3 ppb total organic carbon) and stored dry, or in absolute ethanol.

Mica (S&J Trading Inc., V-1 grade) is cleaved by hand to produce large, step free regions with thicknesses 2 - 6 µm. The thickness can be estimated during the cleaving process from the intensity and colour of interference patterns, arising from visible light passing through the mica, and is accurately measured during an experiment. Once produced, the sheets are cut away using a hot platinum wire, producing a 'burnt edge' on each mica piece. The pieces are then quickly adhered to a freshly cleaved base sheet of mica. This has the effect of protecting one face of the single faceted mica pieces. A semi-transparent silver layer of thickness $\sim$ 45 nm is then evaporated onto the base sheet in a high vacuum ($\sim 10^{-6}$ mbar) with a deposition rate of $\sim$ 0.1 nm s^{-1}. These parameters are monitored using a quartz crystal microbalance, and ensure a smooth silver layer is produced, with a balance between reflection and transmission of light at the mica-silver interface. The mica pieces now have one silvered face and one protected face, and are ready for use in an SFB experiment. An example of a silvered base sheet is shown in figure 2.2. The base sheet is stored under vacuum in a desiccator until required. This method has been shown to produce clean mica surfaces for use in SFB experiments[91].

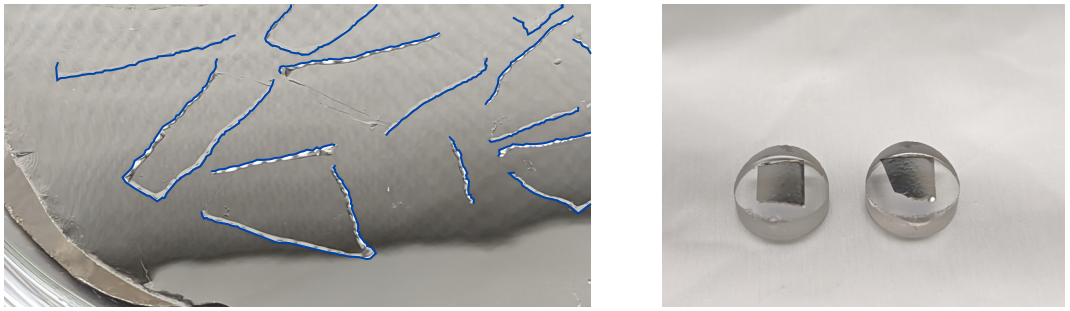


Figure 2.2: Mica preparation. *Left:* single faceted mica pieces are cut with a hot platinum wire, adhered to a freshly cleaved base sheet, and coated with silver. The burnt edges are highlighted in blue. *Right:* during an experiment, the silvered mica is cut to size, lifted from the base sheet, and glued silver side down onto a cylindrical glass lens.

During an experiment, the back-silvered mica pieces are cut to size ($\sim$ 1 cm^2) and levered up from the base sheet by inserting a clean needle between the base sheet and the burnt edge of the mica. The mica can then be lifted from the base sheet using clean tweezers, and glued, silver side down, to a cylindrical glass lens using an epoxy glue (EPON 1004, Shell Chemicals) such that the freshly exposed mica face is upwards. Two lenses must be prepared in this manner from a single piece of mica, such that the mica thickness is identical on each lens. Two such lenses are shown in figure 2.2.

It is known that the high energy mica surfaces can quickly adsorb films of airborne molecules after exposure to ambient air[92,93]. These films can form within two minutes of cleaving the mica, typically have a thickness of $\approx$ 0.5 nm, and are formed from adsorbed water and carbon dioxide from the atmosphere. They are known to be removed upon immersion of the surface in water[52,91,94], however it is not known to what extent these films will be removed on immersion in the complex electrolytes investigated in this study. It seems likely that much of the film will dissolve, as the liquids studied are either aqueous or good solvents in their own right, though owing to the high viscosity of some of the liquids investigated, this may be a slower process than in pure water.

The potential presence of an undissolved film adds a small uncertainty to the absolute zero position of surface contact in the following surface force measurements.

2.1.2 | Derjaguin Approximation

The surface force balance measures the forces acting between two macroscopic, interacting crossed cylinders separated by a distance D, $F_{\text{cylinders}}(D)$. From a theoretical perspective, it is often easier to think in terms of free energy of interaction between parallel plates per unit area, $G_{\text{flat}}(D)$. Experimentally, such a set up of atomically parallel plates is not practical, but the two quantities are related by the Derjaguin Approximation[6]:

$$F_{\text{cylinders}}(D) = 2\pi R G_{\text{flat}}(D) \tag{2.1}$$

where R is the radius of curvature of the cylinders. This approximation is valid for all types of force law, so long as the radius of curvature of the surfaces R is much greater than their separation D.

By convention, surface force measurements are reported with forces normalised by the radius of curvature of the surfaces, F/R. This quantity is independent of the precise experimental surface geometry, so comparisons may be made between measurement spots and between different measurements. However, it is important to recall that $F_{\text{cylinders}}/R \propto G_{\text{flat}}$, and that when discussing the mechanisms and behaviours that give rise to the observed forces, it is $F/2\pi R$ that is the important thermodynamic quantity.

2.1.3 | Lens Mounts and Motion

The two lenses are mounted in removable sections of the SFB, which allows easy access for lens set up, and SFB maintenance and cleaning.

The lower lens is mounted in the boat and the upper lens is mounted in the top part. These are shown *in situ* in figure 2.3 and in more detail in figure 2.4.

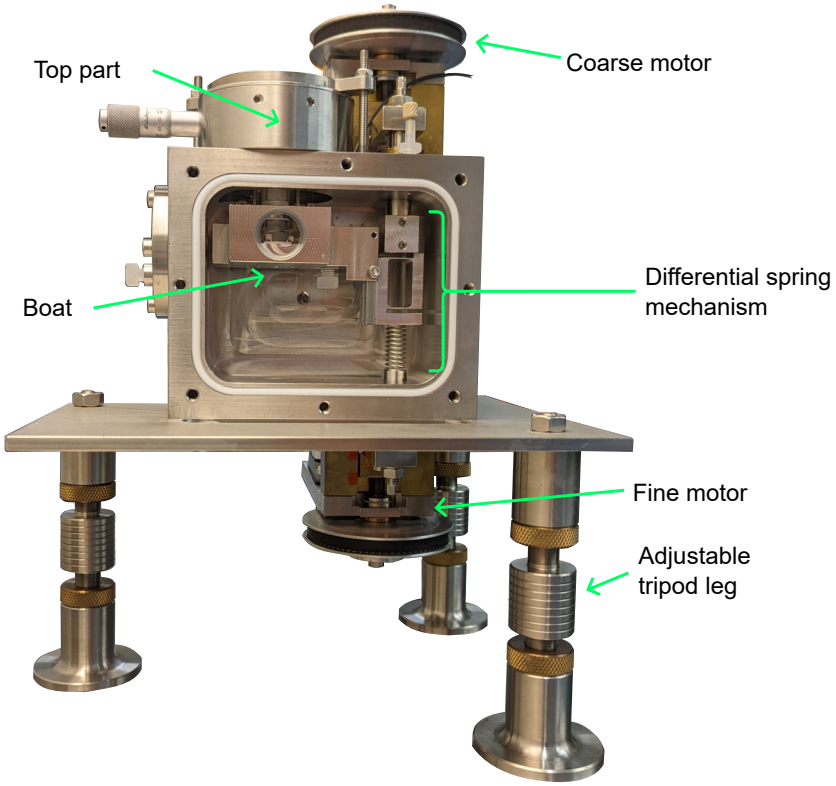


Figure 2.3: The interior of the SFB set up for a measurement, with the top part and boat in place. The motor wheels and differential spring mechanism are shown. The SFB chamber sits on three legs that can be adjusted to ensure measurements take place on a level surface.

The boat holds the lower lens. The lens sits above a quartz window that allows for transmission of light to the lens. It is mounted on a pair of normal leaf springs that separate the lens from the boat. The springs are Hookean, and the spring constant k_N is calculated prior to measurement by measuring the deflection of the springs after applying a series of weights of known mass.

The upper lens is held in the top part. The lens is mounted above a sectored piezoelectric tube, which allows for translation of the lens either vertically or horizontally. This is suspended above the top part by a pair of vertical leaf springs. The deflection of these springs is

measured using an air gap capacitor, which allows for the measurement of noise and lateral motion within the system. Finally, a second quartz window in the bottom of the top part allows for the transmission of light to the spectrometer. Note that upon mounting within the SFB chamber, the top part is inverted relative to figure 2.4.

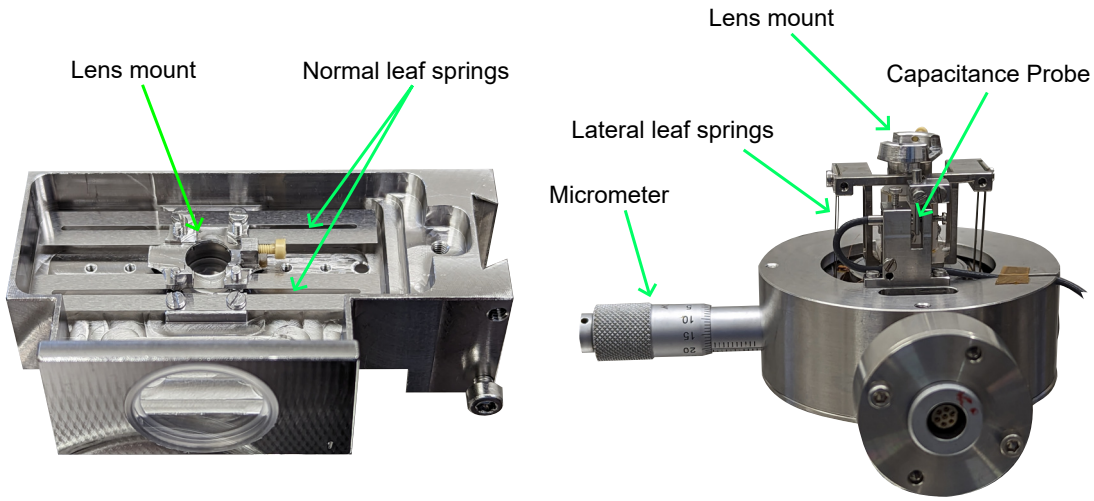


Figure 2.4: Lens positions on the parts of the SFB. *Left:* the boat, which holds the lower lens. The lens is suspended above the base of the boat by two normal leaf springs of known spring constants. It sits over a quartz window, which allows for the transmission of light. *Right:* the top part of the SFB, which holds the upper lens and piezoelectric drive. The lens mount sits directly above the piezoelectric tube. Lateral motion of the lens, either as a result of induced lateral motion or from mechanical noise, is measured by a capacitance probe. Shear forces can be measured using the probe by deducing the deflection of the shear leaf springs.

Once the lenses are prepared and mounted in the top part and boat within the SFB, the chamber is sealed and placed in the measurement room. It is placed on an isolation table, which sits on a stack of rubber, marble, rubber and concrete, on the ground floor of the laboratory. This minimises the effect of external vibrations. The SFB is set level by adjusting the tripod legs.

Motion between the lenses is controlled in three ways, referred to as the *coarse motor, fine motor,* and *piezo*. They are shown in figure 2.5, with the red arrow referring to the direction they move to approach the

lenses.

The boat is directly connected to an electric stepper motor drive. Termed the *coarse motor*, this drive is used to position the lens prior to making measurements. It allows for motion over several centimetres, with a precision of about one micron. The direct connection between the motor and the boat means that the motor generates large amounts of mechanical noise in the system, so is always disabled before making measurements.

A second, identical, stepper motor is separated from the boat by a differential spring mechanism, made up of a coiled spring and a stiff spring. The spring constant of the stiff spring is approximately three orders of magnitude greater than that of the coiled spring. The differential spring set up damps the mechanical noise from the motor, reduces the range of the motor, and allows for greater precision. This is the *fine motor*, and allows for motion over about a millimetre, with a precision of about a nanometre.

Finally, the upper lens in the top part sits above a piezoelectric crystal in the shape of a tube. The outside and inside faces of the tube are coated in silver, and the outer silver coat is divided into four separate regions, giving five sectors total to the tube. This sectored piezoelectric tube is known as the *piezo*. By applying equal voltage to the four outer sectors, or the inner sector only, or to all five sectors, the piezo can expand and contract in a very controlled manner, with a total range of several microns and sub-nanometre precision. Lateral motion can also be introduced using the piezo by applying equal but opposite voltages to two opposite sectors.

Either the fine motor or the piezo may be used to collect data. The fine motor has much greater range of motion, so can apply much lar-

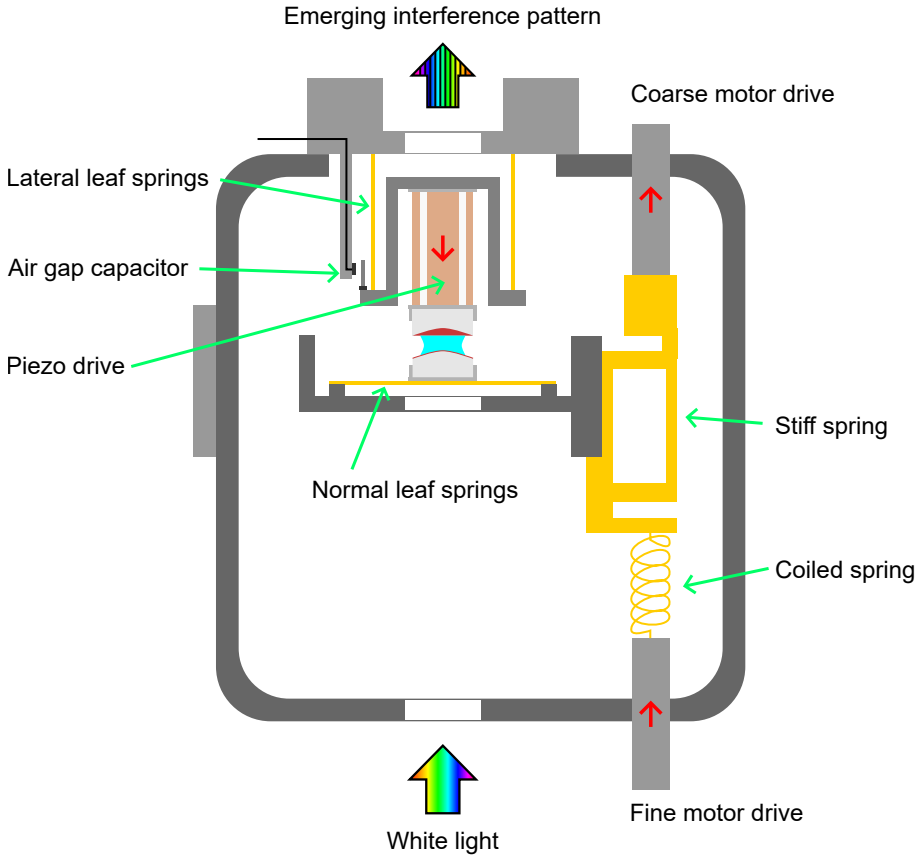


Figure 2.5: Cartoon of the features of the surface force balance with the boat and top part in place. The upper lens is mounted on a sectored piezoelectric tube which allows for fine normal and lateral motion. This is separated from the main body of the top part by shear leaf springs, the deflection of which can be measured using an air gap capacitor. The lower lens is mounted on a set of normal leaf springs within the boat. The boat is connected to two motors, the upper of which drives the position of the boat directly and allows for coarse positioning of the lens, while the lower motor is separated from the boat by a differential spring mechanism which allows for much finer motion of the lens. All springs are shown in yellow. The direction the drives move to cause the lenses to approach is shown by the red arrows.

ger forces, however there is still some non-negligible mechanical noise associated with it, so for accurate work at small forces, the piezo is used.

2.1.4 | Optical Pathway and Image Analysis

During a measurement, the separation between the lenses is measured using multiple beam interferometry. An Ar-Xe arc lamp produces collimated white light that is directed through the window in the bottom of

the SFB chamber. The light passes through the lenses, where the semi-transparent silver-backed mica surfaces form a three layer symmetrical interferometric cavity. Multiple reflections take place between the silver mirrors leading to interferences, and the emerging interference pattern is focused onto the slit of a grating spectrometer. The resulting pattern of light takes the form of a series of Fringes of Equal Chromatic Order (FECO), which can be observed by eye through the spectrometer eye piece, or recorded using a CCD camera. The shape of the fringes arises due to the geometry of the cavity, as shown in figure 2.6, while the bi-refringent nature of cyrstalline mica leads to the splitting of the fringes into doublets. Fringes can be labelled with an order, referring to the number of nodes in the standing wave between the silver mirrors.

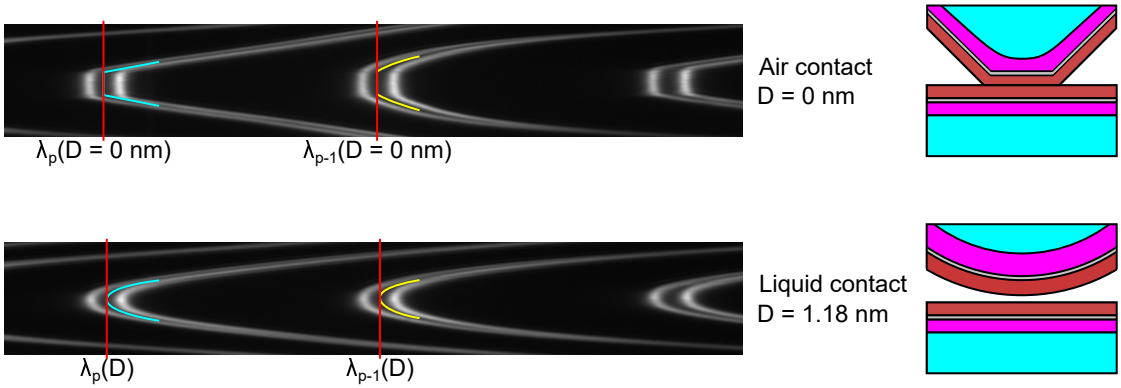


Figure 2.6: Example fringes of equal chromatic order recorded in this work for calibration purposes. The red lines shows the fringe positions. The geometry that gives rise to the fringe shape is shown. *Top:* The fringes during air calibration, in which mica surfaces are brought together in air. Distances for the rest of the experiment are calculated relative to the fringe positions in this image. Strong adhesive forces between high-energy mica surfaces lead to flattening of the fringes as shown, enabled by deformations in the glue layers. In air, there is a clear difference between fringes with odd order and fringes with even order: those with greater curvature are even. *Bottom:* The fringes in liquid contact. A thin film of liquid remains trapped between the surfaces even under high loads, resulting in the non-zero separation.

A formal mathematical treatment of the FECO was first undertaken by Tolansky[95], and later formulated for use in the surface force balance by Israelachvili[77]. A fringe of odd order is chosen (leftmost fringe in

figure 2.6) and labelled as the p *fringe*, with further fringes labelled relative to this fringe (for example, the centre fringe in figure 2.6 is labelled as the $p-1$ *fringe* while the rightmost as the $p-2$ *fringe*). The surfaces are brought gently into contact in air, where strong adhesion between the mica surfaces leads to deformations in the glue layer to allow a large region of surface contact, which is resolved as fringe flattening (top image, figure 2.6). From this image, and by comparison to the Hg green (546.1 nm) and yellow (579.1 nm) lines, the precise mica thickness and the wavelengths of the p and $p-1$ fringes at mica contact ($D = 0$) can be found. Once the wavelengths of the p and $p-1$ fringes at contact, $\lambda_p(D=0)$ and $\lambda_{p-1}(D=0)$ are known, the surface separation D across a film of any medium can be calculated by tracking the wavelength of the p fringe, $\lambda_p(D)$:

$$\tan(k\mu_{\text{medium}}D) = \frac{2\bar{\mu}\sin\theta}{(1+\bar{\mu}^2)\cos\theta \pm (\bar{\mu}^2-1)} \tag{2.2}$$

where k is the wavenumber of the light, $k = 2\pi/\lambda$, $\pm$ refers to even and odd fringes,

$$\bar{\mu} = \frac{\mu_{\text{mica}}}{\mu_{\text{medium}}}, \quad \theta = \frac{p\pi(\lambda_p(D)-\lambda_p(D=0))}{\lambda_p(D=0)}, \quad p = \frac{\lambda_{p-1}(D=0)}{\lambda_{p-1}(D=0)-\lambda_p(D=0)}$$

and μ_x is the refractive index of component x.

In our measurements, the CCD camera was set to record an image of 140 vertical by 2688 horizontal pixels at a rate of approximately 5 Hz. This produces a two-dimensional matrix of intensities at each pixel. Image processing of these matrices takes place using centre of mass tracking in MATLAB®, and the process is shown in figure 2.7. By defining the region of the fringe and finding the centre of mass of each line of pixels, the centre of mass profile of the entire fringe may be calculated.

This can be fitted to a parabola, with the peak of the parabola giving the pixel position of the fringe. By comparison to the air calibration image (figure 2.6 *top*) and with knowledge of the magnification of the optical system and refractive index of the medium, the wavelength of the fringe at any point during the measurement can be calculated. Applying equation 2.2 allows absolute distances between the surfaces to be calculated with an accuracy of ~ 0.5 nm and a precision of ~ 0.1 nm.

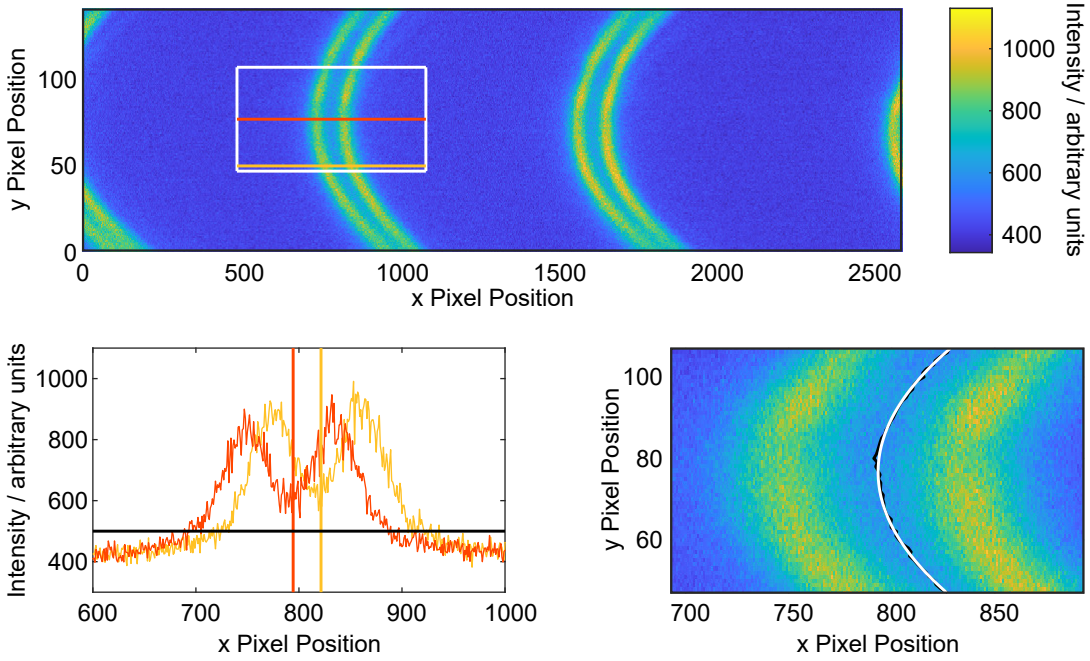


Figure 2.7: Summary of image processing. *Top:* The fringes captured during a measurement are plotted by intensity. The white box shows the defined *p* fringe tracking window. *Bottom left:* The intensity profiles of two horizontal lines of pixels are shown (selected from the top image). The red line is taken from the centre of the fringe while the yellow line is taken from the edge of the fringe. The noise threshold is shown in black, and the centres of mass of each pixel line is calculated and shown as a vertical line. *Bottom right:* The calculated centre of mass of the total fringe is shown in black, and fitted to a parabola shown in white. The pixel position of the fringe is taken as the peak of the parabola.

2.1.5 | Force Profiles

During a measurement, a fluid of interest is introduced between the lenses once the air calibration images have been taken and analysed. A

series of experimental runs is then performed, in which the surfaces are moved together and apart many times. Each run probes some part of a *force profile*, a relationship between the forces acting between the two surfaces and the separation of the surfaces, $F(D)$, that is characteristic of the confined fluid. In certain cases, $F(D)$ may be measured in a single run, but in other cases (particularly if $F(D)$ is oscillatory), many runs must be made in order to measure the total force profile function.

In the majority of runs, the measurement begins with the surfaces at a large initial distance D_0, such that it can be assumed that no forces are acting between the surfaces, typically > 100 nm. Surfaces are then approached at a constant velocity, starting at a time t_0, such that the separation between the surfaces decreases at a linear rate, $D(t) = D_0 - vt$ as long as no forces are acting between the surfaces. These approaches are made using either the fine motor or the piezo moving at velocity v, with the coarse motor disabled to reduce the impact of mechanical vibrations.

Once the surfaces reach a separation over which a force can act, the leaf spring normal to the direction of motion, upon which the lower lens is mounted, deflects by a distance $\delta(t)$, where $\delta(t)$ is the difference between the measured surface separation $D(t)$, and that expected from the linear approach, $D_0 - vt$.

The normal force acting between the surfaces is equal to the restoring force of the spring, and is given by:

$$F_N = k_N \delta(t) = k_N[(D_0 - vt) - D(t)] \tag{2.3}$$

where k_N is calculated prior to the experiment by measuring the deflection of the spring under a series of 'dummy lenses' of known mass.

Retractions may be analysed in a similar process, with the fine motor

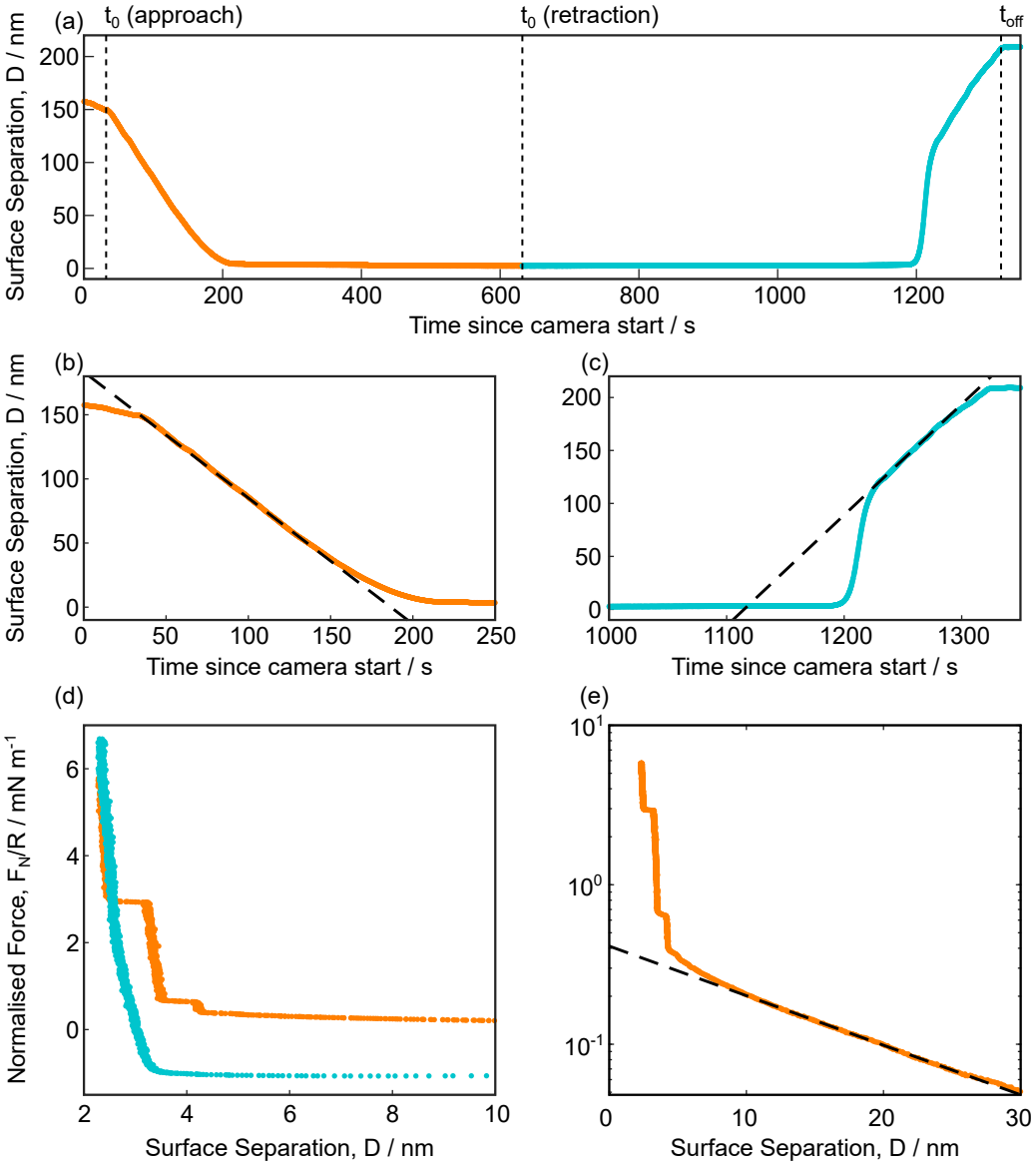


Figure 2.8: Summary of force profile analysis. (a): The surface separation calculated from equation 2.2 as a function of time. Surfaces approach one another from time t_0 (approach) to time t_0 (retraction), at which point the motion of the surfaces is reversed. The retraction is stopped at t_{off}. (b): The linear baseline of the approach. This is fitted from 80 to 50 nm of surface separation, in which the approach is linear so it can be assumed no forces act. The velocity of the approach is 0.98 nm s^{-1}. (c): The linear baseline of the retraction. The velocity of the retraction is 1.05 nm s^{-1}. (d): The completed force profile calculated using equation 2.3, normalised by the radius of curvature of the lenses (see equation 2.1). The forces measured on approach show a series of hard walls, separated by 'jumps in' that characterise a spring instability. The forces measured on retraction reveal the presence of an adhesive well. (e): The approach forces plotted on a logarithmic force scale. This reveals the presence of an exponentially decaying monotonic repulsive force. The characteristic decay length of this force can be calculated from the gradient of the decay.

or piezo acting with an opposite velocity, pulling the surfaces apart from contact. This can be used to probe adhesive forces. An example analysis of this form of experimental run is shown for an ionic liquid in figure 2.8.

This method of constantly moving the surfaces during measurements leads to the occurrence of hydrodynamic forces acting between the surfaces. These forces can be estimated by considering the hydrodynamic force F_H acting between a sphere of radius R and a plane, separated by a fluid film of thickness D and viscosity η, and moving together at a velocity v[96]. In this case,

$$F_H = \frac{6\pi\eta R^2}{D} v \tag{2.4}$$

Using typical values for our systems ($R \approx 10^{-2}$ m, $D \approx 10$ nm, $\eta \approx 10$ mPa s, $v \approx 0.1$ nm s^{-1}), we find that $F_H/R \approx 10^{-2}$ mN m^{-1}. This is small compared to the forces seen close to contact in our studies, so is considered negligible for this work.

The partial force profile shown in figure 2.8 highlights an important feature of this measurement technique: that of the spring instability[52]. As the surfaces move together, the forces acting between them can be balanced as long as the gradient of the force with distance $\partial F_N(D)/\partial D(t) < k_N$. If this condition is not met, the surfaces will be pulled together or apart by the spring until it is. Thus, regions of the force profile for which $\partial F_N(D)/\partial D(t) > k_N$ are inaccessible to measurement. These jumps occur at instability points, that may be taken as the maxima or minima of features within the force profile.

A second way of probing adhesive forces takes advantage of the spring instability by performing a stepwise contraction of the piezo and allowing the system to reach equilibrium between steps. This non-linear

application of force eventually causes the surfaces to attempt to equilibrate very close to an instability point. This causes the surfaces to jump apart by exactly the distance the spring is extended. By comparing the surface separation before and after the jump, the adhesive force of the minimum position can be directly calculated from Hooke's law.

In total, a force profile yields large amounts of data about the confined film of interest, and analysis of minima and maxima positions, oscillatory wavelengths, and exponential decays extracted from the force profile can yield fundamental information about the nature of the liquid.

2.1.6 | Experimental Error Analysis

Great care is taken to ensure that errors within our measurements are minimised. We have noted above the use of an isolation table to minimise the effects of external vibrations on the SFB. All measurements take place at 21^{o}C within a temperature controlled room, and the SFB is sealed during measurements to prevent the introduction of containments to the liquid of interest. The SFB itself is further separated from the environment by enclosing the instrument within a box that minimises the transmission of motion from air currents within the room to the SFB. Here we discuss the origins and magnitudes of errors that these measures are unable to eliminate.

There is a random error associated with the measured surface separations at each recorded point. This arises as a result of uncertainty in the fringe tracking procedure (shown in figure 2.7), and quantifies the precision in our distance measurements. The uncertainty is related to mica thickness, with thicker mica leading to greater uncertainty as more fringes occur within the wavelength window of the camera,

and thus there is a smaller resolution in the tracking of the p fringe wavelength. This error is important when considering single runs, and is typically low, $\sim 0.1 - 0.2$ nm.

When comparing between single runs, further variation in the distances measured at like points within the overall force profile are apparent. This variation is shown in figure 2.9. These errors arise due to thermal expansions within the system that are minimised by the temperature control measures but are still present. Such effects can lead to expansion of the mica layer and small shifts in the optical pathway, such that there is a small uncertainty in the zero position between measurement runs on the same spot. This is typically on the order of $0.2 - 0.4$ nm, including the uncertainty of individual runs. In a similar way, measurements on different measurement spots or different mica surfaces also show variations in the distance measurements which arise due to changes in the optical path. In these cases, variation between like points in runs on different contact spots or different mica surfaces can typically be ~ 0.5 nm. This quantifies the accuracy of our absolute distance measurements.

In addition, there is error associated with the measured forces. Systematic error in the presented normalised forces arises due to uncertainty in the spring constant k_N and in the measured experimental radius R. In each case this is ~ 5 % and is constant throughout a single measurement, affecting the overall accuracy of our absolute force measurements.

The random error associated with the distance measurements within each run leads to a random error in the force, as force is calculated from the apparent spring deflection. This error is the precision in our force measurements. It is typically very small, $\sim 10^{-3}$ mN m^{-1}, and is similar

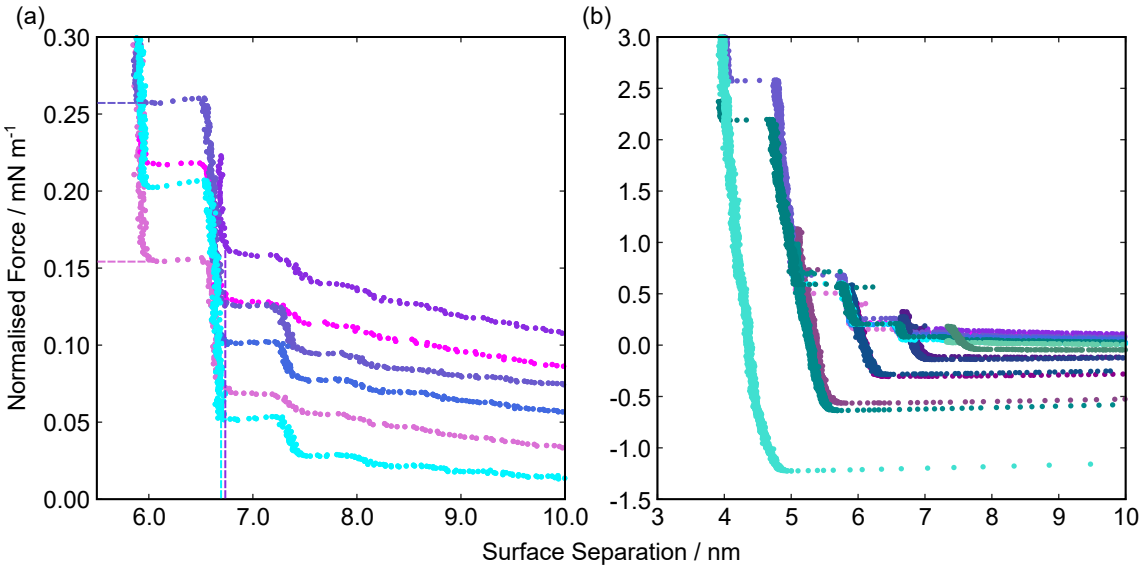


Figure 2.9: Errors during a typical surface force balance measurement on an ionic liquid. (a) and (b) show the same data on different force scales. (a): Slight shifts in the optical path can lead to small variations in the measured distances of about 0.2 nm, shown by the dashed vertical lines. Errors in the baseline, and thermal drifts occurring after the baseline is set can lead to vertical offsets in the force on the order of 0.1 mN m^{-1}, shown by the dashed horizontal lines. (b): Data from multiple slow approach and retraction experimental runs on an ionic liquid. Variations in distance and forces between runs can lead to the 'smearing out' of subtle effects that are qualitatively consistent across each individual run.

to the minimum force resolution of the instrument, which arises due to random noise from thermal and vibrational effects.

There is also variation between measurements in a single experiment, as shown in figure 2.9. One source of this error is in the fitted baselines. Approach baselines are consistently fitted in the region where it is assumed any forces acting between the surfaces are negligible. In the case of the measurements shown in figure 2.9, all approach baselines are fitted between 80 nm and 50 nm. R-square values for these fits are generally 0.998 or greater. Retraction baselines are set close to the point of jump out, but typically also have R-square values of > 0.998. Small drifts that occur in approaches below the baseline will also have an impact on the measured force. These arise as a result of large external vibrations or thermal fluctuations despite the measures

described above, and result in an offset in the absolute force value that may be positive or negative. In order to minimise the effect of these vibrations, the majority of presented measurements take place outside of normal working hours, such that the measurement environment is more quiet. At lower forces, these effects combine to give rise to a variation in force measurements of ~ 0.1 mN m^{-1}.

At higher forces, there is greater variation between runs. This likely arises as a result of non-linearity in the actuators, which can show deviations from linear motion after running for long time periods when probing high force regions of the force profile. Such effects are not large in retractions, where the baseline is set close in time to the point of jump-out. However, these effects can be very substantial during approaches where the baseline is set very far away in time from the point at which the innermost layering positions are reached, and can give rise to errors on the order of ~ 0.5 mN m^{-1}.

In total, these errors give rise to small variations between and within runs probing identical systems. As a result, no averaging of runs is performed, as this would lead to a 'smearing out' of the subtle effects captured by individual runs, and the majority of force profiles presented in this work are in the form of single experimental runs that are representative of the whole. Within a single force profile, errors in absolute distance are ~ 0.5 nm and in absolute normalised force are ~ 0.1 mN m^{-1}, however within a single run, errors in relative distance are ~ 0.2 nm and in relative normalised force are $\sim 10^{-3}$ mN m^{-1}. We ensure to take steps to minimise this error where possible, however this must be done without compromising other aspects of the experiment. Overall, this method produces reproducible results that give direct measurements of liquid behaviour.

2.2 | Bulk Measurements

The measurements of bulk structure carried out in this work were performed using coherent elastic neutron scattering at the ISIS beamline in Harwell, UK. In this technique, neutrons are generated at a source, focused into a beam, and directed towards the sample of interest. Collisions between the neutrons and the atoms within the sample result in the scattering of the neutrons in a pattern characteristic of the structures present within the sample. Analysis of this scattering pattern allows conclusions to be drawn about the structures and correlations present in the sample medium.

2.2.1 | Neutrons and Neutron Production

Neutrons are a form of subatomic particle that carry no charge and are found, alongside protons, in the nuclei of all atoms (with the exception of ^{1}H which consists of a single proton and no neutrons). They were first observed in 1932 by James Chadwick, who noticed an uncharged and highly penetrating radiation emitted by α particles incident on beryllium[97,98]. He concluded that the beryllium nuclei absorbed the α particles, forming the unstable isotope ^{13}C, which decayed into ^{12}C and an uncharged neutron:

$$^{9}\mathrm{Be} + {}^{4}\mathrm{He} \longrightarrow {}^{13}\mathrm{C} \longrightarrow {}^{12}\mathrm{C} + \mathrm{n} \tag{2.5}$$

The properties of neutrons, compared with other subatomic particles are shown in table 2.1.

It is the highly penetrating nature of neutrons that makes them useful for scattering. Because neutrons are uncharged and much heavier than electrons, they are not affected by the electron density around an

Table 2.1: Properties of subatomic particles

Property	Proton	Neutron	Electron
Mass / kg	1.673×10^{-27}	1.675×10^{-27}	9.109×10^{-31}
Charge / e	+ 1	0	− 1
Spin	1/2	1/2	1/2

atom, and are instead only scattered by atomic nuclei.

Free neutrons are unstable particles, and will decay to a proton, an electron, and an anti-neutrino, as shown in equation 2.6. The half life of a free neutron is about 10 minutes.

$$n \longrightarrow p^+ + e^- + \overline{\nu}_e \tag{2.6}$$

In order to perform neutron scattering, a large scale, reliable neutron source is therefore needed that can produce neutrons for measurements as required. These are usually either fission or spallation sources[99].

Nuclear fission reactors use a fuel of fissile material that is able to undergo nuclear fission, such as uranium, thorium or polonium. When the heavy atoms decay into lighter nuclei, they emit heat and free neutrons. In a reactor, the emitted heat is captured and used to generate electricity, usually by heating water to steam, causing a rise in pressure that turns a turbine, generating electricity. A self sustaining fission reaction will take place if one of the emitted neutrons goes on to cause further nuclear decay by being absorbed by the fuel material, forming a very unstable nucleus that can rapidly undergo fission. The remaining neutrons will either also be absorbed, setting off other fission reactions, or will escape from the surface of the reactor. These neutrons may be directed towards instruments using a series of moderators (materials

that slow down neutrons) and reflectors (materials that reflect neutrons) and used in scattering experiments.

Spallation neutron sources work in a very different way to fission sources. In a spallation source, some form of particle accelerator is used to generate pulses of protons accelerated to an appreciable fraction of the speed of light. These are focused onto a target, generally tantalum, tungsten or some other heavy metal. When the proton pulse collides with the target, the protons are absorbed by heavy metal nuclei. A nucleus that has absorbed a high energy proton undergoes a series of nuclear reactions, ejecting new particles including neutrons, that go on to be absorbed by other nuclei. Eventually, all the excited nuclei relax by emitting further, low energy neutrons. These neutrons can then be directed through moderators towards instruments.

In this work, all neutron scattering data was collected at the ISIS Neutron and Muon Source at the Rutherford Appleton Laboratory in Harwell, UK[100]. The neutrons are produced in a spallation source by the following method: hydrogen and caesium gases are mixed in the presence of an electric arc. This forms a plasma, from which hydride ions, $^{1}H^{-}$, are extracted and focused into a beam. These are accelerated by a linar accelerator (LINAC), where alternating electric fields generated by dipole magnets accelerate pulses of hydride ions to 37 % the speed of light. The pulses are directed from the LINAC through an aluminium foil, which strips electrons from the hydride ions, yielding a beam of protons. These pulses of protons finally enter a synchrotron, a ring of dipole electromagnets that may be switched on and off in such a fashion as to further accelerate the protons. After 12,000 revolutions within the synchrotron the protons are moving at 84 % the speed of light. At this point, a magnet is used to eject the pulse of protons. These are

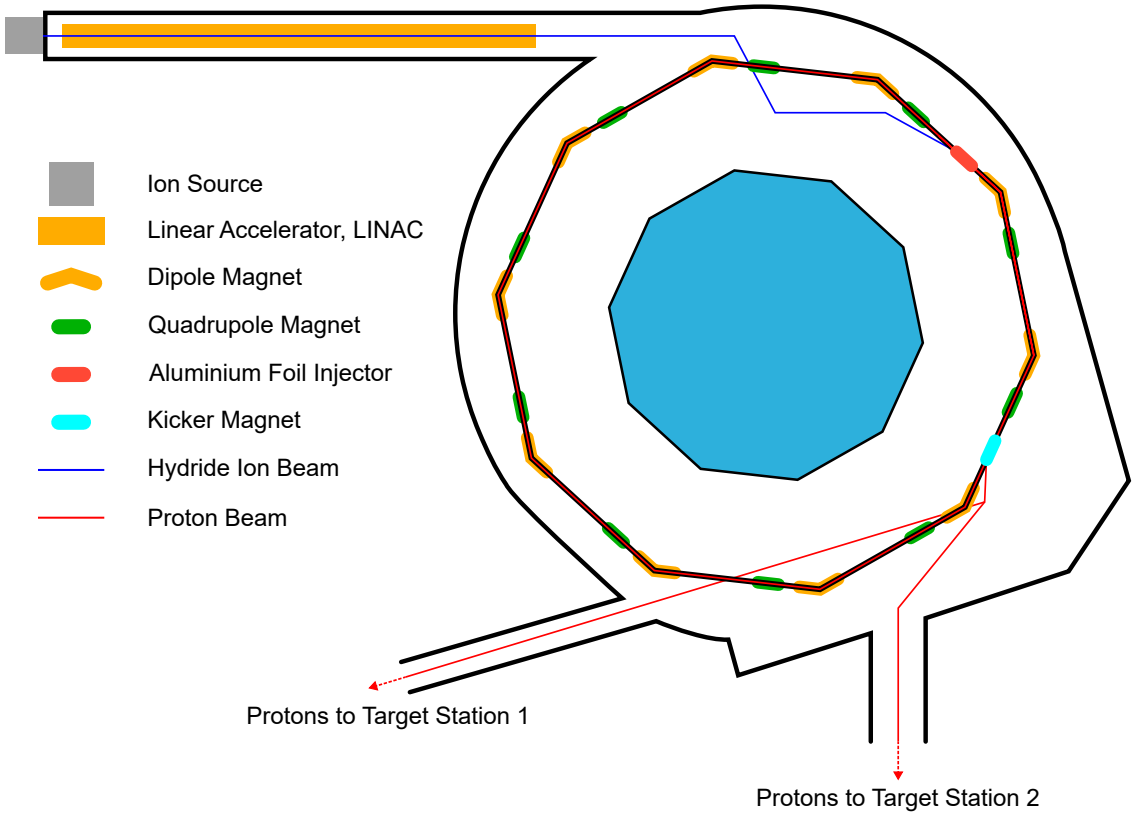


Figure 2.10: Cartoon of the ISIS synchrotron: Hydride ions are produced at the ion source and accelerated to 37 % the speed of light by a LINAC. The hydride ions are stripped of their electrons by passing through a sheet of aluminium foil and injected into the synchrotron. The resulting proton beam is accelerated to 84 % the speed of light, then kicked from the synchrotron by the kicker magnet and sent towards the targets on either target station 1 or 2.

focused down one of two beamlines, towards tungsten targets. The collision of the proton beam with the target produces neutrons that are then used for scattering experiments. A schematic of the synchrotron at ISIS is shown in figure 2.10.

For this work, experiments were carried out on the Near and InterMediate Range Order Diffractometer, NIMROD, which is situated on Target Station 2. Neutrons arrive at NIMROD after passing through moderators of liquid water or liquid hydrogen, giving a broad range of neutron energies.

2.2.2 | Diffraction and Neutron Scattering

When a wave passes an obstacle or through an aperture, it spreads out, or diffracts. The amount the wave diffracts is related to the wavelength of the wave and the size of the gap the wave is diffracting through: an aperture that is of similar size to the wavelength leads to effective diffraction, with the emerging wave resembling an arc wave with a point source in the centre of the slit; while a gap that is much larger than the wavelength of the incoming wave will lead to the wavefronts continuing without much change, with diffraction only taking place in the regions close to the edge of the aperture. This is shown in figure 2.11 (a) and (b).

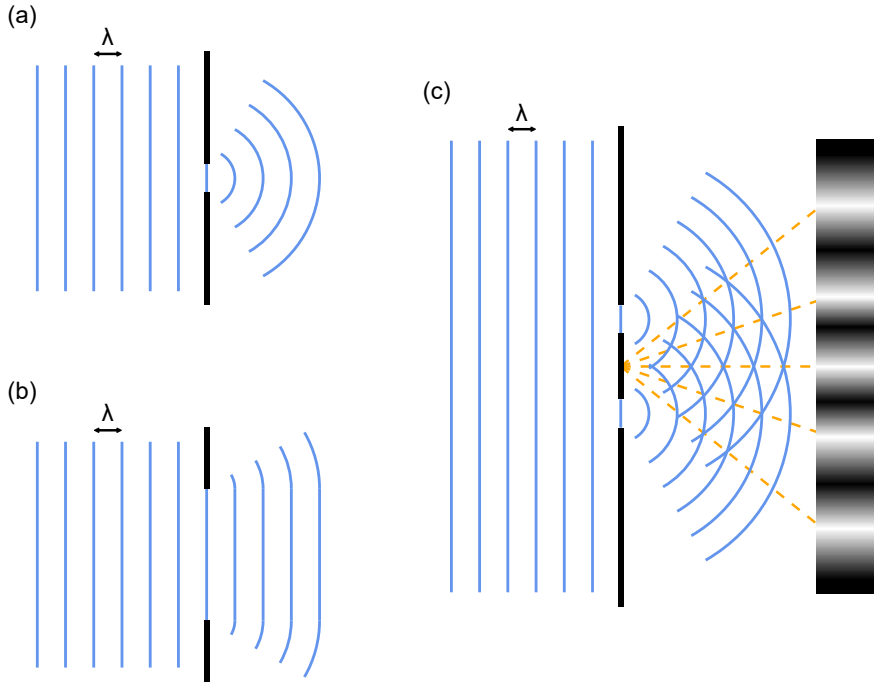


Figure 2.11: Diffraction of a wave in different circumstances. Wavefronts are shown as blue lines, and the wave has a wavelength λ. (a): The effect of diffraction when the aperture size is similar to λ. (b): The effect of diffraction when the aperture size is much greater than to λ. (c): When a wave passes through a double slit, the emerging diffracted waves interfere with each other, giving rise to the shown diffraction pattern. Peaks arise where each wave has travelled an integer number of wavelengths, with the difference between the wavelengths travelled corresponding to the order of the diffraction peak.

When a wave passes through two slits where the slits are com-

parable to the wavelength, the result of the diffraction is that each of the emerging arc waves interferes with the other. These interferences lead to alternating patterns of high and low intensity, shown in figure 2.11 (c). The spacing of these bands of high and low intensity is related to the distance between the slits that the waves pass through. If d is the distance between the two slits, then the spacing of the fringes w at a distance z from the slits is given by:

$$w = \frac{z\lambda}{d} \tag{2.7}$$

as long as $z \gg d$. This effect was first noticed in 1801 by Thomas Young, who was able to produce the diffraction pattern in sunlight, and provided evidence for the wave nature of light[101]. It is this principle that allows structure to be determined from the diffraction, or scattering, of a wave.

A collection of atoms in which there exists some form of order can act to diffract, or scatter, a wave. Therefore, in order to maximise diffraction and give the clearest relation between the scattering distances and the atomic separations, a wave with wavelength similar in magnitude to the distances between atoms is required. Atomic separation is typically of Ångström order, ~ 1 Å, in condensed matter. In the electromagnetic spectrum, this corresponds to x-ray wavelength radiation, and indeed, x-ray scattering is often used to find structural information of condensed matter systems[102–105]. One drawback of the use of x-rays for this purpose is that, as an electromagnetic wave, x-ray radiation interacts with, and is scattered by, regions of charge density. As such, x-rays are very useful for picking out the locations of large atoms, as they have lots of electrons so dominate in the resulting scattering pattern, but peaks arising from atoms with few electrons, such as hy-

drogen, can often get lost in those from heavier elements. A solution to this is to use neutrons as the scattering wave, as neutron scattering is dependent on the nuclear identity, rather than the number of electrons.

Neutrons are most commonly thought of as a particle, however, they can also behave as a wave. This is just one conclusion of a more general fundamental concept of modern particle physics, known as wave-particle duality, in which waves can exhibit particle-like properties and particles the properties of waves. Wave-particle duality has its origins in the work of Louis de Broglie in the 1920s[106,107], who showed that the wavelength of a wave associated with a particle is inversely proportional to the momentum p of the particle:

$$\lambda = \frac{h}{p} = \frac{h}{mv} \tag{2.8}$$

where h is Planck's constant, m the particle mass, and v the particle velocity. Hence, neutrons too can be thought of as a wave, and indeed measurements have been able to reproduce wave-like behaviour from the diffraction, or scattering, of neutrons through a double slit[108]. As such, by controlling the neutron velocity, a wave of neutrons with a wavelength similar to that of atomic separations can be generated.

Neutrons carry no charge and are not a form of electromagnetic radiation, so are not scattered by the electron cloud around an atom. Instead, neutrons are scattered directly by the atomic nuclei, through an interaction mediated by the nuclear strong force. This means the diffraction pattern generated by a beam of neutrons passing through a sample carries information on the location of the nuclei of atoms in the sample. The geometry of a scattering experiment is shown in figure 2.12.

A neutron of wavelength λ enters the sample and is scattered by an

ordered structure of length scale d within the sample. It emerges at an angle 2θ from it's incident direction. From Bragg's law:

$$n\lambda = 2d\sin(\theta) \tag{2.9}$$

where n refers to the diffraction order as shown in figure 2.11, and can be set to unity when considering the first diffraction peak. The scattering is equivalent to a change in the momentum vector, $\vec{p}$. From equation 2.8, $\vec{p} \propto \lambda^{-1}$, so rather than thinking in terms of the wavelength of the wave, it is often useful to think in terms of the wave vector, $\vec{k}$

$$\vec{k} = \frac{2\pi}{\lambda} \tag{2.10}$$

which is directly proportional to the momentum of the wave.

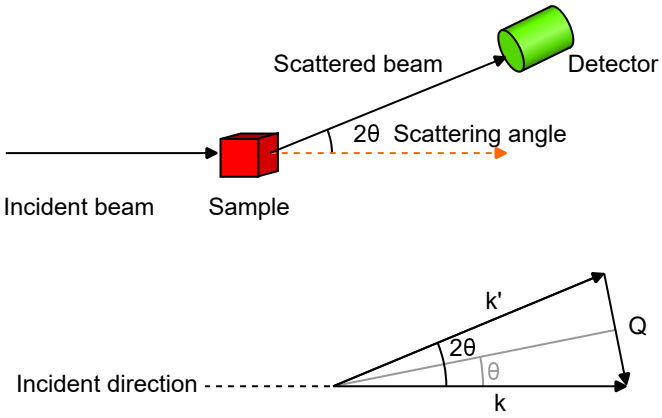


Figure 2.12: The geometry of an elastic neutron scattering experiment. Neutrons incident to the sample with an initial wave vector k are scattered by an angle 2θ to a new wave vector $\vec{k}'$. In an elastic scattering event, $|\vec{k}| = |\vec{k}'|$, so $\vec{Q}$ can be determined from trigonometry.

The change in momentum of a scattering event is given by Q

$$\vec{Q} = \vec{k} - \vec{k}' \tag{2.11}$$

Hence, for an elastic collision in which the magnitude of the momentum

is unchanged ($|\vec{k}| = |\vec{k}'|$), it can be shown from trigonometry that

$$|\vec{Q}| = 2|\vec{k}|\sin\theta = \frac{4\pi}{\lambda}\sin\theta \tag{2.12}$$

and, by comparison with equation 2.9, that

$$d = \frac{2\pi}{|\vec{Q}|} \tag{2.13}$$

Hence, from knowledge of $\vec{Q}$ in elastic scattering events, the distances associated with order, or correlations within a sample can be found. Signal resulting from inelastic scattering events must be corrected for after the experiment.

From the above derivation, it is clear that $\vec{Q}$ is related to the angle through which an elastically scattered neutron is scattered. In order to understand the probability that a neutron scatters in this way, it is necessary to measure the neutron flux at each angle. This property is know as the differential cross section:

$$\frac{\mathrm{d}\sigma}{\mathrm{d}\Omega} = \frac{\text{No. neutrons scattered per second into angle } \mathrm{d}\Omega}{I_0 \mathrm{d}\Omega} \tag{2.14}$$

where I_0 is the incident neutron flux per unit area of sample per second. The differential cross section has dimensions of area, with units typically in barns where 1 barn = 10^{-28} m^2. This unit has its origins in the Manhattan project during the Second World War, where physicists joked that this tiny area was in fact a large target for a subatomic particle, as in the expression 'couldn't hit the broad side of a barn'. The name stuck after the war. Regardless, in order to obtain structural information about the sample through which the neutron beam is incident, it is necessary to plot differential cross section against Q.

In a neutron scattering experiment, the probability that a neutron is scattered by a nucleus is given by the scattering length, b of the nucleus. The value of b is sensitive to the number of protons and neutrons within a nucleus in a non-trivial manner, and as such, neutron scattering experiments are not only element, but also isotope sensitive, and can be positive or negative. However, neutrons carry a spin of 1/2, which can interact with the spin of the scattering nucleus, resulting in an associated standard deviation with b. This results in incoherent scattering that is independent of the scattering angle, and must be corrected for after an experiment.

2.2.3 | The NIMROD Instrument

Neutron scattering data described in this work was collected on the Near and InterMediate Range Order Diffractometer[109], on target station 2 of the ISIS neutron beam line in Harwell, UK. It uses neutrons generated at the ISIS synchrotron (shown in figure 2.10) over a broad range of wavelengths and can detect them over a large angle range. In total, this allows the instrument to probe a Q range of 0.02 to 50 $Å^{-1}$, corresponding to a distance range of 0.15 to over 300 Å.

Neutron detection is carried out by an array of scintillation detectors that emit light upon capturing an incident neutron. The detector contains layers of ^{6}LiF dispersed in ZnS. When a ^{6}Li nucleus absorbs a neutron, it decays, emitting secondary particles, shown in equation 2.15.

$$^{6}\mathrm{Li} + \mathrm{n} \longrightarrow {}^{4}\mathrm{He} + {}^{3}\mathrm{H} \tag{2.15}$$

These particles are strongly ionising, and remove core electrons from the ZnS. This causes outer-shell electrons to relax to the core orbitals, which emits light and is detected by a photodetector.

Samples are placed within the instrument in a can made from an alloy of titanium and zirconium (TiZr) at a molar ratio of 7.16:3.438. This ratio is chosen as the coherent scattering length of titanium $b_{\mathrm{coh,Ti}} = -3.438 \times 10^{-15}$ m while the scattering length of zirconium $b_{\mathrm{coh,Zr}} = 7.16 \times 10^{-15}$ m . As such, at this ratio, the mean coherent scattering length of the can falls to zero and has minimal effect on the collected data[99].

As discussed above, in order to obtain a picture of the structures and correlations present within a sample, only elastic, coherently scattered neutrons are required. However, neutron detectors record all neutrons regardless of their origins, so corrections to the data need to be made. These corrections also remove any small contribution to the scattering from the sample cell. This is done by considering the density and isotopic contents of the sample, and by comparing the collected data from the sample with:

- the chamber background
- a vanadium standard for calibration
- the empty sample can

This process is exceptionally complex, and is completed using the program Gudrun, more details on which can be found in the technical report by Alan Soper[110].

2.3 | Additional Measurements

In order to carry out work in the methods described above, certain physical data is often needed relating to the samples of interest. The methods used to collect these data are described here, and are vital to the

interpretation of the majority of the experimental data shown throughout the rest of this thesis.

2.3.1 | Refractive Indices

The refractive index n of a substance describes the ability of that substance to bend the path of light passing through it. It also describes the factor by which the speed of light passing through that medium is reduced. Thomas Young, of double slit experiment fame, was the first to coin the term “index of refraction"[111], though many great minds of history have also studied this effect.

Many refractive indices are tabulated, and when literature values for refractive index could be found they were used, however in some cases, such as for highly concentrated solutions and mixtures, no literature data could be found. For this reason, it was important to measure some refractive indices over the course of this work.

Measurements were taken on an Abbe 60 Refractometer (Bellingham + Stanley). Briefly, a few drops ($\ll$ 1 ml) of liquid is confined between two prisms, an illuminating prism and a measuring prism and monochromatic light from a sodium lamp is shone onto the illuminating prism. This prism is ground to give a rough surface at the prism-liquid interface, meaning that the surface becomes a source of light that can pass through the liquid at all angles. The measuring prism has a smooth ground surface. Light entering the measuring prism does so as a cone with a critical angle defined by the ratio of the refractive indices of the liquid and the medium. This cone of light is directed through a series of lenses to a telescope eyepiece. By moving the lenses, the edge of the cone of light may be found, from which the critical angle and thus the refractive index of the medium can be calculated. The basic features of

an Abbe refractometer are shown in figure 2.13.

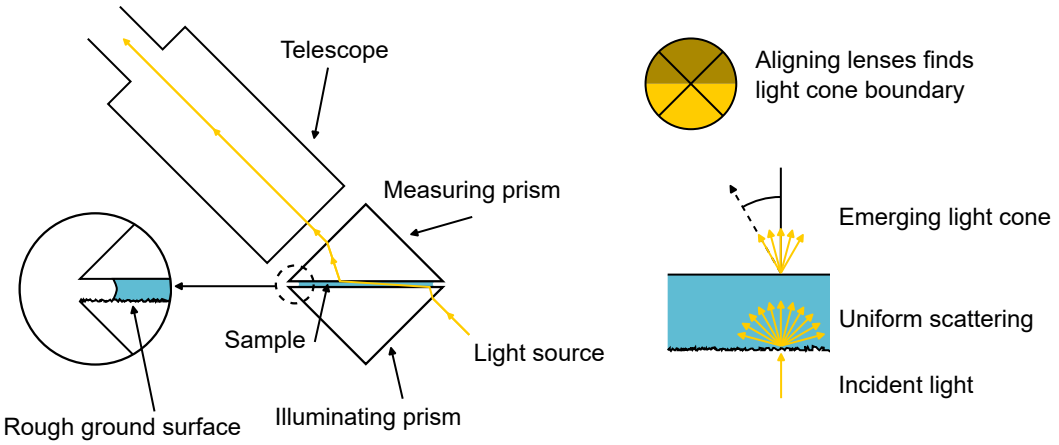


Figure 2.13: Schematic of an Abbe refractometer used in this work. Light enters the sample from the rough illuminating prism surface and is uniformly scattered. The refracted light enters the measuring prism as a cone of well defined angle. The light is focused into a telescope, containing lenses. Aligning the lenses such that the boundary of the cone can be found yields the refractive index of the sample.

2.3.2 | Densities

The density of a substance is the mass per unit volume of that substance. Density has been studied since time immemorial, with one particularly famous example taking place in Syracuse in the third century BCE, when the king asked the scholar Archimedes to measure the gold content of a crown to check whether or not the royal goldsmith was embezzling gold. On taking a bath to think over the problem, Archimedes noticed that the water rose up the side of the tub upon immersion of an object, giving a way to calculate volume, which could then be related to mass through the density.

As with refractive index, many densities of substances are tabulated in the literature, however for concentrated salt solutions this is not the case, and densities must be measured. In this thesis, density measurements were made on a density meter (Anton Paar). Briefly, a small amount of sample ($\sim$ 1 ml) is inserted into a U-shaped tube. The tube

is excited and oscillates at a sample-dependent frequency. From this frequency, the density of the sample can be determined.

3 | Surface Forces in a Water-in-Salt Electrolyte

Water-in-salt (WiS) electrolytes emerged relatively recently as a class of super-concentrated aqueous electrolyte. They were first defined in 2015 by Liumin Suo and colleagues[26] as an electrolyte in which the salt comprises the majority of the mass and volume of the aqueous liquid system. This chapter details measurements of forces and structures that appear at interfaces in WiS electrolytes of lithium bis(trifluoromethanesulfonyl)-imide ($LiNTf_2$, structure shown in figure 3.1), and discusses the implications of these measurements. The work shown in this chapter was first published in 2021, under the title “Surface Forces and Structure in a Water-in-Salt Electrolyte"[62].

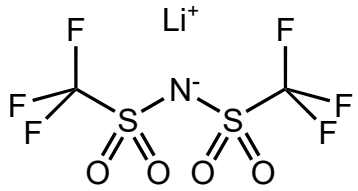


Figure 3.1: Structure of lithium bis(trifluoromethanesulfonyl)imide, $LiNTf_2$. The hydrophilic cation and bulky delocalised anion ensure high solubility in water.

3.1 | Background and Motivation

Water-in-salt electrolytes are exceptionally concentrated aqueous electrolytes, and as such represent a large departure from the well understood areas of dilute electrolyte physics, as discussed in chapter 1. Their study aims to shed light on this high concentration electrolyte regime. Beyond this, WiS electrolytes are of interest due to their potential applications in batteries.

State-of-the-art lithium-ion batteries are an increasingly important part of modern society. They have high energy densities, long lifetimes, and can be tailored for use in specific applications which makes them very attractive in a wide range of products, from laptops and smart phones to electric vehicles and large scale grid energy storage[112–114]. The high energy density arises because lithium electrolytes have a low mass per unit charge carrier, and because the solvents and anions utilised in lithium-ion batteries can be favourably degraded at the electrode surfaces to create a passivating film at the electrode[115]. This film protects the rest of the electrolyte from the high potentials applied at the electrode but still allows for lithium ion conduction to the electrode surface, allowing the electrolyte to function over a wide range of potentials. However, concerns about safety continue to hinder the dominance of lithium-ion batteries[116–118]. The concerns arise as the electrolytes employed in lithium-ion batteries tend to use water-sensitive salts and flammable solvents, where small degradations to the battery integrity can lead to run-away reactions and explosions. One solution to this is to use water as the solvent in battery electrolytes.

3.1.1 | Aqueous Lithium-Ion Batteries

Aqueous lithium ion batteries have been of interest for some time[119], however the narrow electrochemical stability window (ESW, the range of potentials over which a substance is stable to oxidation or reduction) of water has kept the energy density of water based systems low. Conventional organic electrolytes are able to display large ESWs owing to their ability to generate a passivating film at the electrode surface. The challenge then is to develop aqueous electrolytes that are able to deposit a passivating film at the electrode.

Water-in-salt electrolytes are able to form passivating films in aqueous environments through the degradation of organic anions, and as such are viewed as promising candidates to replace unsafe organic electrolytes in future lithium-ion batteries[26,120–122]. They have been able to show large extensions of the ESW, from 1.23 V in pure water, to $\sim$ 3 V, with further extensions to this the focus of much research[123–125]. Since their initial discovery, the principle of WiS electrolytes has been extended to many other battery chemistries, including those of sodium[125–127], potassium[128,129], aluminium[130,131] and zinc ions[132,133], and to battery electrolytes comprising mixtures of high concentration salts[120,121,124,125].

3.1.2 | Water-in-Salt Electrolytes at Interfaces

Of key interest to the study and commercialisation of these systems is the behaviour of these electrolytes at interfaces. This will provide clues as to the nature of the formation of the passivating film and the mechanisms of lithium ion transport within these systems, and is particularly relevant as the behaviour of WiS electrolytes at interfaces is not yet fully understood[134].

Calculations and measurements have probed the formation mechanisms of the passivating film, showing the importance of water in these systems[135,136], whilst others have highlighted the importance of water- and ion-rich domains close to the battery electrodes[137], and worked to develop models of WiS electrolytes[138,139]. Studies have also used surface force measurement techniques to investigate interfacial properties of WiS electrolytes. AFM and SFB studies across thin films of WiS and mixed salt systems have revealed oscillating structural forces similar to those observed in ionic liquids[63,140], while AFM works have highlighted

the importance of the ion identities[141] and surface properties[142] on the behaviour of the oscillating forces.

Many of these studies focus on aqueous solutions of lithium bis-(trifluoromethanesulfonyl)imide, $LiNTf_2$, however a consistent picture of this electrolyte at interfaces is yet to emerge, and as such it remains an interesting and important case for further study.

3.2 | Experimental Details

We investigated the surface forces and structures present in aqueous $LiNTf_2$ over a broad concentration range. Our experiments were performed using the SFB as described in chapter 2, using approach and retraction velocities of 0.5 - 20 nm s^{-1}. Here, details specific to these experiments are discussed.

3.2.1 | Materials and Solution Preparation

The structure and dimensions of $LiNTf_2$ are shown in figure 3.2, alongside the aqueous phase diagram of the salt, with the concentrations investigated in this study highlighted. Solutions of aqueous $LiNTf_2$ were prepared from freshly opened bottles of $LiNTf_2$ (Fluorochem, 99 %) in ultrapure water (Millipore, 18.2 MΩ cm, TOC < 3 ppb). Preparation took place in an LFH using acid-cleaned tools and glassware to minimise contamination.

Measurements were made at three concentrations: 5 m, 8 m, and 12 m, where m refers to the molal concentration, the moles of salt per kilogram of water, mol kg^{-1}. Multiple measures of concentration are compared in table 3.1. At each concentration, multiple experimental runs were carried out across multiple contact spots on the same pair of mica surfaces, and repeats of each concentration were performed

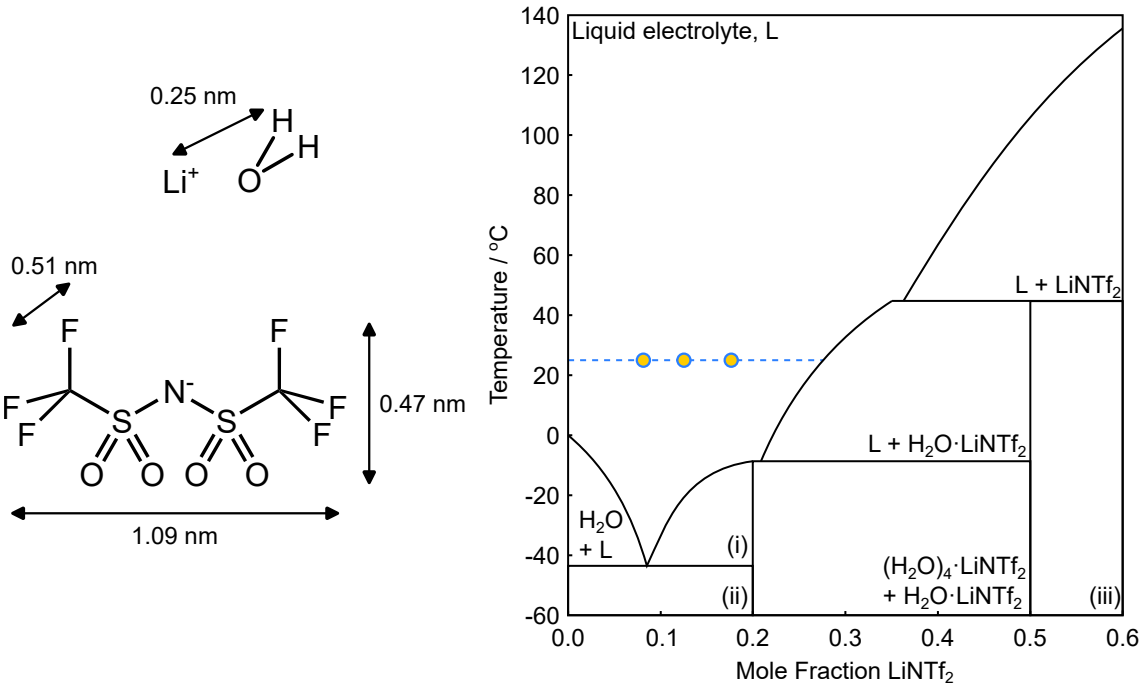


Figure 3.2: *Left:* Approximate dimensions of lithium-water primary hydration shell and NTf_2^- anion, with length scales calculated from Van der Waals radii[68] and neutron scattering experiments[143]. *Right:* Phase diagram of aqueous $LiNTf_2$, as experimentally found by Ding *et. al.*[144]. Concentrations investigated in this study are shown by the yellow circles. (i) - L + $(H_2O)_4 \cdot LiNTf_2$, (ii) - H_2O + $(H_2O)_4 \cdot LiNTf_2$, (iii) - $H_2O \cdot LiNTf_2$ + $LiNTf_2$.

on at least one other pair of mica surfaces with a fresh solution to ensure reproducibility. This range of concentrations was chosen because a 5 m solution of $LiNTf_2$ represents the limit of the WiS regime, where the mass of the water and salt are equal, while at concentrations above 12 m, solutions proved resistant to measurement, either through additional contaminant concentration or because of confinement induced

Table 3.1: Concentrations of aqueous $LiNTf_2$ studied in this work on different concentration scales

Molal Concentration, m / mol kg^{-1}	Molar Concentration, M / mol dm^{-3}	$LiNTf_2$ mole fraction	H_2O/Li molar ratio
5	2.9	0.08	11.1
8	3.7	0.13	6.9
12	4.4	0.18	4.6

crystallisation.

3.2.2 | Refractive Indices

Refractive indices were measured as described in chapter 2. A measurement was made on each solution multiple times to ensure reproducibility, and recorded. Refractive indices measured in this work are detailed in table 3.2.

Table 3.2: Refractive indices of aqueous $LiNTf_2$ solutions. All refractive indices quoted have an error of ± 0.0001.

Molal Concentration / mol kg^{-1}	Refractive Index	Temperature / ^{o}C
5	1.3562	24.2
8	1.3621	22.6
12	1.3694	21.3

3.3 | Surface Forces Measurements and Discussion

Normal forces recorded at three concentrations in aqueous $LiNTf_2$ are shown in figure 3.3 for small surface separations. Forces are normalised by the radius of curvature of the lenses at the measurement spot such that the recorded forces are independent of the surface geometry (see equation 2.1), and forces are distinguished by whether they are measured during an approach of the surfaces or during a retraction.

On approach of the surfaces at each concentration, we observe a series of repulsive hard walls that require an increasing amount of force to overcome, extending to surface separations of $\sim$ 7 nm. Retraction of the surfaces from each hard wall reveals an adhesive well. Once the maximum of one wall is reached, the surfaces jump onto the face of the next wall, while the surfaces jump apart to a large separation at the minimum of each well. These jumps arise from the spring instability

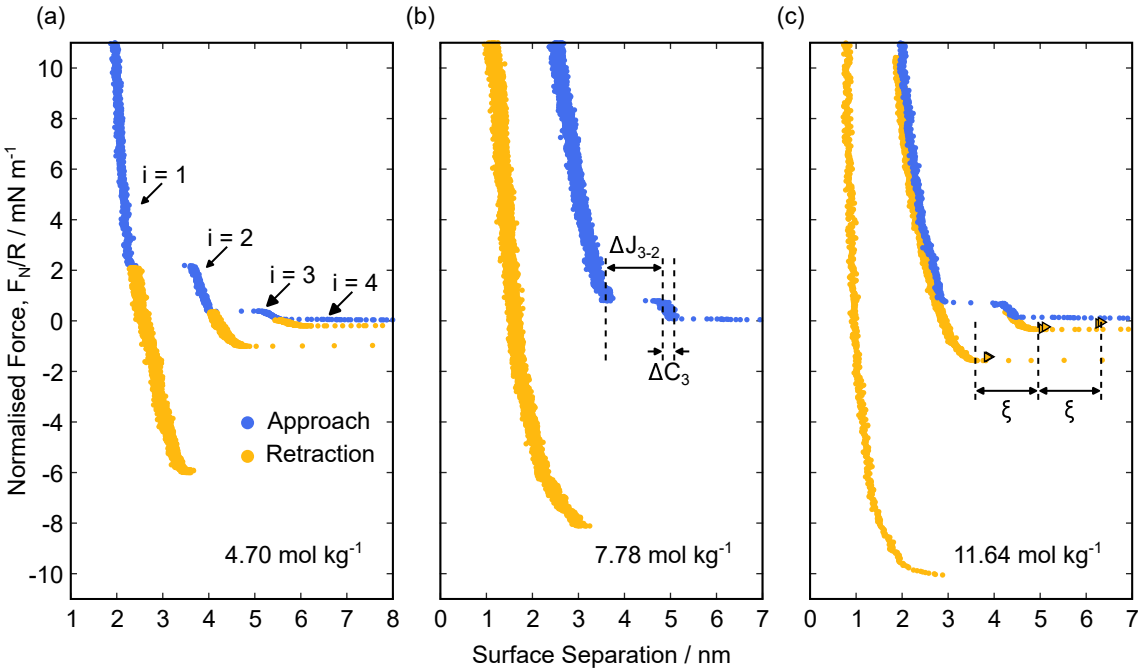


Figure 3.3: Force profiles of increasing concentrations of $LiNTf_2$ WiS electrolyte. Forces are normalised by the radius of curvature of the lenses. Forces measured on approach of the SFB surfaces are shown in blue, while those measured on retraction are shown in yellow. The exact concentration of each system is shown: (a): 4.70 m, (b): 7.78 m, and (c): 11.64 m. At each concentration, layers are seen, with compressions within layers and jumps between layers. Layers are labelled as $i = 1$ at closest approach, while compressions are labelled ΔC_i and jumps are labelled $\Delta J_{i-(i-1)}$. The layers can be interpreted as an oscillating function with an oscillatory wavelength defined by ξ. Jump out positions and calculated forces measured using the static retraction technique are shown as triangles.

inherent within the technique, and as such the region of the force profile between the maximum of layer i and the minimum of layer $i-1$ is inherently unmeasurable. Despite these gaps, it is clear that this region of the force profile has the form of a decaying oscillation, and suggests that a well defined, ordered liquid structure is present at the liquid-mica interface. As such, we label this region of the force profile the 'structural force'.

At smaller forces, we observe a long range, monotonically decaying exponential force, highlighted in the logarithmic distance scale plots of figure 3.4. The characteristic decay length of this force increases with increasing concentration. This force is much smaller in magnitude

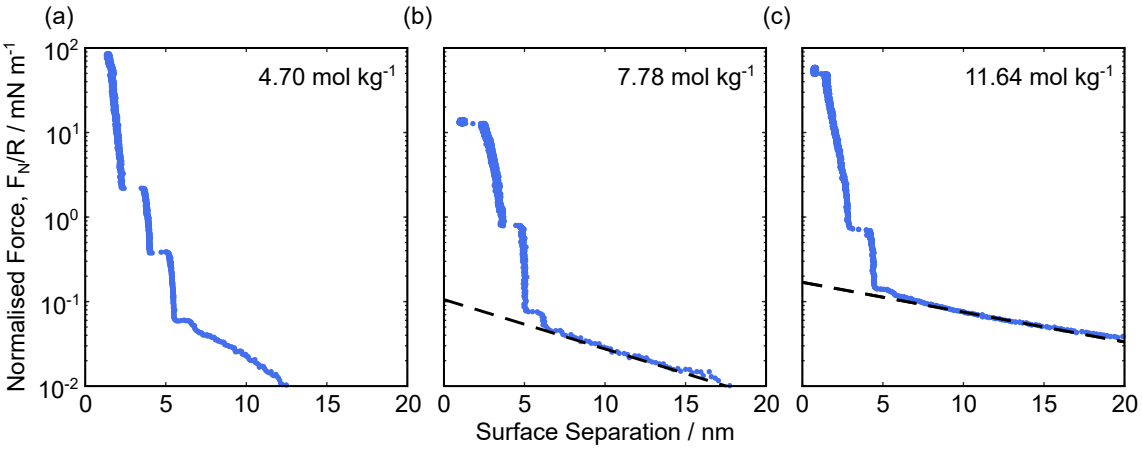


Figure 3.4: Force profiles of increasing concentrations of $LiNTf_2$ WiS electrolyte plotted on a logarithmic force scale. Forces are again normalised by the radius of curvature at the measurement spot and exact concentrations are shown. The exponential screening force is obscured at long ranges by thermal drift at the lowest concentration (a), but the gradient of the exponential force is highlighted by the dashed line at higher concentrations in (b) and (c).

than the structural force, and is only measurable at surface separations where the structural force has decayed substantially. As such, we label this region of the force profile the 'long range force'.

3.3.1 | Fitting Normal Force Profiles

A force profile containing a decaying oscillatory term is well known in surface force experiments for a range of systems and liquids, from non-polar organic liquids[22,46], through dilute aqueous electrolytes[53,54], to concentrated aqueous electrolytes[59,60] and ionic liquids[24,66–73]. Decaying oscillations have also been predicted theoretically to arise both in pure liquids and in electrolytes, either from density fluctuations in pure liquids and high concentration electrolytes, or from charge-charge interactions[145,146].

Longer range, exponentially decaying forces are also known to arise between surfaces. Most famously, in the case of dilute electrolytes, the interaction between ions and charged surfaces follows Debye-Hückel behaviour[7], as captured in DLVO (Derjaguin, Landau, Verwey and Over-

beek) theory[13,14], and leads to a long range exponential force that is repulsive between like-charged surfaces. These forces have previously been measured in dilute ($<$ 0.1 mol dm^{-3}) aqueous electrolytes within the SFB[52,54]. However, the forces described by Debye-Hückel theory are expected to become very short range as the concentration is increased ($<$ 0.1 nm for the concentrations investigated here), so the behaviour observed cannot come from these dilute arguments.

Nevertheless, we observe two contributions to the total force; a decaying oscillatory structural force and a long range monotonically decaying exponential force. As such, these forces can be fitted against surface separation D using the following equation:

$$\frac{F_N}{R} = A\ e^{-D/\lambda_o}\ \cos\left(\frac{2\pi}{\xi}(D+\delta)\right) + B\ e^{-D/\lambda_s} \tag{3.1}$$

The first term in equation 3.1 describes the structural force, where A is the magnitude of the force, λ_o describes the decay of the oscillatory window, ξ describes the oscillatory wavelength, and δ describes an offset in the oscillations. The second term describes the long range force, where B is the magnitude of the force and λ_s describes an exponential screening length. The force is normalised by the radius of curvature of the contact spot, again to allow comparisons between measurements and to the interaction free energy per unit area between parallel plates.

From figure 3.4, it is clear that the intercept of the long range force, B, is much smaller than the intercept of the oscillatory force, A, but that the oscillatory force decays over much shorter ranges than the long range force. Therefore, when fitting these forces, it is reasonable to assume that at the short range, the contribution to the overall force from the long range force is negligible, while at long range the contribution to the overall force from the oscillatory force is negligible. This

provides a pathway for the fitting of equation 3.1 for any concentration. An example of the fitting process for a measurement on 11.64 m aqueous solution of $LiNTf_2$ is shown in figure 3.5, while the total fit is shown superimposed on the measured force profile in figure 3.6.

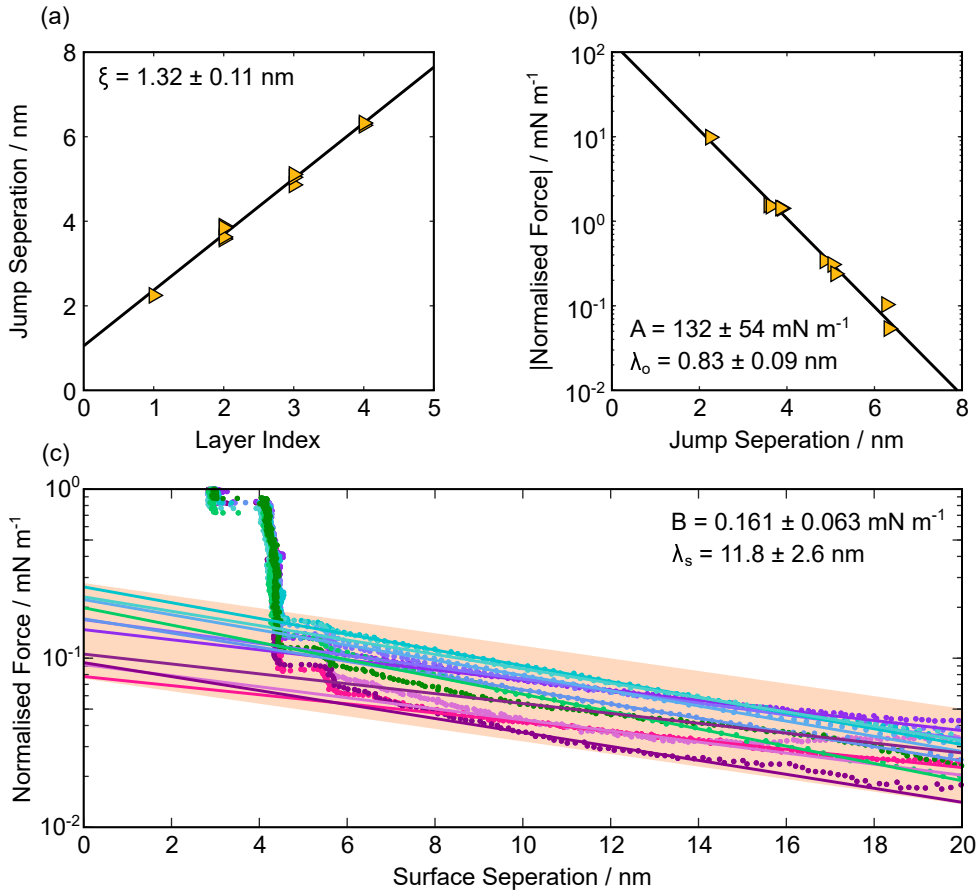


Figure 3.5: Fitting process for a measurement on 11.64 m aqueous $LiNTf_2$. (a): Surface separations of jump out positions are plotted against layer index. The wavelength of oscillations is given from the gradient. (b): Adhesive forces plotted against jump out positions. The magnitude of the structural force is given by the intercept, while the characteristic decay length of the oscillations is given by the gradient. (c): Multiple slow approach force profiles are shown on a logarithmic force scale. Fits of each run at separations from 9 to 15 nm, shown by the solid lines, give a magnitude and decay length of the long range force for each run, with the mean values and standard deviations for the long range force parameters shown.

In general, the form of the generated fit matches closely the measured force profile at low forces and at addhesive minima, however deviations occur at larger compressive forces. These deviations arise as the glue layer in the lens set up is slightly deformable. At high loads,

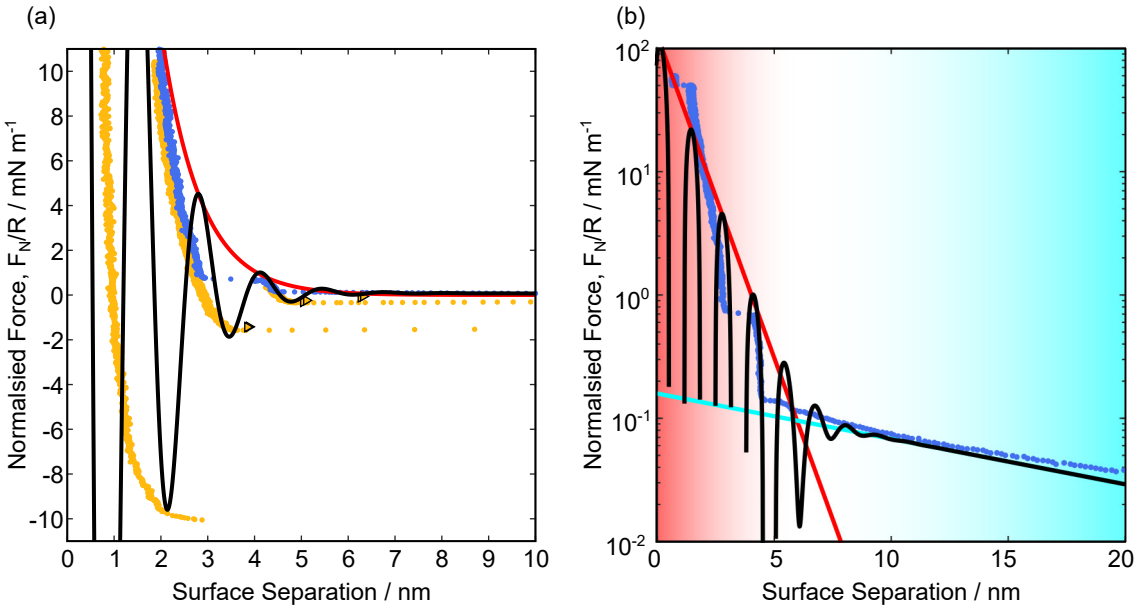


Figure 3.6: Data and fitted force profile for a measurement on 11.64 m aqueous $LiNTf_2$ shown on a linear (a) and logarithmic (b) force scale. The fit follows equation 3.1, with parameters calculated in figure 3.5. The decay of the oscillatory force is shown by the red line, the decay of the long range force is shown by the pale blue line, and the regions associated with each force are highlighted in (b).

deformations in the glue can become significant, with a high degree of surface flattening occurring at the contact position. This alters the geometry of the system and results in the deviations from equation 3.1[147].

3.3.2 | Structural Forces

Here we discuss the interpretation for the structural forces, F_{osc} that arise in the observed force profiles. These detail the short range, oscillatory part of the force profile, and give rise to the first term in equation 3.1, which is reproduced here for clarity.

$$\frac{F_{osc}}{R} = A\, e^{-D/\lambda_o} \cos\left(\frac{2\pi}{\xi}(D+\delta)\right)$$

The values of the fitted parameters extracted from this region of the force profile are shown in table 3.3.

The magnitude of the structural force (A) is typically of the order

Table 3.3: Fitted parameters from the structural force in equation 3.1 for a range of concentrations of aqueous $LiNTf_2$ solutions

Concentration / mol kg^{-1}	A / mN m^{-1}	λ_o / nm	ξ / nm	δ / nm
4.70	480 ± 250	0.83 ± 0.15	1.53 ± 0.27	0.7 ± 0.5
8.11	25 ± 25	0.76 ± 0.51	1.63 ± 0.34	0.3 ± 0.5
11.64	132 ± 54	0.83 ± 0.09	1.32 ± 0.11	1.4 ± 0.5
12.22	36 ± 24	0.76 ± 0.30	1.17 ± 0.21	0.7 ± 0.5

of $\sim$ 100 mN m^{-1}. This corresponds to a free energy of interaction from the structural force of $\sim$ 16 mJ m^{-2}. A is highly dependent on the relative orientations of the two mica surfaces[148], which can lead to large variations in the magnitude of A between experiments where mica crystallographic alignment is not perfect. It will also depend on surface chemistry and charge, and can be sensitive to impurities and adsorbates[149]. As such, large variations of A between experiments is expected. The high error does not arise from insensitivity of the instrument, but instead from uncertainty in the exact location and adhesive force of each minimum position (from which A is calculated), as well as from contributions from additional forces that are not considered in this model, such as deviations from the ideal geometry as a result of surface flattening. Thus, long-range forces are not affected by these uncertainties. One consequence of the variation in A is a change in the surface separation of closest approach in the measurements shown in figure 3.3. In the 4.70 m case, A is very large. This means that the inner most layers are tightly held to the surface and may not be squeezed out from between the surfaces within the force range of our experiment, hence the surfaces cannot approach closer than $\sim$ 2 nm.

The parameter δ corresponds to an offset in the oscillatory force. As the mica surfaces are negatively charged when immersed in an elec-

trolyte, even at the closest contact there must exist some positively charged film between the surfaces to ensure charge neutrality. This means δ takes some small positive value to account for the breadth of this film. The film acts to reduce the interaction between mica surfaces in liquids versus the interaction in air, and our measured free energies of interaction are substantially less than those measured in the absence of any liquid[147]. δ also carries information about shifts in the optical path from the calibration, giving rise to the high error.

λ_o describes the characteristic decay length of the structural force, and remains fairly constant over the entire concentration range. This suggests that λ_o is solution independent and therefore likely a confinement or surface dependent property. It can be interpreted as the ability of the mica surfaces to template layers against themselves when confining a liquid, and describes the length scale over which correlations within the liquid film are perturbed by the presence of an interface.

Finally, ξ describes the wavelength of the oscillations, and arises from a correlation within the bulk liquid. The surface templates a liquid structure against itself. As the surfaces approach, layers of the structure are successively squeezed out, giving rise to the oscillatory force. In the case of simple molecular liquids, the structure is just layers of molecules, and as such the wavelength ξ corresponds to the molecular diameter[22,45,46]. However in the case of electrolytes, an additional constraint is added: the system of the thin film and the surfaces confining it must remain charge neutral. For this reason, in ionic liquids (pure liquid salts), ξ corresponds to the diameter of an ion pair, *i.e.* the oscillations arise from the squeeze out of a layer of cations and a layer of anions[66–68].

In the case of a concentrated aqueous electrolyte, it is unclear what

the wavelength of the oscillations should correspond to, however previous research has suggested that layering in concentrated solutions of simple salts arises from hydrated cation layers at the mica surfaces[60,150]. Neutron scattering measurements on concentrated aqueous lithium salts have suggested a hydrated lithium ion diameter of $\sim$ 0.5 nm, which is a large underestimate of the layering dimension observed here[143]. A mean unit diameter (one ion pair surrounded by water molecules in the correct molar ratio) could also be calculated by considering the solution density and unit molar mass. This crude calculation finds a mean ion diameter of 0.83 nm for a 5 m solution, and 0.72 nm for a 12 m solution, also a substantial underestimate of the observed wavelength.

A further possibility is that the observed wavelength arises from a self-assembled nano-structure within the liquid. Such self-assembly is well known for bulk ionic liquids containing long alkyl chains, where interactions between uncharged tail groups leads to a separation of the liquid into charge-rich and charge-poor regions[151,152]. In surface forces studies, these nano-structured domains manifest as bilayers[24,69]. A similar argument could be made for the observations described here. Lithium cations are small and charge dense. These properties make the cations extremely hydrophilic. On the other hand, the NTf_2^- anions are bulky, delocalised and charge diffuse, as well as highly fluorinated. This makes the anions relatively hydrophobic. We suggest that this diverging affinity of the ions for water association leads to a separation of the solution into a hydrated cation domain, rich in water molecules and lithium ions, and a non-aqueous anion domain, from which water molecules are largely excluded. The separation of charges into these domains is driven by the difference in solvation behaviour of the ions. Mica is negatively charged in the presence of aqueous solutions owing

to the dissolution of potassium ions from the surface. A region of the aqueous cation domain is therefore templated against the mica surface. This provides a template for a region of the non-aqueous anion domain, which again templates the cation domain, decaying away into the bulk with a wavelength of ξ and a decay length of λ_o. The jumps observed in the SFB experiments correspond to the removal of both a hydrated cation domain and a non-aqueous anion domain in order to maintain charge neutrality between the surfaces. This behaviour is sketched in figure 3.7. In this interpretation, the thin, positively charged film confined between the mica surfaces at closest surface contact will correspond to a single layer of hydrated cation domain, thus we expect δ will always be smaller than ξ, as we have observed.

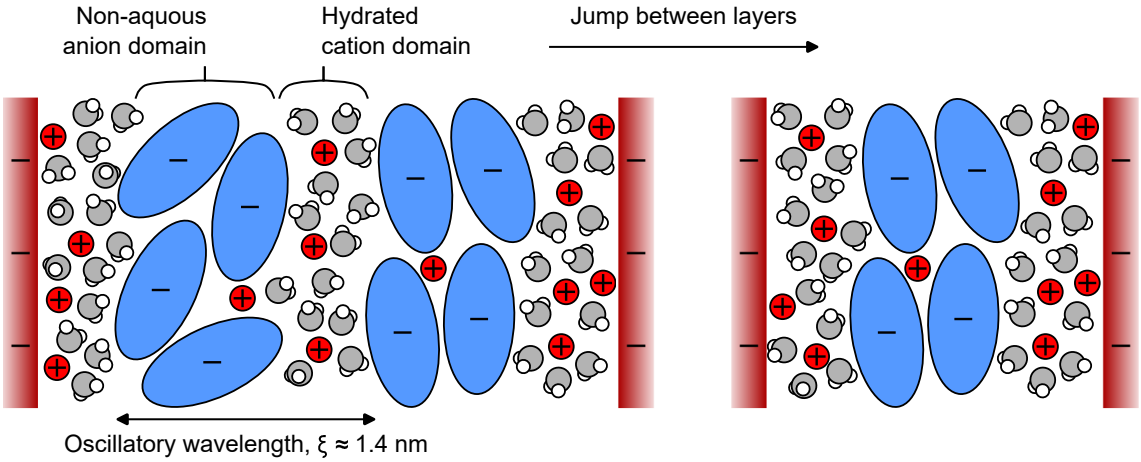


Figure 3.7: Cartoon representation of a possible domain structure present in the water-in-salt electrolyte $LiNTf_2$. The hydrated cation domain and non-aqueous anion domain are shown. Successive removal of layers of the domains, as templated by the negative mica surfaces, gives rise to the oscillatory force measured.

Further information about the behaviour and structure present in the confined WiS film can be drawn by considering the evolution of the layers under increased force. This is captured by the compressions that take place within layers, and by the jump distances between layers. These are calculated as shown in figure 3.3(b), and are shown as a

function of concentration for each layer in figure 3.8.

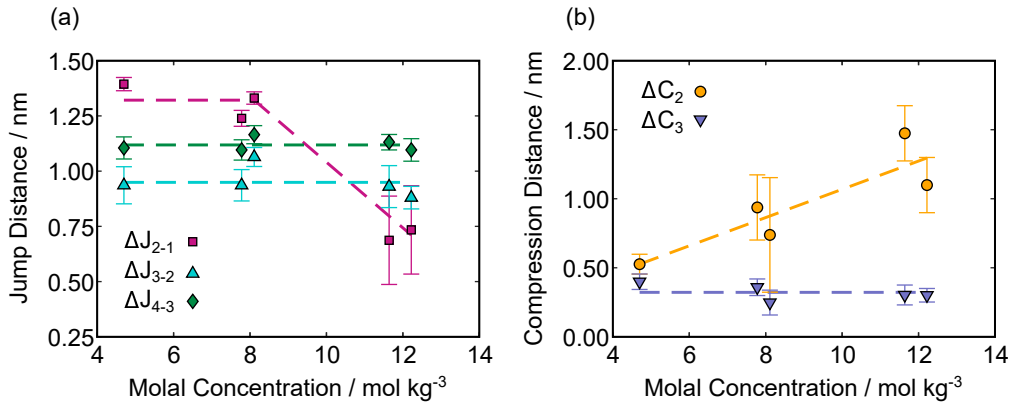


Figure 3.8: Data on jump distances (a) and compressions (b) between and within layers of WiS electrolyte. Lines are drawn as guides to the eye.

Jump distances between outer layers stay constant as the concentration of $LiNTf_2$ is increased, which suggests that a similar structure is removed from between the SFB surfaces in each case. This means that the size of the domain structure remains relatively constant as the concentration is increased, perhaps suggesting that any shrinking in the hydrated cation domain by the removal of water from the system is compensated for by a swelling of the non-aqueous anion domain as ion concentration increases. This trend changes for the inner most layering transition, with ΔJ_{2-1} (12 m) $<$ ΔJ_{2-1} (8 m, 5 m). This change suggests a rearrangement in layer $i = 2$ at the highest concentration; some reversible structural reorganisation can take place within the layer to reduce the layer thickness and allow a compression (hence the large compression distance ΔC_2 at the highest concentration). Such a reorganisation could take place via a dehydration in the hydrated cation domain, or by a reorganisation in the non-aqueous anion domain as long as charge neutrality is retained. Large compressions are not seen in the outer layers at any concentration, so such transitions must have a large energy barrier and require a high compressive force to induce.

3.3.3 | Long Range Forces

We now move on to discuss the long range forces, F_{lr} observed in the total force profile, as shown in figure 3.4. These describe the long range, monotonically decaying exponential part of the force profile, and give rise to the second term in equation 3.1, which is reproduced here for clarity.

$$\frac{F_{\text{lr}}}{R} = B\ e^{-D/\lambda_s}$$

The values of the fitted parameters extracted from this region of the force profile are shown in table 3.4. This force is small, and shows an increasing decay length with increasing concentration.

Table 3.4: Fitted parameters from the long range force in equation 3.1 for a range of concentrations of aqueous $LiNTf_2$ solutions

Concentration / mol kg^{-1}	B / mN m^{-1}	λ_s / nm
4.70	0	N/A
7.78	0.119 ± 0.049	8.5 ± 1.6
8.11	0.403 ± 0.123	6.2 ± 0.5
11.64	0.161 ± 0.063	11.8 ± 2.6

As noted above, the classical theory of electrolytes holds that forces arising from Debye-Hückel screening behaviour between ions are expected to become very short range at large concentrations[7], and indeed at concentrations in excess of 1 m are expected to fall to molecular dimensions. As such, the measurement of long range forces between negatively charged surfaces across a thin film of electrolyte is surprising. Nevertheless, such measurements have been made many times over the last decade, both with surface force[59,60,71,153–157] and independent[158,159] measurement techniques, and have been shown to be independent of viscous forces that arise between surfaces in motion[160]. This force has become known as “underscreening", as it ap-

pears that electrostatic forces are not screened as efficiently as expected in concentrated electrolytes. However, underscreening remains a controversial finding. A recent AFM study has found no evidence for this force in concentrated electrolytes[161], while simulations have also struggled to find evidence for an underscreening force that matches experimental observations[162–164].

Recently, an experimentally observed scaling law was introduced, describing how the observed decay length of the underscreening force depended on the electrolyte parameters[155]:

$$\frac{\lambda_s}{\lambda_D} \sim \left(\frac{a}{\lambda_D}\right)^3 \tag{3.2}$$

for all $a/\lambda_D > 1$. Here, λ_s is the measured screening length, λ_D is the classical Debye length, and a is the ion diameter (when $a/\lambda_D \ll 1$, normal Debye-Hückel screening is observed), and several recent calculations and models have shown that such a force can exist[165,166]. This empirical law suggests that screening length should increase with increasing concentration, as we have observed.

Our measurements perhaps shed light on why underscreening remains elusive in both measurements and calculations. By comparing the values of A (shown in table 3.3) and B (shown in table 3.4) from equation 3.1, we see that the long range force is three orders of magnitude smaller than the oscillatory force. This means that this force is only measurable where extremely small forces can be observed, such as in the SFB, and could explain the apparent lack of underscreening observations in simulations and other measurements using less sensitive techniques.

3.4 | Summary

In summary, we have performed direct measurements of surface forces present in the water-in-salt electrolyte $LiNTf_2$. We observed an exponentially decaying, oscillatory structural force, and an exponentially decaying, monotonic long range force, in a form similar to the force profiles seen in ionic liquids. We extract key data about the structure and behaviour of confined WiS films, and suggest a model of surface structure in which the liquid forms a nano-structure against the SFB surfaces. We also measure underscreening, in line with previous measurements on concentrated aqueous salts, and suggest why this long range force remains elusive to many techniques.

A key feature of our results is the model of surface structure. This is templated by charged surfaces, and will be present at electrode surfaces in electrochemical energy storage devices. Such ordering could be vital in the formation of the solid-electrolyte interphase that extends the electrochemical stability window and hence the energy density of WiS batteries, and optimisation of this feature of the electrolyte could lead to extensions to the electrochemical stability window. It will also have implications for the nature of ion transport to the electrode surface, and an interesting further direction for study could be to look at the transport of lithium ions across the non-aqueous domains.

Overall, our results highlight the complex nature of these highly concentrated electrolytes, and will be important in future research to design and commercialise WiS-electrolyte based energy storage devices.

4 | Bulk Structure of a Water-in-Salt Electrolyte

In chapter 3, we presented measurements of the structures and interactions present in the water-in-salt electrolyte lithium bis(trifluoromethanesulfonyl)imide, $LiNTf_2$, confined in thin films between two planar surfaces. The results indicated a structural correlation length of ≈ 1.5 nm over a broad range of concentrations. This was interpreted as a layered structure of alternating water- and cation-rich hydrophilic domains and anion-rich hydrophobic domains. In Principle, measurements of a correlation length in a confined film should reveal interactions equivalent to those present in the bulk liquid. Thus, we expect that the interactions giving rise to the ≈ 1.5 nm length scale to also influence the bulk structure. However, the precise nature of the structure was only hypothesised, and remains to be demonstrated directly. In this chapter we move on to investigate the bulk structure of these solutions in order to test our domain hypothesis and to provide a more complete picture of the structuring in complex water-in-salt electrolytes.

Previous bulk characterisation has been carried out, most notably by Borodin *et al.*[167], who showed through small angle neutron scattering (SANS) measurements on concentrated aqueous $LiNTf_2$ solutions that there is a correlation length of 1 to 2 nm present in the bulk liquid. This result was obtained in tandem with a variety of spectroscopic techniques and interpreted with molecular dynamics simulations. Their findings suggested that the bulk liquid was separated into a percolating anion network, throughout which exist clusters rich in water and lithium cations, similar to the hypothesis we described for the structure at sur-

faces in chapter 3. They also showed that ion conductivity in the 21 m saturated $LiNTf_2$ system was comparable to conductivity in state-of-the-art non-aqueous lithium ion battery electrolytes. Investigations into the ion solvation showed that ~ 40 % of the lithium ions had no NTf_2^- ions in their immediate coordination shell. They suggested that the ~ 40 % of lithium ions uncoordinated by the NTf_2^- ions were responsible for the high conductivity of the solution, with units of $Li(H_2O)_4^+$ acting as the dominant charge carriers in a vehicular mechanism of ion transport. In this mechanism, the ion moves together with its solvation shell over a distance of several solvated ion diameters before exchanging solvating molecules or ions.

Since these findings, further work has investigated structure and properties of various WiS electrolytes using scattering and simulation techniques. Studies have looked at nano-scale relaxation in aqueous $LiNTf_2$ and water-in-bisalt solutions[168], at liquid structure in WiS electrolytes with asymmetric anions[169], at hydrogen bonding, solvation and solubility[170,171], and at the nature of the ion and water networks that form in WiS electrolytes[172–176]. Together, the insights from these works start to build a picture of WiS electrolytes, with the nano-segregation of the fluid into domains driven by the disparity in water affinity between the cation and anion. As the salt concentration is increased, the extent of the anion-rich domains has been shown to grow, eventually percolating through the entire structure. The mechanism of lithium ion transport through the bulk WiS electrolyte remains of particular interest. Zhang and colleagues have suggested that at very high concentrations, the extent of the hydrated cation domains breaks down, with water existing in smaller clusters and filaments in which the vehicular mechanism cannot account for the high lithium ion conductivity[172,173].

Instead, they suggested lithium was transported via a “hopping” mechanism, in which the ion moves with its solvation shell over a distance of a single solvated ion diameter before exchanging solvating species.

Here, we present coherent elastic neutron scattering measurements on concentrated aqueous solutions of $LiNTf_2$, using multiple hydrogen contrasts. We analyse this data using an empirical potential structure refinement (EPSR) technique. These methods allow us to build a model of the WiS electrolyte that fits closely to the measurements, and which can be used to find molecular scale structural information.

4.1 | Experimental Details

We performed scattering measurements at two concentrations of aqueous $LiNTf_2$. Our experiments were performed with the NIMROD instrument on the ISIS neutron spallation source in Harwell, UK, as described in chapter 2. Data was collected with the advice and technical support of the instrument scientist Dr Tom Headen, and in collaboration with Dr James Hallett and Kieran Agg. Here, details specific to these experiments are discussed, alongside a description of the empirical potential structure refinement (EPSR) based analysis technique.

4.1.1 | Materials and Solution Preparation

Solutions of aqueous $LiNTf_2$ were prepared from freshly opened bottles of $LiNTf_2$ (Fluorochem, 99 %) in ultrapure water (18.2 MΩ cm), D_2O (Sigma Aldrich, 99.9 atom % D), a 1:1 mixture of ultrapure water and D_2O, known as HDO, or a 1.78:1 mixture of ultrapure water and D_2O for which the mean coherent scattering length of hydrogen atoms is zero, known as null water.

Measurements were made at two concentrations: 11.9 m and 19.7 m,

where m refers to the molal concentration, the moles of salt per kilogram of water, mol kg^{-1}. These concentrations cover the high concentration range of the WiS system, and enable comparison between the highest concentrations studied in our SFB measurements (≈ 12 m) with those at saturation of $LiNTf_2$ in water (≈ 21 m).

4.1.2 | Empirical Potential Structure Refinement and the Dissolve Package

Computational structure refinement, in which a model liquid structure is refined until it matches experimental data, is a powerful technique for predicting the structural arrangements within a liquid. It has its origins in the 1960s, where a Monte Carlo simulation on an array of 100 atoms only accepted changes that improved the fit of predicted x-ray diffraction patterns to those measured in a selenium glass[177]. Such reverse Monte Carlo methods are still used today, however these methods do not require any knowledge of the interaction potentials within the system.

In empirical potential structure refinement, EPSR, a three dimensional simulation box is built that matches the experimental components, concentration, and density. The system can be described using a simple reference potential, and is allowed to come to equilibrium as defined by the reference potential. Theoretical scattering data can then be generated from the simulation box, and is compared to a measured scattering pattern. Based on the difference between the calculated and measured scattering patterns, an additional empirical potential is introduced in order to push the model towards a match with the experiment[178]. This empirical potential is not derived from any physical principles, and takes the form of a series of functions that are iteratively

refined until an acceptable level of fit between the experiment and the simulated scattering pattern is reached. Multiple isotopic contrasts or scattering techniques can be used to improve the results, as the simulation must refine towards a single result which most closely matches all available data.

The EPSR software package, designed by Alan Soper[178], puts the described EPSR technique into effect, and has been widely used across a variety of disordered systems, including glasses, molecular liquids, ionic liquids, liquid mixtures, and micelles[179–184]. However, the latest EPSR software package, EPSR26 has several drawbacks including the size of possible boxes and the calculation speed, and as such we use the next generation empirical potential structure refinement package called Dissolve, which can support larger boxes and run faster calculations using parallel processing, and is more user-friendly. Dissolve also uses the EPSR technique to simulate a model 3D box based on experimental neutron scattering data, and has been shown to produce results consistent with EPSR26 for a variety of systems[39].

In the version of the Dissolve software package we used (Dissolve v1.4.0), bonds within molecules are treated as harmonic oscillators, with force constants, bond lengths and angles taken from the literature. The interatomic reference potentials consists of a Lennard-Jones term, which accounts for van der Waals and steric interactions between atoms, and a Coulombic term where each atom is assigned a partial charge to account for electrostatic interactions. The system is then equilibrated through a combination of Monte Carlo and Molecular Dynamics steps. Structure refinement then takes place iteratively using the EPSR technique as described above, until an acceptable global level of fit is achieved across each isotopic contrast, at which point it is as-

sumed the simulated liquid structure matches closely the experimental liquid structure. In our systems, we consider three species: the Li^+ cation, which has only interatomic interactions and carries a full +ve charge[185]; the NTf_2^- ion, for which we use ionic liquid structure and interactions designed by Neumann *et al.*[186]; and the H_2O molecule, for which we use the flexible simple point-charge water model[187]. We note that these force fields do not give perfect representations of their species, but that they provide a basis set from which our model box may be generated in a realistic configuration. The force fields are then refined during the EPSR process to fit to the data collected in multiple contrasts.

4.1.3 | Densities

Accurate knowledge of the densities of the solutions of interest is of absolute importance when setting up the model box for EPSR. To ensure this, the densities of a broad concentration range of $LiNTf_2$ solutions was measured as described in chapter 2, carried out together with Kieran Agg, in order to produce an empirical reference curve for aqueous WiS solutions. This is shown in figure 4.1.

The measured density data could be fitted to a curve of the form

$$\rho = Ae^{ac} + Be^{bc} \tag{4.1}$$

where ρ is the density, c the molal concentration, and A, B, a and b are fitted parameters. We found a best fit with $A = 1.63$ g cm^{-3}, $B = -0.55$ g cm^{-3}, $a = 0.00306$ kg mol^{-1} and $b = -0.164$ kg mol^{-1}.

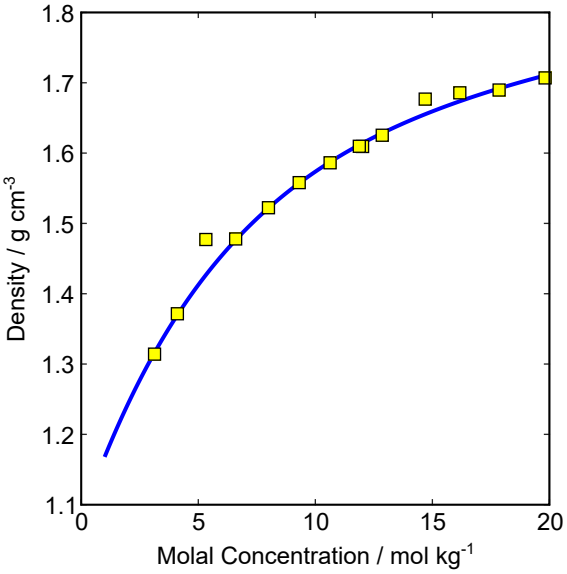


Figure 4.1: Densities of aqueous $LiNTf_2$ solutions across the whole concentration range of $LiNTf_2$ solubility. The blue line shows a fit to equation 4.1.

4.1.4 | Dissolve Model Details

We set up two models using the Dissolve software package to perform EPSR and fit our measured data with concentrations chosen to match the experimental concentrations. In the first model box, there were 6136 water molecules, 1317 lithium cations, and 1317 NTf_2 anions. This corresponds to a concentration of 11.9 m, with a density of 1.61 g cm^{-3}, giving a box with side length 7.95 nm. In the second model box, there were 5500 water molecules, 1953 lithium cations, and 1953 NTf_2 anions. This corresponds to a concentration of 19.7 m, with a density of 1.71 g cm^{-3}, giving a box with side length 8.62 nm.

4.2 | Bulk Structure Measurements and Discussion

Scattering measurements were made at two separate concentrations, 11.9 m and 19.7 m, with four isotopic solvent contrasts at each concentration. The raw scattering diffraction patterns for each contrast at each concentration are shown by the solid lines in figure 4.2. In each case

we see a series of peaks that arise because of correlations within the liquid. Q is related to real space distance d as $d = 2\pi/Q$ as described in equation 2.13, so peaks at higher-Q correspond to shorter ranged distance correlations while those at lower-Q correspond to longer ranged correlations. Scattering is expected to fall to 0 at very high-Q as these regions of the scattering pattern correspond to distances much smaller than molecular bond lengths.

An initial examination of the raw scattering patterns reveals an interesting feature: at both concentrations a low-Q peak can be observed between 0.5 and 0.6 $Å^{-1}$. This low-Q peak is particularly prominent in the data recorded for $LiNTF_2$ solutions in H_2O and D_2O at each concentration, and is visible as a shoulder in the data in null water. It is also much more prominent in data measured at 11.9 m than at 19.7 m. The peak is highlighted in figure 4.3. Converting to real-space distance units using equation 2.13, this peak corresponds to a correlation length of between 1.05 and 1.26 nm. This length scale is larger than the van der Waals radii of the single ions and molecules present in the solution (shown in figure 3.2), and thus the existence of this large correlation length implies some form of structuring present within aqueous solutions of $LiNTf_2$ beyond the scale of nearest neighbours. This observation is similar to that seen in the surface force experiments described in chapter 3, where an oscillatory structure with wavelength of ~ 1.2 nm was observed in 12 m solutions of $LiNTf_2$, and is analogous to the long range correlations previously measured in these systems[167].

Additional peaks within the raw scattering data occur at $Q \gtrsim 1$ $Å^{-1}$. This corresponds to a real space distance of $\lesssim 0.63$ nm, which is similar to the dimensions of the species present. Peaks in this region of the diffraction pattern correspond to nearest neighbour or intramolecular

correlations, and contain information about the environment close to each atom in the solution.

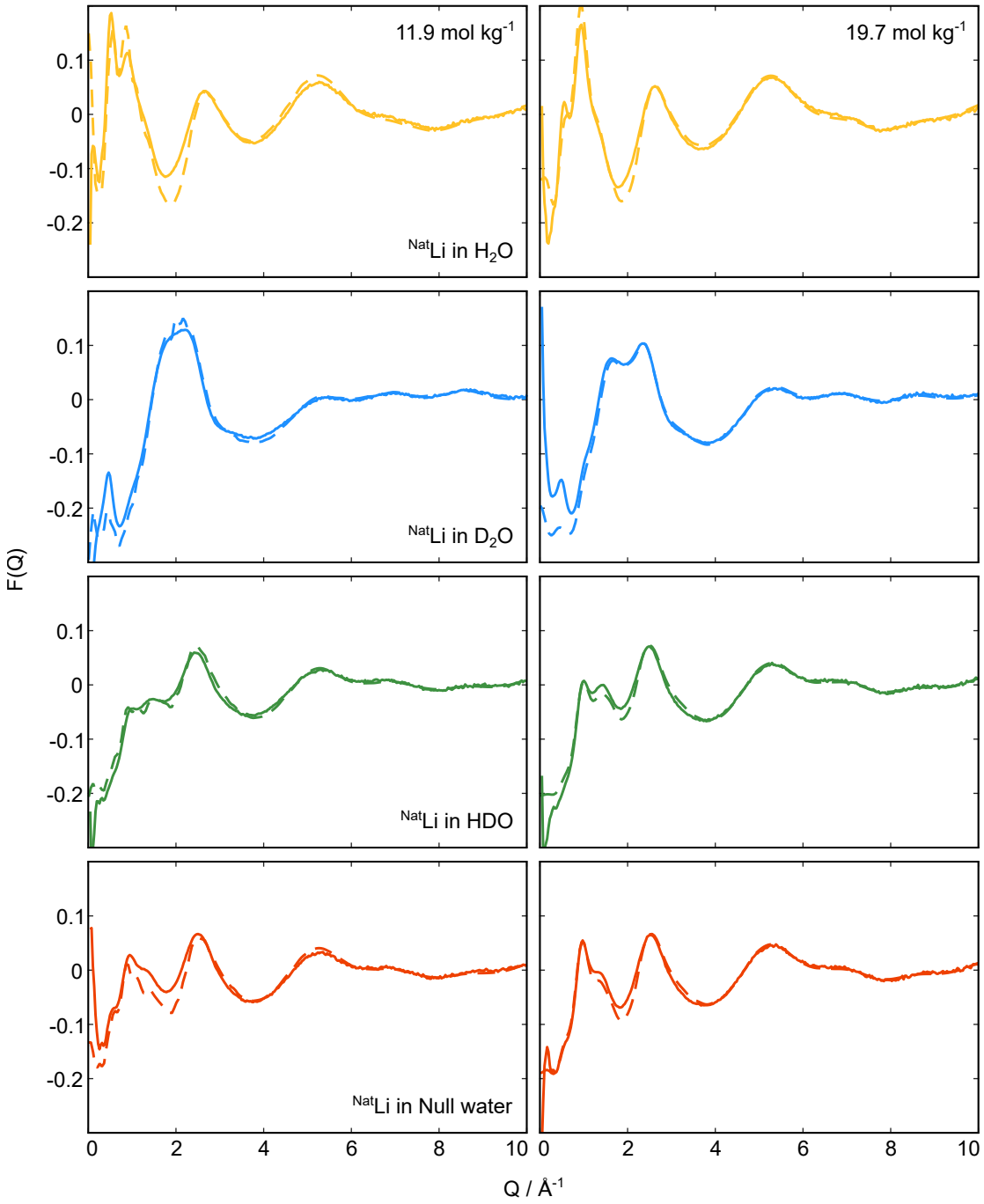


Figure 4.2: Experimental (solid lines) and fitted (dashed lines) neutron diffraction patterns for each concentration and each solvent contrast. $LiNTf_2$ in H_2O is shown at the top in yellow, $LiNTf_2$ in D_2O is shown second in blue, $LiNTf_2$ in HDO is shown third in green, and $LiNTf_2$ in null water is shown at the bottom in red. Measurements and model data for the 11.9 m is shown on the left, with the 19.7 m case shown on the right.

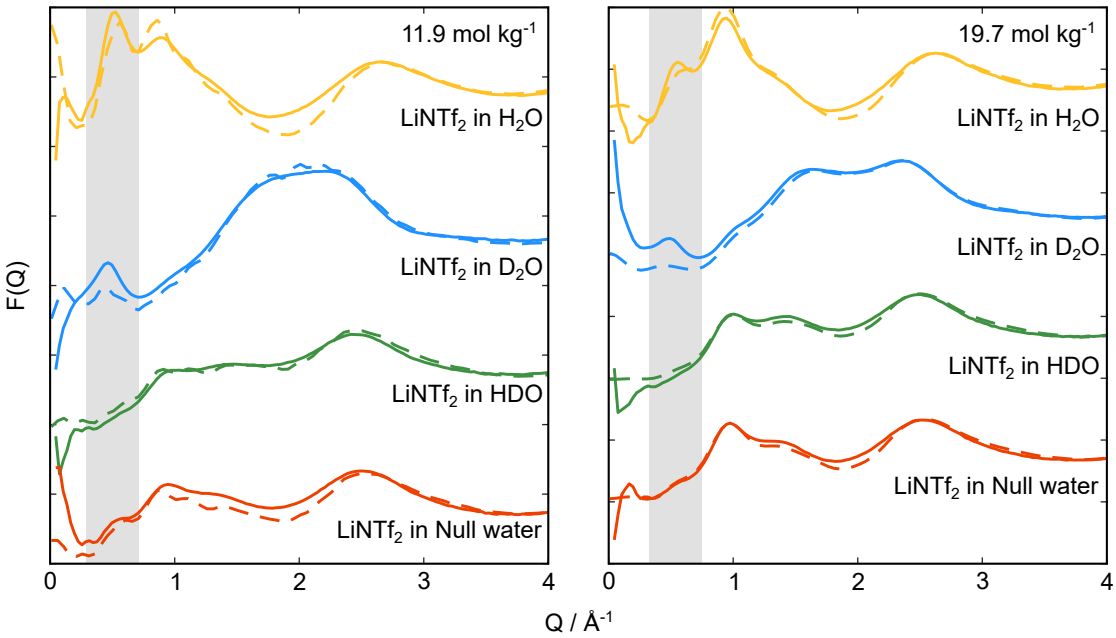


Figure 4.3: Experimental (solid lines) and fitted (dashed lines) neutron diffraction patterns for each concentration and each solvent contrast, zoomed in to highlight features at low Q. $LiNTf_2$ in H_2O is shown at the top in yellow, $LiNTf_2$ in D_2O is shown second in blue, $LiNTf_2$ in HDO is shown third in green, and $LiNTf_2$ in null water is shown at the bottom in red. Measurements and model data for the 11.9 m is shown on the left, with the 19.7 m case shown on the right.

We use the Dissolve package to produce a model of the liquid structure using EPSR. The simulated scattering pattern is shown for each contrast at each concentration as the dashed lines in figures 4.2 and 4.3. In each case, the fitted data is in good agreement with the experimental data, with some differences at the low-Q limit where errors in the inelasticity correction and instrument resolution can lead to discrepancies. Errors in the inelasticity correction likely arise due to unaccounted-for hydrogen atoms in the measurement samples, which have large inelastic scattering cross sections. The mismatch is largest in the D_2O solvent contrast, which suggests some level of H_2O contamination, either from the air during solution preparation and transport, or in the deuterated water used to make up samples. However, the fitted scattering patterns are obtained from a best fit across all contrasts, and

these small discrepancies in some of the contrasts should not significantly affect our interpretation. This is shown by the consistent qualitative, if not quantitative, agreement across the entire Q-range.

The agreement between the measured and fitted scattering patterns suggests that the liquid structure in the simulation boxes is indeed close to the structure adopted by the liquid in bulk environments. Thus, analysis of the simulated box may be used to understand the structures and interactions present within the liquid. Snapshots of the simulated boxes are shown in figure 4.4 at both 11.9 m and 19.7 m. The lithium cations are shown in red, water molecules in grey (oxygen) and white (hydrogen), and the NTf_2^- anions are shown as a blue surface mesh. These snapshots at each concentration show that there is an extensive network of anions present in the system with water rich regions throughout this anion network. The extent of the water rich regions appears to decrease as the salt concentration is increased from 11.9 to 19.7 m, as suggested by the decrease in the intensity of the prepeak in the raw data. Such a decrease is perhaps intuitive: as the amount of salt is increased relative to the amount of water in the system, then the water rich regions within the liquid will necessarily shrink.

4.2.1 | Interactions in the bulk liquid

The observed nano-structure arises due to the particular set of interactions present within the liquid. These interactions can be quantified by examining the radial distribution functions (RDFs) and coordination numbers of the individual species. Such structural information is virtually impossible to extract from raw experimental neutron scattering data, but can be found from the simulated liquid boxes shown in figure 4.4. The radial distribution functions of the lithium cation with water

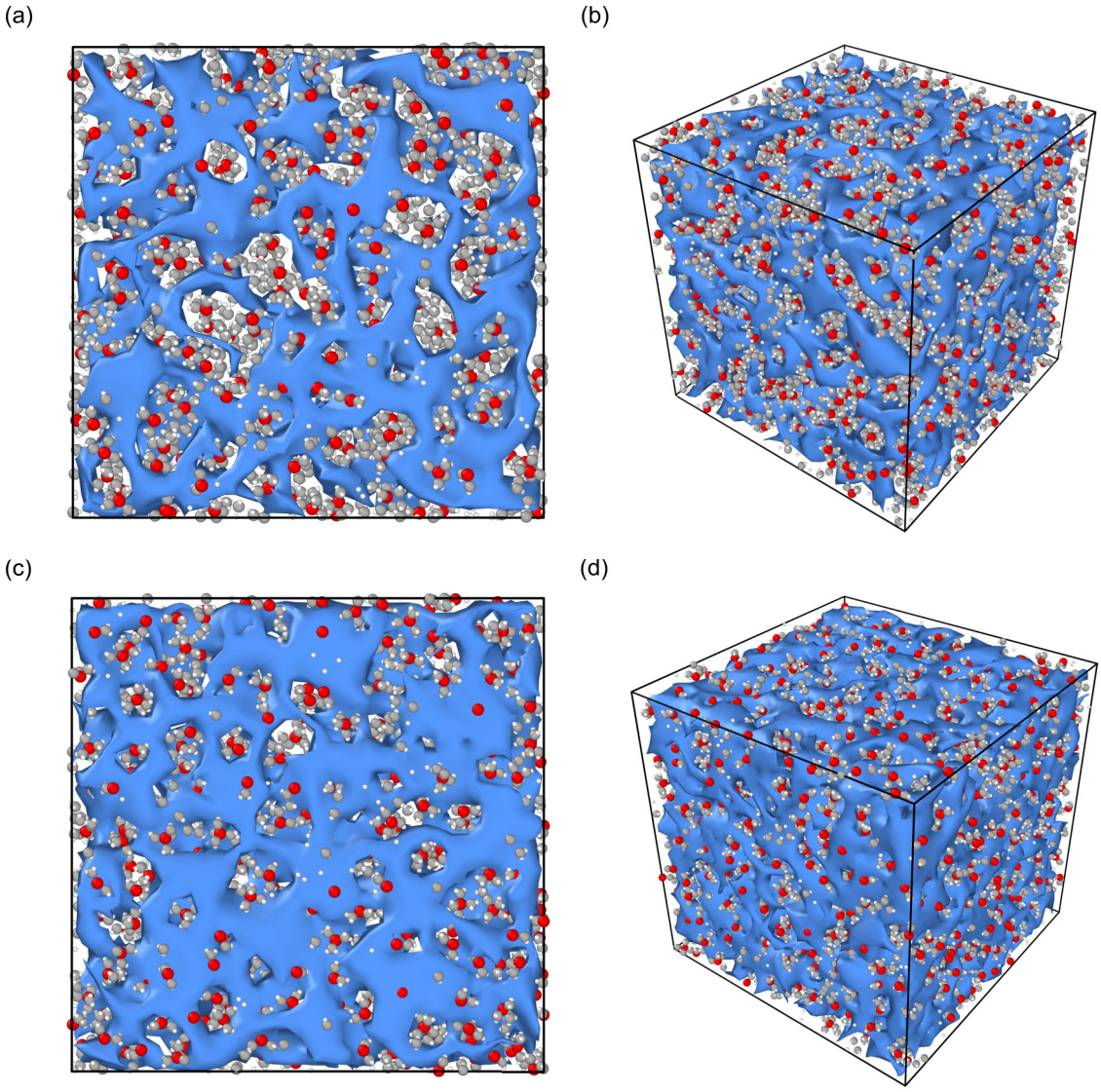


Figure 4.4: Snapshots of the dissolve model at 11.9 m ((a) and (b)) and 19.7 m ((c) and (d)). Water oxygens are shown in grey, water hydrogens in white, lithium cations in red, and NTf_2 anions as a blue mesh. Panels (a) and (c) show 1.5 nm thick slabs of the simulated box while panels (b) and (d) show a projection of the entire box.

and with the NTf_2 anion are shown in figure 4.5.

In the case of the lithium interaction with water, there is a very strong short range correlation between the lithium and water oxygen atom, with an initial peak at 0.21 nm at each concentration. There is also a second, much weaker peak at 0.44 nm. The lithium-water hydrogen RDF shows similar features to the lithium-water oxygen RDF, though these are shifted to slightly greater distances, with the initial

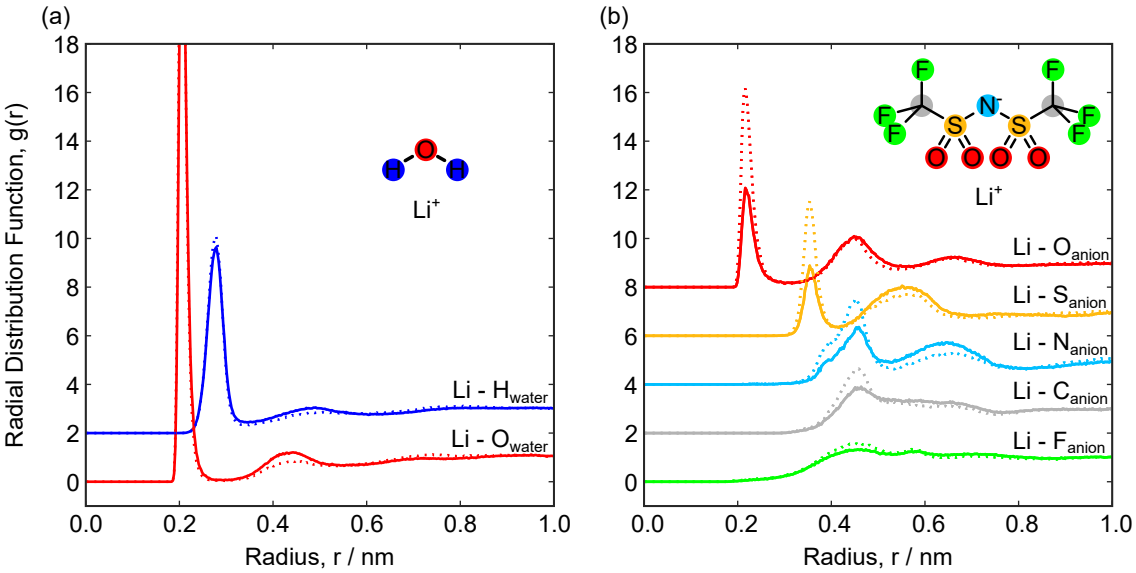


Figure 4.5: Intermolecular radial distribution functions of the lithium cation with each atom present in (a) water and (b) the NTf_2 anion. RDFs are accumulated over several hundred frames from the equilibrium models simulated in Dissolve. RDFs for the 11.9 m concentration are shown as solid lines and those for the 19.7 m concentration are shown as dotted lines. The colour of each line refers to the interaction between lithium and a specific atom type in either water or NTf_2, as described by the molecular diagrams. The RDFs are vertically offset by 2 in both panels to enable clear viewing.

peak at 0.28 nm and the second peak at 0.49 nm. This shift arises as the water molecules are mostly oriented with their oxygen atoms close to the lithium ions, as expected based on the ion-dipole interaction: the high electronegativity of oxygen means it carries a large partial negative charge. This leads to a strong electrostatic attraction between the lithium cation and the water oxygen, so such nearest neighbour pairings are common in our simulation box and we see a strong peak in the RDF. The presence of a second lithium-oxygen peak suggests that this order templating effect extends to two hydration shells.

For the lithium interactions with the anion, there is a strong correlation between the lithium and the anion oxygen atoms. Here we see three clear peaks: an initial peak at 0.22 nm, a second peak at 0.45 nm, and a third peak at 0.66 nm. These features are again carried through the molecule, with lithium-sulfur peaks at 0.35 nm and 0.56 nm, and

lithium-nitrogen peaks at 0.46 nm and 0.65 nm. There are also very small lithium-carbon and lithium-fluorine peaks at 0.46 nm.

Again, these features point to lithium solvation by the oxygen atoms of the anion. As in water, these oxygen atoms carry partial negative charges and are free to interact electrostatically with the lithium cation. The nitrogen atom also carries a partial negative charge, however we do not see evidence for a lithium-nitrogen nearest neighbour interaction. This is likely because the nitrogen atom of the anion is sterically hindered by the rest of the anion, preventing a direct interaction with the lithium. Instead, the peaks seen in the sulfur, carbon and nitrogen RDFs arise as a consequence of the strong lithium-oxygen interaction.

It is surprising that there is significant overlap between the radial distribution functions despite the substantial difference in molar ratio between the 11.9 m and 19.7 m systems, particularly in the case of the lithium-water interaction (figure 4.7 (a)). However, the RDFs are normalised by the mean density in the system. As this mean density of a species changes as the salt concentration is increased, it is not meaningful to directly compare the height of the peaks in the radial distribution functions between concentrations. Instead, we compare coordination numbers, N, which can be calculated as the cylindrical integral of a peak in the radial distribution function multiplied by the bulk density, as shown in equation 4.2.

$$N = \rho \int_0^r 4\pi r^2 g(r)\, dr \tag{4.2}$$

The calculated coordination numbers for the total lithium-oxygen interaction, and with the water and the anion oxygens individually, are shown in table 4.1.

The number of water molecules solvating each lithium ion decreases

Table 4.1: Coordination numbers of the primary hydration shell of lithium ions at 11.9 m and 19.7 m $LiNTf_2$ aqueous solutions, calculated as in equation 4.2. A cut-off value of 0.31 nm was used in each case, taken as the minima from the Li-O RDFs shown in figure 4.5.

Environment	11.9 mol kg^{-1}	19.7 mol kg^{-1}
Li-O_{total}	4.6	4.5
Li-O_{water}	3.6	2.6
Li-$O_{NTf_2^-}$	1.0	1.9

as the salt concentration is increased, as there are fewer water molecules per lithium ion. However, the total lithium-oxygen coordination number is independent of mole fraction, as the desolvation by water molecules is compensated for by an increase in lithium-anion solvation as the concentration is increased. This suggests that extensive lithium-water domains are not as likely at very high salt concentrations, as they get broken up by lithium-anion interactions.

We also consider correlations between the anion with water and with other anions in order to understand the liquid structure about the anions. The intermolecular radial distribution functions that quantify these correlations are shown in figure 4.6. We show the RDFs of each atom in the negatively charged anion with the partially positively charged water hydrogen, as this will be the principal interaction. We also show the RDFs of each anion atom with themselves. These show which regions of the anion are spatially correlated, allowing a picture of the anion solvation environment to be constructed.

We first examine the correlations between water and the anion. The primary association is between the anion oxygen atoms and the water hydrogen, with a peak at 0.19 nm, suggesting a hydrogen bonding interaction[180]. This strong H-O association can also be seen in the S-H and N-H RDFs, with peaks at 0.32 and 0.43 nm respectively that arise

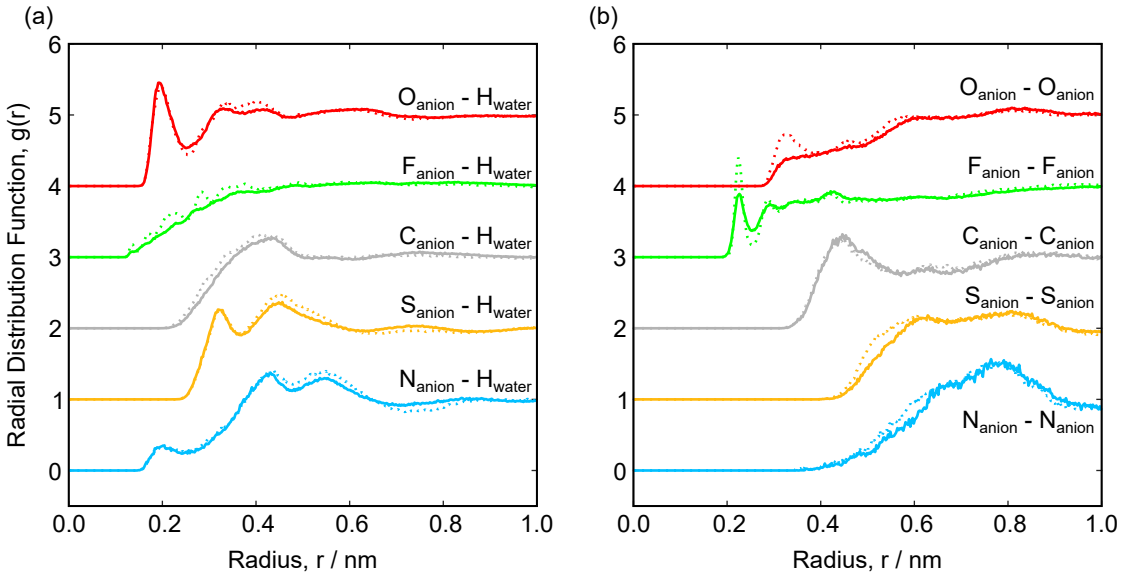


Figure 4.6: Intermolecular radial distribution functions of the NTf_2^- anion with (a) the water hydrogen atom and (b) the NTf_2^- anion. RDFs are accumulated over several hundred frames from the equilibrium models simulated in Dissolve. RDFs for the 11.9 m concentration are shown as solid lines and those for the 19.7 m concentration are shown as dotted lines.

as a consequence of hydrogen bonding at the anion oxygens. There is a small peak in the N-H RDF at 0.20 nm, suggesting that this is a possible hydrogen bonding site, however the density of hydrogen atoms at this site is smaller than the bulk density, so this association is not statistically significant in the solvation of the anion. This is likely due to the structure of the molecular anion, with bulky groups on either side of the nitrogen hindering this site for hydrogen bonds.

There is very little change in the RDFs as the concentration is increased. A coordination number calculation, as described in equation 4.2, shows that at 11.9 m, $N = 0.48$ for the O_{anion}-H, while at 19.7 m, $N = 0.54$. This analysis shows that as the concentration of salt is increased, the solvation environment of the water by the anion does not change significantly, and provides further evidence for the existence of a separation of the liquid into anion rich domains and water rich domains. As the concentration of salt is increased, the additional anions are dissolved into the anion rich domains. The anion-water as-

sociation only takes place at the boundary between these domains, and the boundary environment is largely unchanged by the increasing concentration.

The RDFs between like anion atoms show that there is relatively little well defined structuring between the anions. The exception to this is between the fluorine atoms, which show a single well defined peak at 0.23 nm. Such an association is again not unexpected: heavily fluorinated alkyl groups are hydrophobic and will associate with one another rather than with water. This means that the CF_3 groups of the anion are pointing away from the water-rich domains in the bulk WiS electrolyte. This interaction appears to grow in strength as the concentration is increased. Similarly, as the concentration is increased a peak emerges in the O-O RDF at 0.32 nm. The emergence of this peak could be coupled to the increase of lithium solvation by the anion as the concentration is increased. It suggests that as the amount of salt present in the solution is increased, it becomes more likely for lithium ions to be bound to multiple anions, allowing for anion oxygen ordering to occur across solvated lithium ions.

Finally, we discuss the interactions present between water molecules in the WiS electrolytes. The intermolecular radial distribution functions calculated from the Dissolve model that quantify these interactions are shown in figure 4.7, alongside literature RDFs for pure water[180].

The initial peak in the O-H RDF is positioned at 0.18 nm in pure water, and each concentration of WiS electrolyte investigated. This suggests that the nearest neighbour hydrogen bonding geometry in the WiS systems is unchanged from pure water. However, this peak sees a sharp decrease as salt concentration is increased from 11.9 m to 19.7 m, which suggests extended water hydrogen bond networks

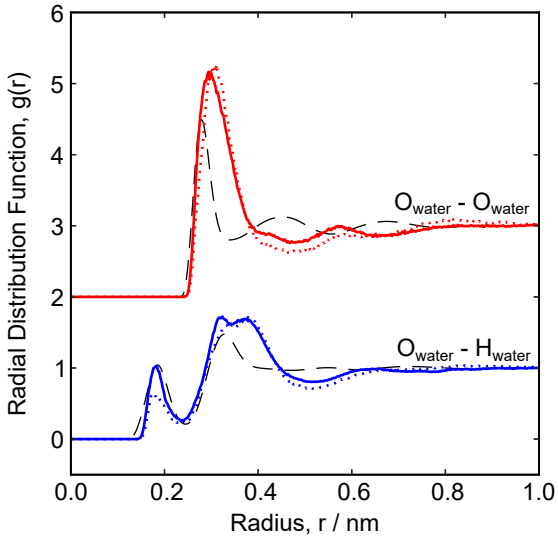


Figure 4.7: Intermolecular radial distribution functions between atoms present in H_2O. Correlations that arise from atoms within the same molecule are not included. RDFs are accumulated over several hundred frames from the equilibrium models simulated in Dissolve. RDFs for the 11.9 m concentration are shown as solid lines and those for the 19.7 m concentration are shown as dotted lines. The O-H RDF is shown in blue, and the O-O RDF is shown in red. Literature data for pure water is also shown as the black dashed lines, reproduced from a work by Soper *et al*[180].

become less likely as the salt concentration is increased. This is in agreement with data described above, and suggests that the increased salt concentration breaks up the water-rich domains.

The initial peak in the O-O RDF is at 0.28 nm in pure water, but moves outward as the salt concentration is increased, appearing at 0.30 nm in 11.9 m and at 0.31 nm in 19.7 m WiS electrolyte. The peaks also broaden as the salt concentration is increased. These observations suggest an increased uncertainty in the position of nearest neighbour water molecules as the concentration is increased, and again highlight the disruption of increasing salt concentration on the water-rich domains.

4.2.2 | Cluster Analysis

The raw neutron scattering data, plotted in figure 4.2, shows a clear low-Q peak at between 0.5 and 0.6 $Å^{-1}$. This feature unambiguously suggests the occurrence of a nano-structuring within the bulk liquid at both concentrations investigated. Analysis of the simulated radial distribution functions shows which interactions and length scales are important in this nano-structuring. We now use this information to characterise the extent of the nano-structuring domains.

We carry out a cluster analysis on multiple instantaneous snapshots of the Dissolve model simulation box to quantify the extent to which species appear close to one another. A Python programme, designed and written by Shurui Miao, was used to perform the analysis[188]. The method works by identifying an atom of a specific type (e.g. a water oxygen atom) and looking for a second defined atom in a different molecule (e.g. a water hydrogen atom in a second water molecule) within a cut-off radius. The cut-off is defined as the minimum in an association peak from the radial distribution functions. If the cluster analysis code finds the second atom type within the defined radius, then those two molecules are labelled as belonging to the same cluster. The code can examine multiple interaction sites and types per molecule, allowing the full extent of clusters in the simulation box to be found. The probability of finding a molecule of a specific type within a cluster of size n, $P(n)$ is given by

$$P(n) = nT/n_{\text{tot}} \tag{4.3}$$

where T is the number of times a cluster of n molecules is found, and n_{tot} is the total number of molecules examined by the analysis.

We examine a trajectory of 100 frames for each concentration using

this cluster analysis in order to produce reliable statistics. From the radial distribution functions described above, we identify five key interactions to examine. These are shown in table 4.2. To ensure any clusters identified are statistically significant and are not as a result of random chance, we compare our analysis to a percolation threshold. In any condensed system there is some critical probability above which the formation of large clusters is favoured and below which they are disfavoured. In a three dimensional system of non-interacting spheres, grown on any lattice using a closest contact approach to define the cluster, the critical probability always yields a universal Fisher exponent of $\tau \approx 2.2$. This Fisher exponent characterises the cluster size distribution and is empirically determined from computer simulations[189,190]. While the critical probability of including nearest neighbour non-interacting spheres varies with lattice geometry, the Fisher exponent does not. Thus, it is appropriate to compare the probability of finding a cluster of n molecules in our system, where we do not expect an ordered lattice, to this universal Fisher exponent. The probability of finding a molecule in a cluster of n molecules $P(n) \propto n \cdot n^{-\tau} \propto n^{-1.2}$. If the probability of finding a cluster in our system sits above this line, then these clusters can be said to form as a result of the interactions present in our system and not through random chance.

The results from this cluster analysis focusing on water molecules are shown in figure 4.8. Examining first the case of water-only clusters (figure 4.8 (a) and (b)), we see that at 11.9 m there is a slight preference for clusters of water molecules on the order of 20-30 molecules, but that larger clusters are disfavoured. At the higher concentration, only clusters with $n \leq 10$ are found to be likely. This observation shows that water only rich domains do not exist at any great extent in WiS

Table 4.2: Clusters investigated by this cluster analysis. The associations probed, along with the cut-off radii, are shown.

Cluster	Associations probed	Cut-off radius / nm
water-water	O_{water}-H_{water}	0.25
water-lithium-water	O_{water}-Li O_{water}-H_{water}	0.25
anion-lithium	O_{anion}-Li	0.3
anion-anion	F_{anion}-F_{anion}	0.26
anion-lithium-anion	O_{anion}-Li F_{anion}-F_{anion}	0.3

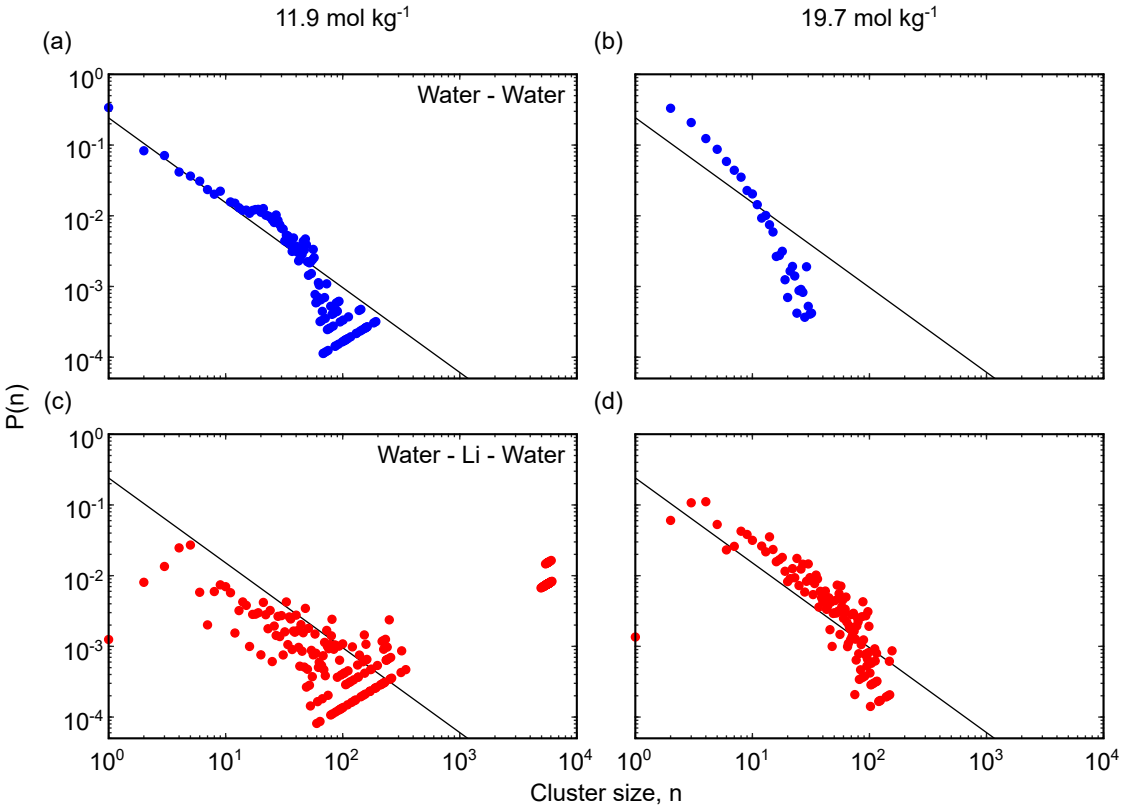


Figure 4.8: Cluster analysis of 100 snapshots of the simulation boxes in aqueous $LiNTf_2$ focusing on interactions between water molecules. The plots show the probability of finding a molecule within a cluster containing n molecules against the size of the cluster, n. The solid black lines on the plots show the percolation threshold normalised to the box size. (a) and (b) show water-water clusters, and (c) and (d) show water-lithium-water clusters. (a) and (c) show analysis of the 11.9 m system, and (b) and (d) show analysis of the 19.7 m system.

electrolytes.

A consequence of this is that, in a high salt concentration water-in-salt electrolyte, it is extremely rare to find a water molecule in an environment similar to that experienced by water in dilute electrolytes. The vast majority of water molecules are interacting in some way with an ion. These interactions are present throughout the solution, and dramatically affect the electronic structure of the water molecule. Such effects can lower the energy of the highest occupied molecular orbital of the molecule, which will increase the oxidation potential, and hence this solvation of the water molecules by the salt increase the electrochemical stability window of the WiS system, as discussed in chapter 3.

Extended aqueous networks may be possible if the water molecules are able to use lithium ions to bridge the gap between water clusters. In figure 4.8 (c) and (d) we consider this scenario by searching for clusters in which water is interacting closely with either another water molecule (as in (a) and (b)) or with a lithium ion. The result is that networks become far more extensive, suggesting percolating water- and cation-rich domains, as we first suggested from our surface force studies in chapter 3. These ideas are highlighted schematically in figure 4.9.

The extension of the water clusters by considering water-lithium ion interactions is particularly significant at 11.9 m, where the hydrated cation domains can extend throughout the entire simulation box. Such extended behaviour is not observed at 19.7 m, however there is a significant expansion of clusters from those found by considering only water-water interactions, with clusters now found to contain $\sim$ 100 molecules and ions. This means that at the highest possible concentrations of water-in-salt electrolytes, the hydrated cation domains are not able to percolate through the entire structure and can be isolated by the anion-

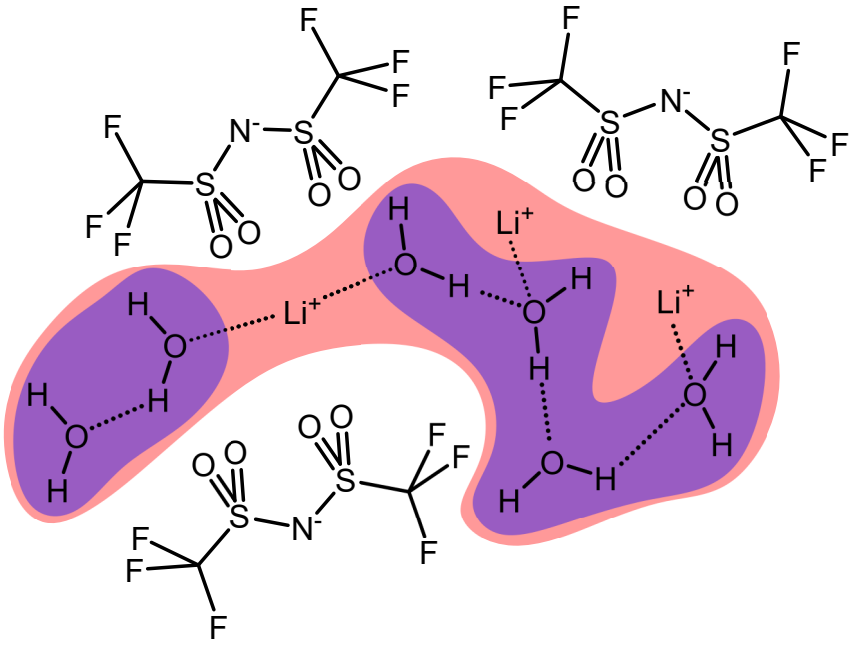


Figure 4.9: Water molecule centred cluster analysis. When only water-water interactions are considered (figure 4.8 (a) and (b)), small clusters in which all water molecules are directly linked are found. When water-lithium interactions are considered as well (figure 4.8 (c) and (d)), larger clusters can be found as lithium ions can act as bridges between small water-only clusters. Only interactions considered in the relevant cluster analyses are shown.

rich hydrophobic domains. Such an observation has consequences for the interpretation of rapid lithium ion transport throughout WiS systems: it suggests that transport along extended lithium-water networks by a vehicular mechanism cannot be the sole driver of lithium ion transport and instead supports a lithium “hopping” mechanism as has recently been hypothesised[173].

This hopping mechanism will be important in lithium transport to electrode surfaces. As we observed in our surface force measurements on WiS solutions, the domain structure is templated into layers by the presence of a surface. In order to reach an electrode surface, lithium ions must be able to cross this domain structure. A hopping mechanism, in which lithium ions can diffuse through domains by hopping from water to NTf_2^- solvation provides a pathway for this to occur.

We now consider the results of the cluster analysis focusing on the

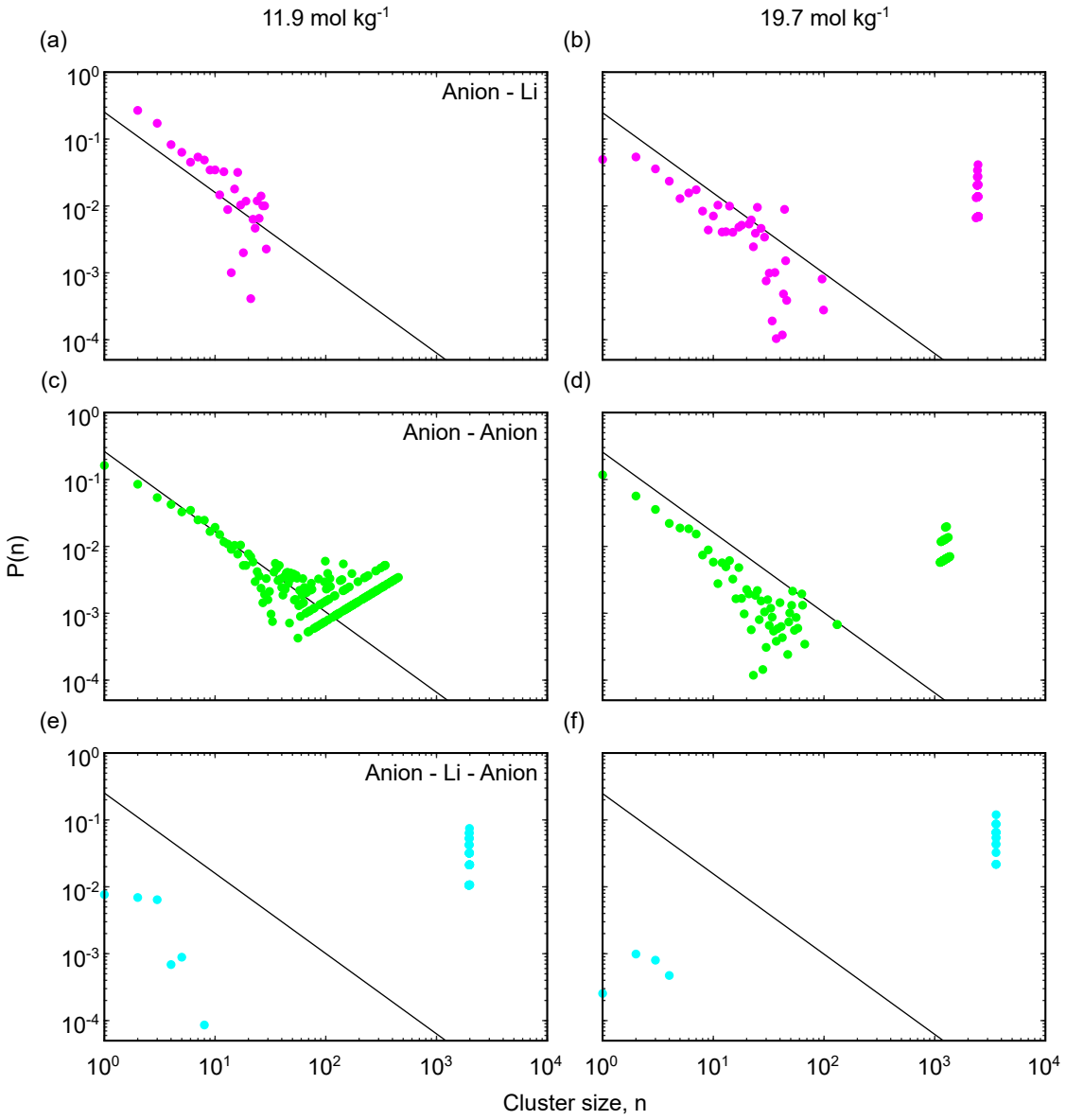


Figure 4.10: Cluster analysis of 100 snapshots of the simulation boxes in aqueous $LiNTf_2$ focusing on anion interactions. The plots show the probability of finding a molecule within a cluster containing *n* molecules against the size of the cluster, *n*. The solid black lines on the plots show the percolation threshold. (a) and (b) show anion-lithium clusters, (c) and (d) show anion-anion clusters, and (e) and (f) show anion-lithium-anion clusters. (a), (c), and (e) show analysis of the 11.9 m system, and (b), (d), and (f) show analysis of the 19.7 m system.

interactions of anions, as shown in figure 4.10. We begin with the clusters observed when considering anion interactions with lithium ions, shown in figure 4.10 (a) and (b). At the lower concentration, we find a slight preference for small clusters containing up to 30 ions, but no ex-

tensive lithium solvating anion network. In contrast at 19.7 m we do find a lithium-anion network that extends through the entire box. This observation shows there is a preference for lithium solvation by water molecules: at 11.9 m, when there is still significant water, the majority of lithium ions are solvated by water molecules, recall a coordination number of 3.6 water oxygens around each lithium ion compared to 1.0 for NTf_2 oxygens. This means that the concentration of lithium ions is low in the hydrophobic anion domain, and it is unlikely that NTf_2 ions are found binding multiple lithium ions. As such, the only clusters found by our analysis are small. Increasing the salt concentration means that there are fewer water molecules per lithium ion and lithium ions are forced into the hydrophobic anion domain. This means lithium ions that bridge NTf_2 ions become more common, and we observe an extensive domain that covers the entirety of the box.

Considering only anion-anion interactions, plotted in figure 4.10 (c) and (d), substantial anion clustering at both concentrations is seen: at 11.9 m we see anion clusters of $\sim$ 450 ions, while at 19.7 m we see clusters that encompass the entire box. This analysis appears to show that whilst large anion-anion clusters are expected at 11.9 m, they do not percolate throughout the entire box. However, by considering anions bridged by lithium ions, looking at the anion-lithium-anion clusters shown in figure 4.10 (e) and (f), we see that such clusters are able to percolate through the box at both concentrations studied. The observation of different clustering extents found by considering different interactions of the anion with other anions and lithium ions is shown in figure 4.11. This is similar to the observation made in water at 11.9 m, where again lithium ions are required to form bridges between clusters in order to see an extended water-lithium network throughout the struc-

ture. Taken together, this means that at 11.9 m, there is no extensive network consisting of either anions or water - it is only by considering the role of lithium ions that bridges can be formed between small anion- or water-rich clusters, leading to the extensive domain structure.

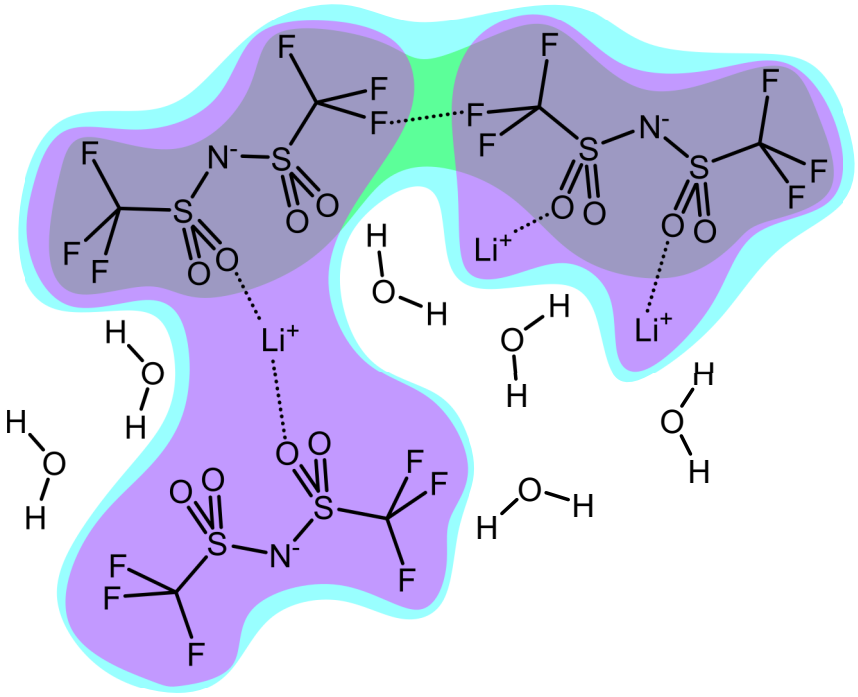


Figure 4.11: Anion-centred cluster analysis. When only anion-lithium (figure 4.10 (a) and (b)) or anion anion (figure 4.10 (c) and (d)) interactions are considered individually, smaller clusters are observed at 11.9 m. However, when anion-lithium and anion-anion interactions are both considered (figure 4.10 (e) and (f)), clusters can percolate through the entire box at both studied concentrations. Only interactions considered in the relevant cluster analyses are shown.

4.2.3 | Void Analysis

The cluster analysis described above allows us to see how molecules are grouped, and provides an observation as to the extent of these clusters in the liquid, but does not give an insight into the length scale of the domains to compare with our measured SFB results. In order to obtain such a dimension, we use a void analysis to study snapshots of our simulation boxes. A second Python programme, designed and writ-

ten by James Hallett, based on the work by Koumakis *et al.* was used to perform this analysis[191]. In this method, atoms from the molecules or ions of interest are deleted. Spheres are then expanded at 10^5 random points in the simulation box, and the expansion stops once any atom is encountered. The spheres are prevented from forming within an atom, defined by a radius of 0.12 nm (Van der Waals radius of a hydrogen atom). This is carried out for 10 separate snapshots, giving 10^6 data points in total. In this way, the minimum dimension of voids left behind by deleting e.g. all the water molecules may be measured, in order to quantify the size of the observed domains.

We measure voids left behind on deleting all of the anion and lithium atoms, to quantify the size of the anion and anion-solvated lithium clusters; and voids left behind on deleting all of the water and lithium atoms, to quantify the size of the water and water-solvated lithium clusters. As a control, we also measure voids left behind when deleting no atoms. If the clusters are spherical, then the volume of the largest voids observed should correspond to the number of participants in the cluster as measured by the cluster analysis above. However, if the clusters are truly a percolating network as we have hypothesised, we should measure a void volume that is much too small to accommodate all the members of a cluster. The results of this void analysis are shown in figure 4.12.

For each system at each concentration, the probability of finding a void of a given radius increases to a maximum value, followed by a sharp decrease. The gradient of the increase is the same regardless of identity of the species probed. These small radius voids arise as a consequence of the packing of atoms in liquids - small gaps in close packed regions always arise, and with the same frequency regardless

of the identity of the liquid considered. A maximum value in the probability distribution of minimum void radius is also expected, as large voids are extremely unlikely in condensed liquid mixtures. The position of this maximum value moves to the right (greater void dimensions) as clustering species are deleted. This is expected as the process creates gaps in the packed liquid structure.

At 11.9 m, the water and anion void dimension probability distribution follows a similar trajectory. This is reflected in the largest measured minimum void dimension, recorded in table 4.3: both anion and water voids show a largest minimum void dimension of ≈ 0.4 nm. This means that at this concentration, the shapes of the hydrated cation domains and of the non-aqueous anion domains are roughly similar. Further, this largest dimension is far too small to account for the large numbers of molecules and ions contained within clusters as measured in the above cluster analysis (recall, the largest dimension of the anion is ≈ 1 nm, shown in figure 3.2), thus reinforcing the idea of the clusters forming extended narrow channels that percolate through the liquid.

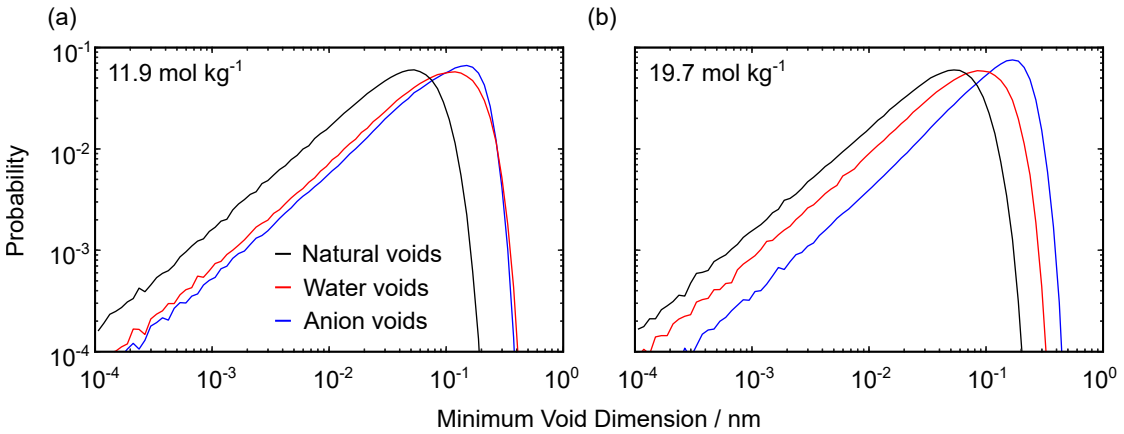


Figure 4.12: Probability distribution of the minimum void dimension at each concentration considering voids made by deleting anion and lithium atoms (anion voids, blue), water and lithium atoms (water voids, red), and nothing (natural voids, black). The void analysis at 11.9 m is shown in (a) and at 19.7 m in (b). Small gaps between atoms occur in all cases, so all lines have the same gradient until some threshold value.

These channels can have a maximum diameter of ≈ 0.8 nm.

On increasing the concentration to 19.7 m, figure 4.12 and table 4.3 show that the voids created on deleting anions grow and those formed by deleting the water molecules shrink as additional salt is added to the system. As at the lower concentration, the observed largest minimum void radius is much too small to accommodate significant spheres forming, and instead the clusters take the form of narrow channels through the liquid. This observation means that the domain structure is not characterised by a uniform shape, but that it changes with concentration. As additional salt is added, the effect is to 'thin' the hydrated cation domain, as well as to break up the domains as seen in the cluster analysis. Such a domain thinning will again disfavour a vehicular method of lithium ion transport as it becomes harder for water-solvated lithium ions to move through the hydrated cation domain. This thinning of the domains can be seen in the snapshots shown in figure 4.4.

Table 4.3 details the largest observed minimum domain radius dimension at each concentration for the hydrated cation domains and the non-aqueous anion domains. The largest domains have a breadth of twice the minimum domain radius dimension, and thus, like points in adjacent hydrated cation domains separated by a non-aqueous anion domain (or vice versa) will be at a distance apart that is smaller than the sum of these maximum domain breadths. At 11.9 m, we expect a maximum separation of 1.69 nm, and at 19.7 m, we expect a maximum

Table 4.3: Largest minimum void radius dimension measured at each concentration considering voids made by deleting anion and lithium atoms (anion voids) and water and lithium atoms (water voids).

Void Type	11.9 mol kg^{-1}	19.7 mol kg^{-1}
Anion Voids	0.411 nm	0.505 nm
Water Voids	0.435 nm	0.380 nm

separation of 1.77 nm, and indeed, we expect to often find points at distances slightly closer than these maxima. This gives distances between domains similar to the layering wavelength as measured in the surface force balance, described in chapter 3. We therefore conclude that it is the observation of these domains that gives rise to the large oscillations observed by the SFB, as we initially hypothesised[62].

When the SFB surfaces are close together, the negative charge of the mica templates the domains such that they lie in layers against the surfaces. These layers can be measured with a characteristic wavelength. In the bulk, the water-in-salt electrolyte domains form a percolating network with a characteristic correlation parameter that corresponds to the wavelength measured in the SFB. These ideas are shown in figure 4.13.

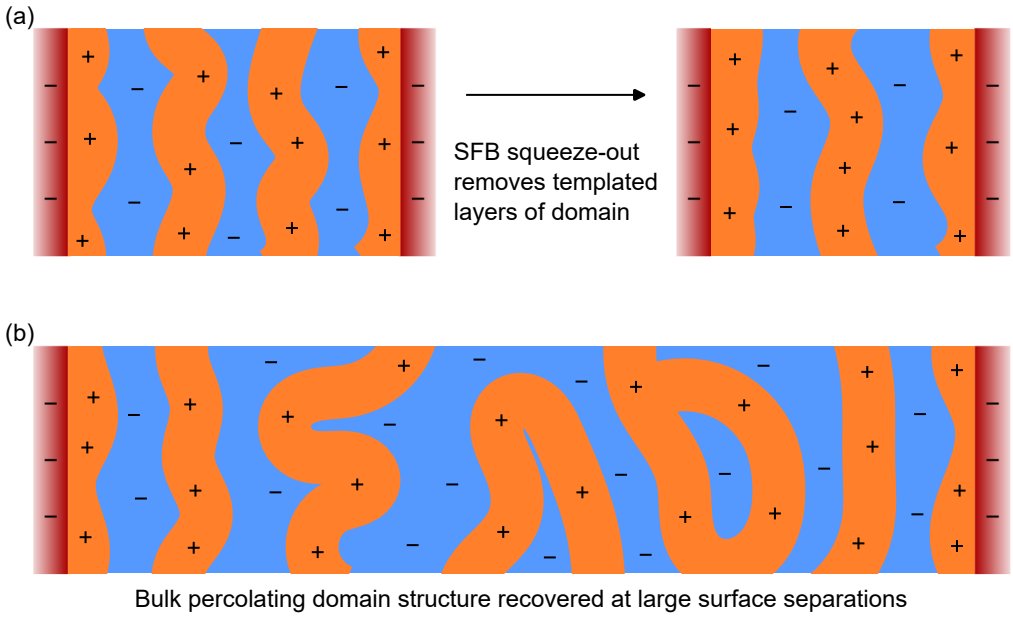


Figure 4.13: Cartoon showing surface and bulk structure of the WiS. In (a), the WiS is confined as in the SFB and forms layers of a characteristic wavelength. In (b), the WiS is able to form a percolating domain network with a characteristic correlation length that corresponds to the wavelength measured in the SFB. The hydrated cation domain is shown in orange and the non-aqueous anion domain is shown in blue.

4.3 | Summary

In summary, we have performed coherent elastic neutron scattering measurements on the water-in-salt electrolyte $LiNTf_2$, both at a concentration similar to those measured in the SFB in chapter 3 and at a concentration close to saturation. In each case, we observed a long range correlation length of ≈ 1.2 nm, similar to the oscillatory wavelength observed within the SFB. Using empirical potential structure refinement techniques, we generate simulation boxes in which the liquid structure is assumed to be similar to that of the bulk liquid. Analysis of these models suggest a bulk liquid structure similar to that proposed in our surface forces study, with interpenetrating domains consisting of lithium ions solvated by water - the hydrated cation domain, and lithium ions solvated by NTf_2 ions - the non-aqueous anion domain.

We have shown that the environment of water in these systems is substantially different from the environment in pure water. These changes will affect the electronic structure of the water molecules, allowing WiS electrolytes to show broad electrochemical stability windows. We have also shown that at the highest concentration, water-rich channels within the liquid are narrow and do not extend throughout the entire liquid. This observation supports the theory that lithium ion transport throughout water-in-salt electrolytes is enabled by solvation shell hopping between the domains, rather than by a vehicular mechanism through the hydrated cation domain.

Overall, this study has shown the value in the complementary techniques of the surface force apparatus and neutron scattering in determining liquid structure, and made observations that will be critical in understanding the behaviours and optimising the applications of water-in-salt electrolytes.

5 | Oscillatory Forces in Ionic Liquid Mixtures

Ionic liquids are salts that exist in the liquid state. This broad definition encompasses a wide range of systems, including traditional inorganic salts such as sodium chloride, which melts to form a molten salt at temperatures in excess of 801 ^{o}C. In this chapter, we focus on the narrower regime of room temperature ionic liquids, and use the term 'ionic liquid' to denote any salt with a melting point below room temperature. The first room temperature ionic liquid was discovered by Paul Walden in 1914. He found that the salt ethylammonium nitrate, $[EtNH_3][NO_3]$ had a melting point of just 12 ^{o}C, well below that of most inorganic salts[192]. Here, we focus on the differences in structure between two ionic liquids, 1-ethyl-3-methylimidazolium bis(trifluoromethanesulfonyl)-imide, $[C_2C_1Im][NTf_2]$, and 1-decyl-3-methylimidazolium bis(trifluoromethanesulfonyl)imide, $[C_{10}C_1Im][NTf_2]$, as measured in the surface

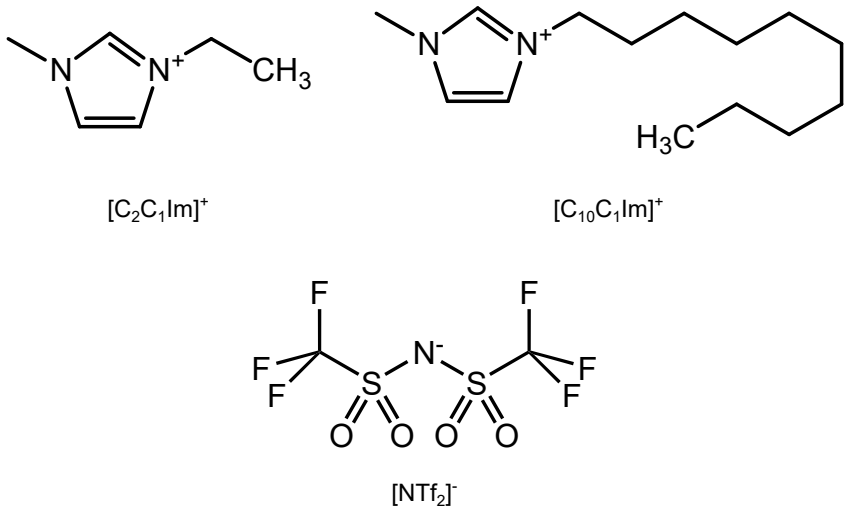


Figure 5.1: Structure of the molecular ions investigated in this chapter, showing the cations above and the anion below. The anion is common to both ionic liquids.

force balance, and discuss the effects of this structuring on mixtures of the two ionic liquids. The molecular ion structures of the ionic liquids investigated in this chapter are shown in figure 5.1.

5.1 | Background and Motivation

Ionic liquids are liquids comprised solely of ions, and represent perhaps the clearest possible departure from the classical understanding of electrolytes discussed in chapter 1. The study of ionic liquids has rapidly expanded over the past few decades, and ionic liquids have shown potential for use in myriad applications[192]. Ionic liquids have been proposed as environmentally responsible 'green solvents'[193,194]; as solvents for cellulose, lignin and other biomass[195–197]; as agents for carbon dioxide capture[198]; as components of electrochemical energy storage devices and fuel cells[199,200]; and as lubricants and lubricant additives[201–203]; alongside many other uses and applications across chemistry, physics and engineering.

Such broad applicability is possible because of the many and various desirable properties that are found across ionic liquid systems. They can have low volatilities, high chemical, thermal and electrochemical stabilities and conductivities, broad liquid ranges, and low flammabilities. However, the extent to which ionic liquids show these properties depends on the constituent ions that make up the liquid[204].

5.1.1 | Designer Ionic Liquids

The properties of an ionic liquid can be tuned by choosing an appropriate cation-anion pairing. As a result, ionic liquids are often called 'designer solvents' as the liquid properties can be designed by choosing a pair of ions that give rise to desirable properties for an applica-

tion[205]. These ions are often large molecular ions with many degrees of freedom, giving rise to a large entropic driving force that prevents crystallisation. They may be aprotic or protic[206], polymeric[207], or involve multiple components such as in solvate ionic liquids or deep eutectic solvents[208,209]. Some examples of the ions that may be used in ionic liquids are shown in figure 5.2.

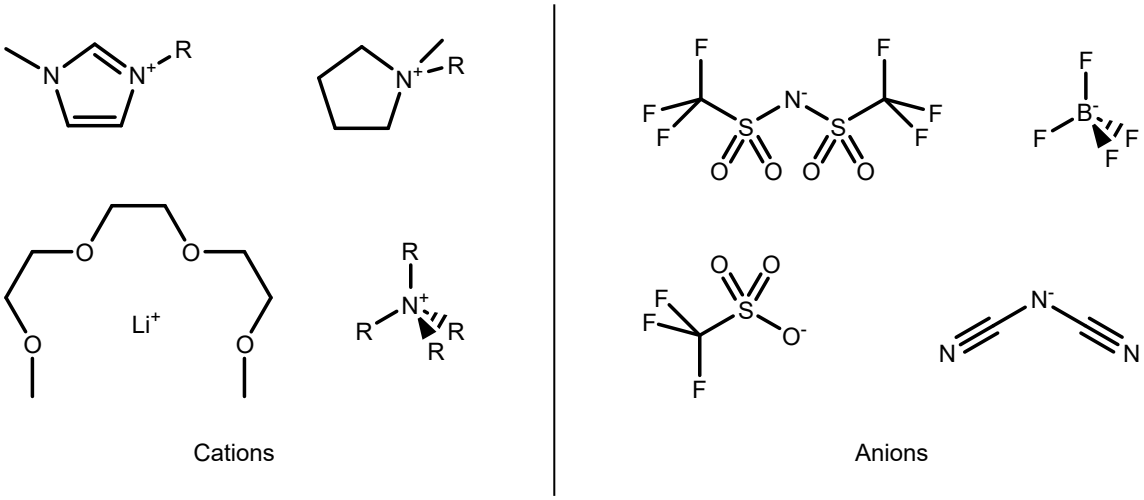


Figure 5.2: Structures of some common ionic liquid ions. R groups can be alkyl, aryl, protic, or polymeric. Combinations of different cations and anions give rise to different ionic liquids with tunable properties.

5.1.2 | Ionic Liquid Structure

A lot of study has been devoted to trying to understand the structures present in ionic liquids, both in the bulk liquid, and at interfaces. Simulation studies of the liquid in the bulk saw evidence for the ordering of ionic liquids into domain regions, similar to those described for WiS electrolytes in chapters 3 and 4. The domains consisted of charge rich regions, where the charge carrying groups of the ionic liquid ions accumulated, and charge poor regions, rich in aliphatic and apolar tail groups of the ions[210]. These findings have since been experimentally backed up in scattering measurements[211–213]. As the length of the aliphatic region of ionic liquid ions increases, the size of the aliphatic

rich domains increases, until eventually the liquid can organise into a percolating network of interpenetrating domains.

Studies of ionic liquids at surfaces have also found substantial evidence for order and structure in the liquid. Roger Horn first investigated the properties of a protic ionic liquid within the surface force balance[66]. He found an oscillatory force at the mica surfaces where the wavelength of the oscillatory force was comparable to the mean ion pair diameter. Further studies of the behaviour of ionic liquids at smooth surfaces using the SFB, AFM, and reflectivity techniques, found similar behaviour for ionic liquids with short chain aliphatic groups[67,214,215], and suggested that these ions form ABAB type ion ordering at the surface that decayed away into the bulk liquid. However, measurements on longer chain ionic liquids revealed a significant switch in the oscillatory wavelength as the aliphatic chain length is increased: the observed wavelength remains similar for increasing aliphatic chain length until some threshold length is reached, beyond which the wavelength is much larger than the mean ion pair diameter[24,68,69,216]. This arises due to a change in layering behaviour, from alternating layers of anions and cations in which the aliphatic chain lies against the surface, to bilayer type structures with aliphatic chains pointing away from the surface. These layering behaviours against smooth surfaces are shown schematically in figure 5.3.

5.1.3 | Mixtures of Ionic Liquids

A further method of tuning ionic liquid properties in order to make 'designer solvents' is to mix two ionic liquids together to achieve more desirable properties than either liquid has alone[27,217–219]. Many studies have investigated various properties of mixtures of ionic liquids, includ-

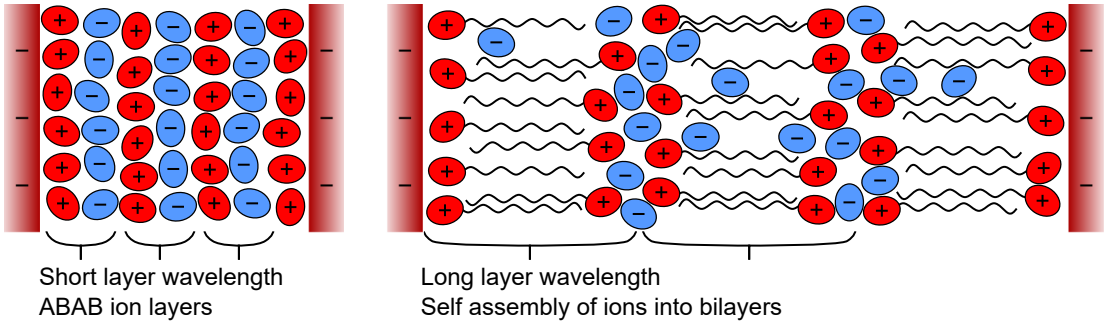


Figure 5.3: Cartoon representation of layering behaviour in ionic liquids. Ionic liquids with small aliphatic regions form ABAB layers of alternating cations and anions templated by the surface charge. Ionic liquids with large aliphatic regions form bilayers, with charge rich and charge poor domains.

ing studies of the density, phase behaviour, conductivity, and viscosity of mixtures[220–223].

Work has also investigated structuring in ionic liquid mixtures. One particular point of interest has been the existence of domains in ionic liquid mixtures, and the extent to which native ionic liquid domain structures in pure liquids are destroyed or reinforced by mixing ionic liquids. Some ionic liquids are found to be miscible at the molecular scale, while others remain effectively nano-segregated, existing as discrete domains of pure ionic liquids[27,224–226]. Scattering and simulation studies have shown that these effects will depend on the chain lengths in the constituent ions of the mixture[152,225]. Examples of various types of ionic liquid behaviour are shown in figure 5.4.

The effects of ionic liquid mixtures on surfaces at interfaces and in confinement remains poorly investigated. One study by Smith *et al.* investigated an equimolar mixture of short and long chain ionic liquids with a common anion using an SFB.[24]. They noted that the forces were altered significantly from the pure case, suggesting that both cations were present in the confined film, and noted similarities between the observed forces in the mixture and those in the long chain ionic liquid, suggesting a distorted bilayer type structure. However, these meas-

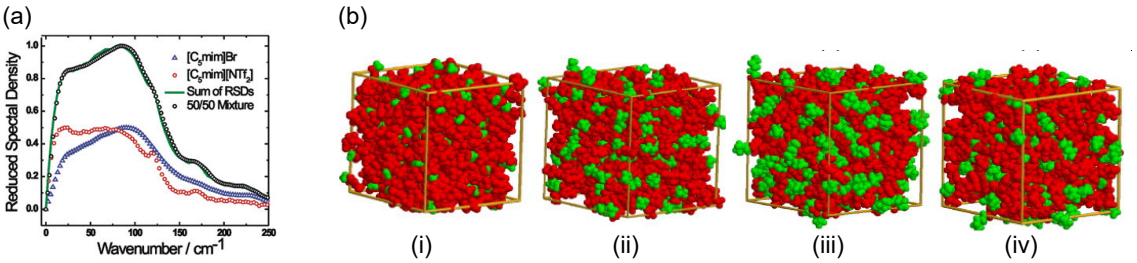


Figure 5.4: Literature data highlighting varying mixing behaviours of ionic liquids. (a): Additivity in the Optical Kerr Effect structure of liquid mixtures of $[C_5C_1Im][NTf_2]$ and $[C_5C_1Im]Br$ suggest the liquids within the mixture are nano-segregated. Reproduced from a work by Xiao *et al*[224]. (b): Molecular dynamics simulations on (i) $[C_2C_1Im][NTf_2]$, (ii) $[C_4C_1Im][NTf_2]$, (iii) $[C_6C_1Im][NTf_2]$, and (iv) a 1:1 mixture of $[C_2C_1Im][NTf_2]$ and $[C_6C_1Im][NTf_2]$ show that the liquids can separate into charge rich (red) and charge poor (green) regions, with the mixture of long and short chains most closely resembling the intermediate chain cation ionic liquid structure. Reproduced from a work by Shimizu *et al*[225].

urements were at a much lower force resolution than is now possible with modern SFB techniques, and the surface structure of ionic liquid mixtures remains an important property for in-depth study, with consequences across a wide range of applications for ionic liquid mixtures.

5.2 | Experimental Details

We investigated the surface forces and structures present in two well characterised ionic liquids, 1-ethyl-3-methylimidazolium bis(trifluoromethanesulfonyl)imide, $[C_2C_1Im][NTf_2]$, and 1-decyl-3-methylimidazolium bis(trifluoromethanesulfonyl)imide, $[C_{10}C_1Im][NTf_2]$, and their mixtures using the surface force balance as described in chapter 2. The high viscosities of ionic liquids mean that mechanical vibrations within the SFB were damped during measurements, while the low ionic liquid vapour pressures prevented cooling effects due to evaporation. As a result, mechanical and thermal drifts in these systems were minimised, and approach and retraction velocities of 0.2 nm s^{-1} could be made. Here, details specific to these experiments are discussed.

5.2.1 | Material and Mixture Preparation

The structures of $[C_2C_1Im][NTf_2]$ and $[C_{10}C_1Im][NTf_2]$ are shown in figure 5.1. Pure ionic liquids (Iolitech, $[C_2C_1Im][NTf_2]$ >99.5 %, $[C_{10}C_1Im][NTf_2]$ >98 %) were dried on a Schlenk line at 70 ^oC for $\sim$ 24 hours to remove absorbed water content and volatile impurities before use. A test using a Karl-Fischer titration method on pure $[C_2C_1Im][NTf_2]$ prepared in this way found water content in the ionic liquid to be < 200 ppm. All handling of the ionic liquids took place in an LFH using acid-cleaned tools and glassware as described in chapter 2.

Mixtures of ionic liquids throughout this chapter are referred to by the mole percent of $[C_2C_1Im][NTf_2]$. We prepared three ionic liquid mixtures at 50 %, 30 %, and 10 % $[C_2C_1Im][NTf_2]$, again in an LFH using acid-cleaned tools and glassware. After preparation, the ionic liquid mixtures were dried on a Schlenk line at 70 ^oC for $\sim$ 24 hours to remove absorbed water content and volatile impurities. The exact concentrations of ionic liquid mixtures investigated are detailed in table 5.1.

5.2.2 | Refractive Indices

Refractive indices for pure ionic liquids are well tabulated in the literature. Here we have used the work of M. Tariq for the refractive indices of the pure ionic liquids[227]. However, there is much less literature data detailing the refractive indices of ionic liquid mixtures, and as such we measure these as described in chapter 2. A measurement was made on each solution multiple times to ensure reproducibility, and the exact temperature recorded. The literature and measured values for the refractive indices, alongside the measured temperatures, are shown in table 5.1.

Table 5.1: Concentrations as mole percent $[C_2C_1Im][NTf_2]$ and as exact molar ratios, and the literature or measured value for refractive index at each concentration investigated[227]. Errors in the measured refractive indices are ± 0.0001, and errors in the measured temperatures are ± 0.1 °C.

Mole percent $[C_2C_1Im][NTf_2]$	Molar Ratio, $[C_2C_1Im]$:$[C_{10}C_1Im]$	Refractive Index	Temperature /°C
100	1:0	1.42351[227]	20.0
50	1:1.0	1.43109	20.0
30	3:7.2	1.42853	20.3
10	1:9.0	1.43509	20.4
0	0:1	1.43557[227]	20.0

5.3 | Pure Ionic Liquids - Measurements and Discussion

In order to fully investigate the effect of mixing ionic liquids on the ionic liquid surface structure, it is first vital to understand the surface structure of the pure ionic liquids. Normal forces recorded in pure $[C_2C_1Im][NTf_2]$ and $[C_{10}C_1Im][NTf_2]$ are shown in figure 5.5. Forces are normalised by the radius of curvature of the cylinders at the measurement spot such that the recorded values are independent of the surface geometry, and may be related to the free energy of interaction between two parallel surfaces: $F_N/R = 2\pi G$, as in equation 2.1. Forces are distinguished by whether they are measured during an approach of the surfaces (light colours) or during a retraction (dark colours). We also make use of stepwise, or static retractions to provide additional measurements of jump out positions and forces (triangles).

As in chapter 3, at surface separations between 2 and 10 nm we see a series of repulsive hard walls separated from adhesive wells, with jumps between walls and from wells arising due to the spring instability associated with the technique. These force profiles have the form of a decaying oscillation, suggesting a well defined, ordered liquid structure

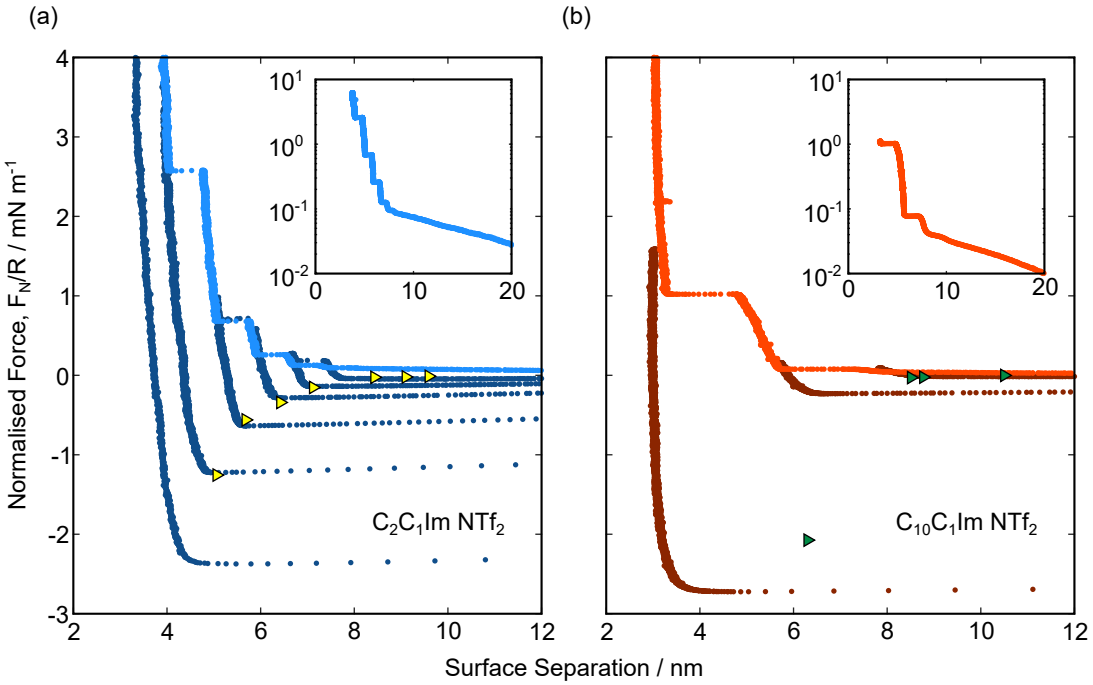


Figure 5.5: Force profiles of pure ionic liquids. Forces are normalised by the radius of curvature of the lenses, and forces measured on approach of the SFB surfaces are shown in brighter colours, while those measured on retraction are shown in darker colours. Jump out positions and calculated forces measured using the static retraction technique are shown as triangles. Forces measured in $[C_2C_1Im][NTf_2]$ are shown in (a), and those measured in $[C_{10}C_1Im][NTf_2]$ are shown in (b). In each liquid, layers are seen, with layers labelled as $i = 1$ at closest approach. Long range forces are also observed for each liquid, and are highlighted in the insets.

is present at the liquid mica interface, and we can again label the short range region of the force profile the 'structural force'. We also see a long range component of the force at surface separations greater than 10 nm, significantly smaller in magnitude than the structural force, and only measurable when the structural force has decayed substantially. This force, shown in the insets of figure 5.5, is repulsive, and follows a monotonic exponential decay We label this region of the force profile the 'long range force'.

5.3.1 | Fitting Pure Ionic Liquid Force Profiles

This form of short range oscillatory structural force and monotonic exponential long range force is now well documented in ionic liquid meas-

urements with the surface force apparatus[24,59,60,66–73,153–157]. To fully quantify our measured forces, we fit them to equation 3.1, reproduced here for clarity:

$$\frac{F_N}{R} = A\ e^{-D/\lambda_o}\cos\left(\frac{2\pi}{\xi}(D+\delta)\right) + B\ e^{-D/\lambda_s} \qquad \text{(3.1 revisited)}$$

Once again, the first term in equation 3.1 describes the structural force, where A is the magnitude of the force, λ_o describes the decay of the oscillatory window, ξ describes the oscillatory wavelength, and δ describes an offset in the oscillations. The second term describes the long range force, where B is the magnitude of the force and λ_s describes an exponential screening length. The force is normalised by the radius of curvature at the contact spot, allowing comparisons between measurements. We also note that A and B may be converted to absolute free energies per unit area by dividing equation 3.1 through by 2π, as described in equation 2.1.

As was the case for the water-in-salt electrolyte, the magnitude of the structural oscillatory force is much larger than the magnitude of the monotonic long range force while the decay length is smaller ($A \gg B$, $\lambda_o < \lambda_s$), and as such it is reasonable to fit each term in equation 3.1 separately. The fitting process is highlighted for $[C_2C_1Im][NTf_2]$ in figure 5.6. An identical process can be completed for $[C_{10}C_1Im][NTf_2]$, and the resulting fits are shown superimposed on the measured force profile in figure 5.7.

In general, the form of the calculated fit matches closely with the measured force profile, particularly at low forces. However, as seen for the WiS electrolytes in chapter 3, deviations can occur at larger compressive forces due to mechanical pressures that lead to deviations from equation 3.1.

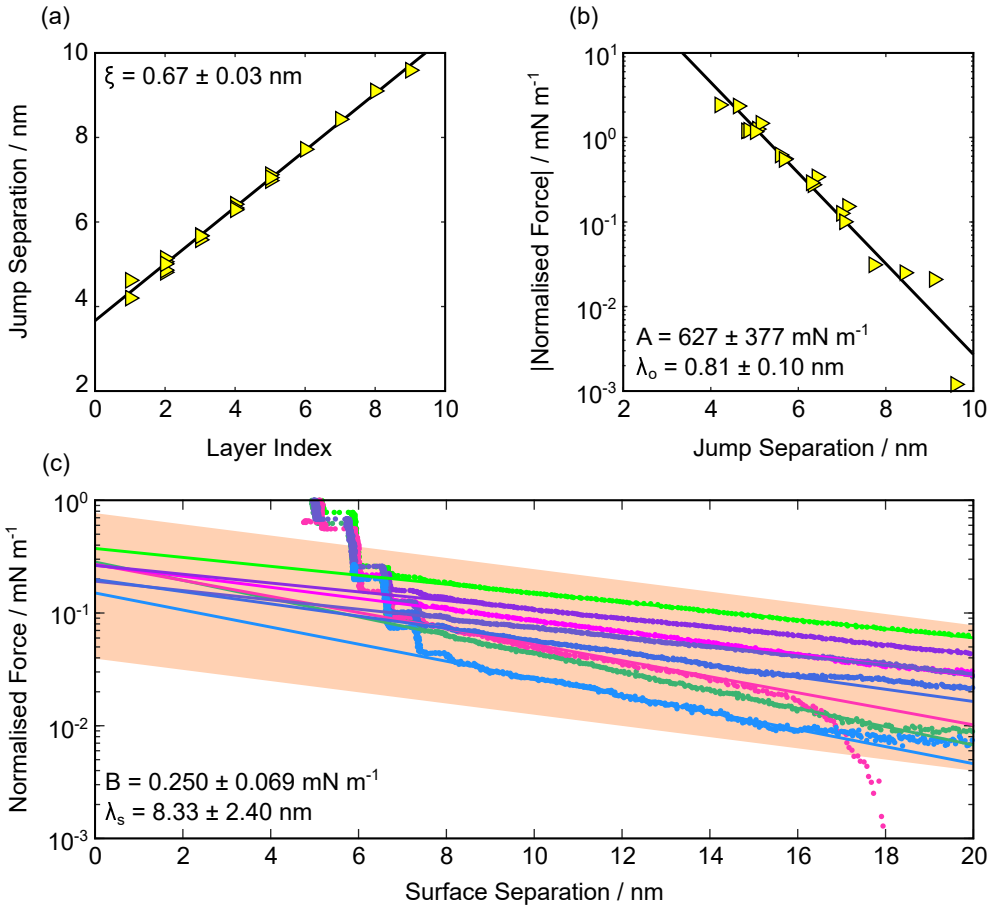


Figure 5.6: Fitting process for a measurement on pure $[C_2C_1Im][NTf_2]$. (a): Surface separations of jump out positions are plotted against layer index. The wavelength of oscillations is given by the gradient. (b): Adhesive forces plotted against jump out positions. The magnitude of the structural forces is given by the intercept, while the characteristic decay length of the oscillations is given by the gradient. (c): Multiple slow approach force profiles are shown on a logarithmic force scale. Fits (solid lines) of each run at separations from 9 to 15 nm gives a magnitude and decay length of the long range force for each run. The mean and standard deviation of these values is shown.

5.3.2 | Forces in Pure Ionic Liquids

Here we discuss the interpretation for the forces measured in pure ionic liquids. Table 5.2 shows the calculated parameters from equation 3.1 to allow for comparison. We also tabulate values of $A/2\pi$ and $B/2\pi$ to access the absolute free energies of the interactions giving rise to these forces. We note that λ_o, ξ, and λ_s are remarkably consistent across multiple experiments on the same liquid. This suggests that the model

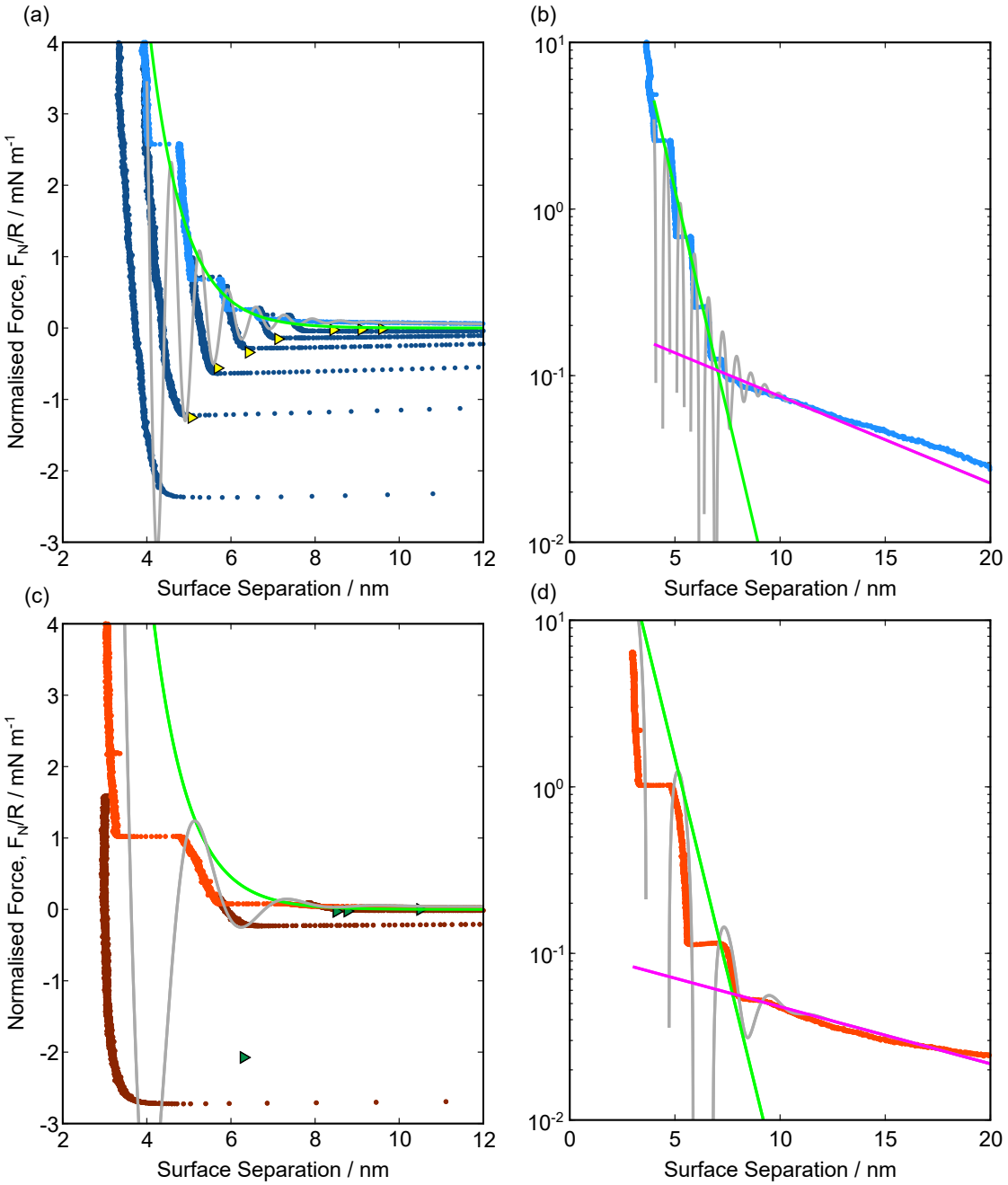


Figure 5.7: Measured force profiles with superimposed fitted force profiles in pure ionic liquids $[C_2C_1Im][NTf_2]$ (blue, (a) and (b)) and $[C_{10}C_1Im][NTf_2]$ (red, (c) and (d)). The fit follows equation 3.1, with parameters calculated as in figure 5.6 and given in table 5.2. The full fit from equation 3.1 is shown in grey, while the exponential decay of the structural ($A\ e^{-D/\lambda_o}$) and long range ($B\ e^{-D/\lambda_s}$) forces are shown in green and magenta respectively.

force profiles described by equation 3.1 capture behaviour that is characteristic of the liquid studied. Such an observation is not surprising: the nature of the force profile measured at the liquid-solid interface is

Table 5.2: Fitted parameters from equation 3.1 for the pure ionic liquids studied in this investigation. We also show A and B as absolute free energies of interaction

Parameter	$[C_2C_1Im][NTf_2]$	$[C_{10}C_1Im][NTf_2]$
A / mN m^{-1}	627 ± 377	576 ± 436
$A/2\pi$ / mJ m^{-2}	100 ± 60	92 ± 69
λ_o / nm	0.81 ± 0.10	0.84 ± 0.17
ξ / nm	0.67 ± 0.03	2.20 ± 0.15
δ / nm	0.1 ± 0.5	1.3 ± 0.5
B / mN m^{-1}	0.250 ± 0.069	0.105 ± 0.042
$B/2\pi$ / mJ m^{-2}	0.040 ± 0.011	0.017 ± 0.007
λ_s / nm	8.33 ± 2.40	12.68 ± 3.43

intrinsically related to the behaviour of the bulk liquid[23], and thus we suggest that λ_o, ξ, and λ_s are properties of the bulk liquid. On the other hand, we find substantially larger scatters in A, B, and δ, perhaps suggesting that these parameters are more sensitive to surface effects, including mica twist angle or adsorbed species.

The magnitudes of the structural force A are very similar in the two liquids, however in each case there is a large error. This parameter is highly dependent on the relative orientations of the two mica surfaces[149], and can depend on surface chemistry and charge. However, large values of A suggest very tightly held ions close to the surface that are very difficult to squeeze out. This is not unexpected for liquids comprised solely of ions. The negatively charged mica surface will strongly electrostatically bind an initial layer of cations that are able to resist large compressive forces of the SFB. A strongly bound surface layer may then strongly interact with the next ion layer, and so on, decaying into the bulk liquid.

The parameter δ corresponds to an offset in the oscillatory struc-

tural forces. Small changes in the optical path from the calibration can lead to small errors in δ in a manner that is difficult to quantify. However, δ should always be small and positive in a dielectric medium, as a thin film with a net positive charge must always be present between the surfaces to ensure charge neutrality. Thus, it is intuitive that δ for $[C_2C_1Im][NTf_2]$ (short chain cations) is smaller than $[C_{10}C_1Im][NTf_2]$ (long chain cations), as we observe.

The characteristic decay length of the structural force is given by λ_o. It is interesting to note that λ_o is similar, not just for the two liquids discussed here, but also for the WiS electrolytes described in chapter 3. As before, we interpret λ_o as the ability of the mica surfaces to template layers against themselves, and the similarity of λ_o across a wide range of ion dense liquids suggest that the interactions that allow the surface to impose order on the molecules and ions close to the surface are largely independent of the precise liquid identity.

Structural differences between the two liquids are characterised by the parameter ξ. This is the wavelength of the oscillations, and by analysis of this quantity, the makeup of the structures that are squeezed out from between the SFB surfaces to give rise to the structural force can be inferred. As in the case of the water-in-salt electrolytes, these layers must be charge neutral. We describe above how ionic liquids can form structures of either ABAB layers of alternating cations and anions between the surfaces, or, in the case of ions with long chain aliphatic regions, bilayers with alternating polar and non-polar domains.[24,67–69,214–216]. These structures are shown in figure 5.3.

For $[C_2C_1Im][NTf_2]$, $\xi = 0.67 \pm 0.03$ nm. The mean ion pair diameter, d of $[C_2C_1Im][NTf_2]$ can be computed by considering the density ρ and

molar mass M_r of the liquid:

$$d = \left(\frac{M_r}{\rho N_A} \right)^{\frac{1}{3}} \tag{5.1}$$

$[C_2C_1Im][NTf_2]$ has a density of 1.52 g cm^{-3} and a molar mass of 391.31 g mol^{-1}, which gives a mean ion pair diameter of 0.75 nm (Data sourced from Iolitec[228]). The mean ion pair diameter is comparable with ξ, which suggests that this liquid forms an ABAB type alternating anion cation structure, as shown in figure 5.3 *left*. This is expected as the liquid has only small aliphatic regions.

Turning now to $[C_{10}C_1Im][NTf_2]$, the oscillatory wavelength for this liquid $\xi = 2.20 \pm 0.15$ nm. This is much larger than that measured for $[C_2C_1Im][NTf_2]$. The mean ion pair diameter can again be calculated from equation 5.1. In this case, from a density of 1.27 g cm^{-3} and a molar mass of 503.53 g mol^{-1}, the mean ion diameter is found to be 0.87 nm. The large discrepancy between the measured oscillatory wavelength and the mean ion diameter suggests that the ionic liquid is not forming an ABAB structure, but rather is organising into bilayers, as shown in figure 5.3 *right*. Again, this is expected as the cations present in the ionic liquid contain a long aliphatic carbon chain.

These differences in the behaviours of pure ionic liquids at surfaces have consequences for the electrical double layer structures of these systems. It has recently been shown that ionic liquids that are able to self-assemble into bilayer type structures can enhance electrical charge storage at electrode surfaces due to the presence of polar and non-polar domains in such liquids[28]. This observations suggests a possible application for $[C_{10}C_1Im][NTf_2]$ as an electrolyte medium in next-generation electrochemical energy storage devices, such as superca-

pacitors or non-flammable batteries.

Beyond the structural forces, long range forces are observed. As we have discussed before, long range forces are unexpected in concentrated electrolytes, however over the past decade they have been measured in a wide variety of systems by several independent techniques[59,60,71,153–159]. This phenomenon is now known as "underscreening". The magnitude of the long range force, B, is similar for both liquids, and as was the case for the WiS electrolytes in chapter 3, $B \ll A$. This again suggests that only very sensitive measurement and simulation techniques will be able to resolve both the structural oscillatory and the long range monotonic forces simultaneously, and highlights the value of the SFB as such a technique.

The decay length of the long range force λ_s is similar to underscreening decay lengths measured in other pure ionic liquids,[60,71,153,155] highlighting the reproducibility of these measurements. It is interesting to note however that the measured decay length in $[C_{10}C_1Im][NTf_2]$ is longer than that measured in $[C_2C_1Im][NTf_2]$. If significant, this can be explained by studying the scaling law described in equation 3.2, which may be rearranged[155] to give:

$$\lambda_s = l_B a^3 c_{\text{ion}} \tag{5.2}$$

where a is the ion diameter, c_{ion} is the ion concentration, and

$$l_B = \frac{q^2}{4\pi\epsilon_r\epsilon_0 k_B T} \tag{5.3}$$

is the Bjerrum length. The dielectric permittivity ϵ_r of $[C_2C_1Im][NTf_2]$ is known to be 12.0. Increasing the alkyl chain length of imidazolium based ionic liquids increases the dielectric permittivity[229], so it is ex-

pected that the dielectric permittivity of $[C_{10}C_1Im][NTf_2]$ is > 12. The ion density of $[C_{10}C_1Im][NTf_2]$ is less than that of $[C_2C_1Im][NTf_2]$. These effects would combine to reduce λ_s on increasing the alkyl chain length from $[C_2C_1Im][NTf_2]$ to $[C_{10}C_1Im][NTf_2]$. However, the size of the cation also increases. This has the opposite effect, and owing to the cube power, this dominates and thus $[C_{10}C_1Im][NTf_2]$ has a longer screening length than $[C_2C_1Im][NTf_2]$.

The origin of the underscreening force remains an open question, and researchers have suggested that the force may arise from a lower ion concentration due to extensive ion clustering[153], or from uncharged defects within the liquid acting as charge carriers[154]. Recent theoretical work by Roland Kjellander perhaps provides a tantalising clue[165]. In this analysis, interactions in an electrolyte can be described by a sum of exponentially decaying terms, or decay modes, that may be monotonic or oscillatory. Each decay is characterised by a decay length, λ_x, analogous to the Debye length (equation 1.5), given by:

$$\lambda_x = \sqrt{\frac{\epsilon_0 \epsilon^*(\lambda_x) k_B T}{\sum_i n_i q_i q_i^*}} \tag{5.4}$$

where $\epsilon^*(\lambda_x)$ is a renormalised dielectric factor which depends on λ_x, n_i is the bulk density of species i, and q_i^* is a renormalised ion charge. Importantly, this allows for a long range electrostatic decay either when n_i is very small, as is observed with the Debye length for dilute electrolytes, or when n_i is large but q_i^* is very small, such as may be the case in concentrated electrolytes like ionic liquids.

One interpretation of this model is reminiscent of the initial ion clustering interpretation of underscreening[153]. Ions grouped together in large, near neutral clusters could be responsible for the low renormalised ion charge. However, a second interpretation would be to say that

this is an average property for the whole liquid, and that alongside an analysis of the liquid as comprised of individual ions, it is also important to consider the liquid as a bulk entity with statistical properties.

This theory shows promise at establishing a theoretical basis for the experimental observation of underscreening, but the complexities of real electrolytes mean that it is not yet quite clear how to calculate the parameters $\epsilon^*(\lambda_x)$ and q_i^* and thus make quantitative comparisons with our experimental data.

5.3.3 | Non-equilibrium Structural Transitions

The measurements we make generally involve a constant motion of the surfaces, however the velocity of these measurements is much slower than the ability of the liquid to adapt to changes in the surface position, and thus the forces we measure are equilibrium forces. The exception to this is during a jump caused by the spring instability, where the surfaces move together or apart rapidly. Measurements taken during these regions are of non-equilibrium forces, and are often not plotted and rarely discussed in the literature. However, here we demonstrate that discrete structural transitions may be measured during these regions of the force profile. In the case of pure ionic liquids, these transitions may be clearly shown during the non-equilibrium jump-outs, as shown in figure 5.8.

The observation of such transitions during non-equilibrium regions of the force profile suggests a mechanism by which fluid can be incorporated into a crack. As we see discrete transitions that appear to correspond to the liquid layering dimension, it appears that liquid is incorporated layer by layer. At minimum points in the force profile, an integer number of molecular or ion layers exist between the surfaces.

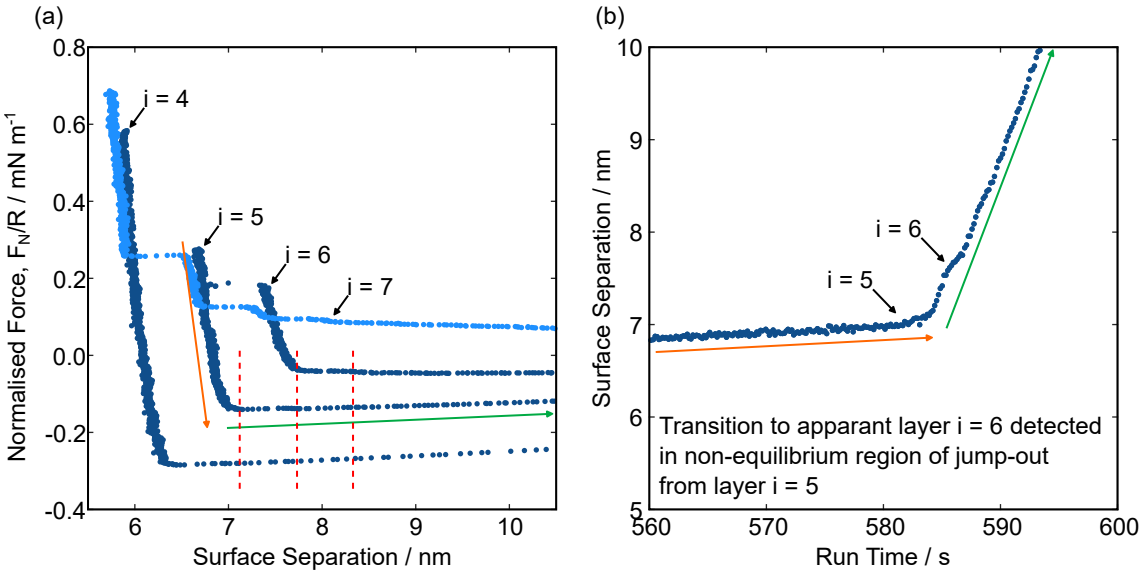


Figure 5.8: Observations of structural transitions during non-equilibrium regions of measurements probing the minima of inner layers in $[C_2C_1Im][NTf_2]$. (a): A zoomed in region of the force profile of $[C_2C_1Im][NTf_2]$ (shown in full in figure 5.5), with retractions (shown in dark blue) from layers $i = 4$, 5, and 6 shown. Layer $i = 7$ is also visible during the approach (shown in light blue). Forces measured that are thought to lie on the equilibrium force profile for layer $i = 5$ are highlighted by the orange arrow, while non-equilibrium forces measured after the spring instability causes a large jump out are shown by the green arrow. Layering transitions are visible in the non-equilibrium region of the force profile, with jumps to positions that appear to correspond to the minima of outer layers. (b): A distance versus time plot of the retraction measurement from layer $i = 5$. A layering transition that would correspond to a jump from $i = 5$ to $i = 6$ is clearly visible.

In order to move the surfaces apart from contact to a position with no interaction, vacuum must be created using elastic energy stored in the spring. This could happen in a single step, with a sudden and large jump out creating a large vacuum that is then filled by liquid, which would involve moving through a large maximum on the energy profile of the retraction. However, our observations suggest that this instead occurs stepwise, with the surfaces following an energy profile that includes small local maxima with the creation of a vacuum only a single ion layer thick. These vacuums are then rapidly filled by a single layer flowing into the crack from the bulk reservoir outside the SFB contact spot, taking the system to a local minimum, before further separation

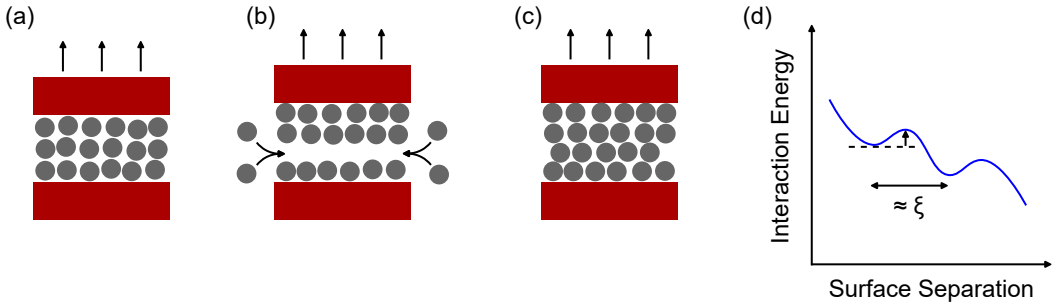


Figure 5.9: Schematic representation of the jump-out process. At a minimum point in a force profile, there is an integer number of molecular or ion layers confined between the SFB surfaces (a). On the application of the spring restoring force during a jump out, the surfaces jump apart through a local maximum, creating a vacuum with dimensions equivalent to a single layer (b). Liquid floods the created gap, taking the system to the next local energy minimum (c). (d) shows the suggested energy profile for such a transition, and highlights that the oscillatory wavelength measured by the equilibrium force profile corresponds to the layering transitions seen in these non-equilibrium regions.

of the surfaces occurs. This process is shown in figure 5.9.

The time spent in each local minimum is a function both of the height of the energy barrier and of the viscosity of the liquid, as low viscosity liquids will rapidly be able to fill the gap. As a result, such non-equilibrium transitions are clearly visible in ionic liquids, where electrostatic interactions give rise to large energy barriers and high viscosities ensure slow filling mechanics. In the case of water-in-salt electrolytes, the much lower viscosities mean such transitions are not seen.

5.4 | Ionic Liquid Mixtures - Measurements and Discussion

With the cases for the pure ionic liquids now well characterised, we move on to present and discuss forces measured in ionic liquid mixtures. Force profiles measured at 50, 30, and 10 mol % $[C_2C_1Im][NTf_2]$ in $[C_{10}C_1Im][NTf_2]$ are shown in figure 5.10, with the forces normalised by the radius of curvature of the lenses at the contact spot. In each mixture, we observe well defined and reproducible structural forces characterised by hard walls and adhesive wells. We also observe a long range

monotonically decaying exponential force. However, there are marked differences between the force profiles as the concentration of the short chain $[C_2C_1Im]^+$ cation is reduced.

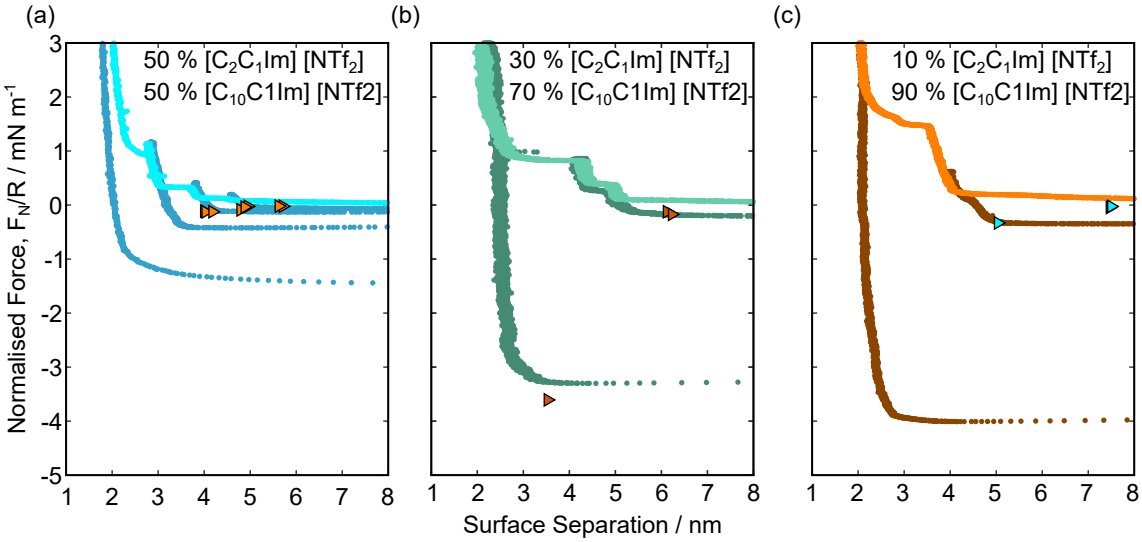


Figure 5.10: Force profiles measured in ionic liquid mixtures at (a): 50 %, (b): 30 %, and (c): 10 % $[C_2C_1Im][NTf_2]$ in $[C_{10}C_1Im][NTf_2]$. Forces measured on approach are shown in the lighter colour while those measured on retraction are shown in the darker colour. Jump out positions and calculated forces measured using the static retraction technique are shown as triangles.

In the case of 50 % $[C_2C_1Im][NTf_2]$, we see a force profile in the form of a series of well defined oscillations, with repulsive barriers increasing in height as the surface separation is increased, and adhesive wells increasing in magnitude as the surface separation is decreased. This force profile is qualitatively similar to those observed in pure ionic liquids, as described above. At the lower $[C_2C_1Im][NTf_2]$ concentrations, however, this simple form of force profile vanishes and is replaced by much more complex behaviour. We now discuss the form of these complex force profiles in more depth.

Figure 5.11 shows a close up view of some interesting features of the force profile measured at low forces in 30 % $[C_2C_1Im][NTf_2]$. Initial surface approach, shown in light green, reveals a small maximum in the force profile at $\approx$ 6.6 nm from absolute surface contact. This is followed

by a jump of ≈ 1.5 nm to a hard wall at ≈ 5.1 nm. Compression here leads to a second, smaller jump of ≈ 0.4 nm to a second hard wall at ≈ 4.5 nm. Compression at this hard wall eventually yields a final jump, however this jump occurs in two stages: the first is rapid, and takes place over similar timescales to the jumps in pure ionic liquids, but the second is much slower. In total, this final jump to the innermost observed hard wall is ≈ 1.6 nm, with the final surface separation at ≈ 2.6 nm. Retraction, shown in dark green, from this innermost hard wall reveals a deep adhesive well. Retractions from the outer hard walls however show some unusual features: rather than showing a single, deep adhesive minimum, multiple minima are observed separated by jumps, similar to those seen on approach of the surfaces. Two jump outs of ≈ 0.5 nm are observed before a final minimum with a jump to large separations is reached. This form of force profile was found to be highly reproducible over ∼ 12 hours of measurements.

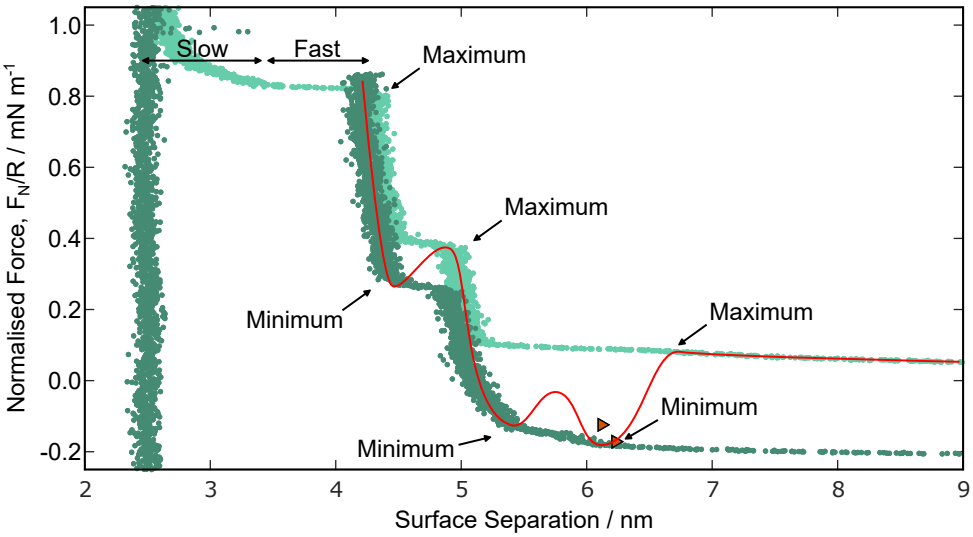


Figure 5.11: Enlarged force profile measured in 30 % $[C_2C_1Im][NTf_2]$. Forces measured on approach of the surfaces are shown in pale green and those measured on retraction are shown in dark green. Measured maxima and minima are highlighted. Several inner minima exist at lower adhesive force than minima observed at greater surface separations, so jumps are observed during retraction force measurements. The red line is shown as a guide to the eye to suggest the approximate shape of a force law consistent with the measurements.

These observations have important consequences for the form of the equilibrium forces that exist in the confined mixture of 30 mole % $[C_2C_1Im][NTf_2]$ in $[C_{10}C_1Im][NTf_2]$. The existence of a minimum for which no maximum can be measured suggests that a maximum exists but in the region of the force profile which cannot be measured by our technique. This force maximum must occur at a lower force than maxima measured at larger separations, such that the spring instability causes the surfaces to jump together over this low maximum. Such an unmeasurable maximum is shown by the red line in figure 5.11. Similarly, minima exist close to surface contact that are at smaller force magnitudes than those further away from surface contact. This is clearly seen in the retraction made before the final large jump, shown in figure 5.11. In this case, we observe a minimum at a separation of 4.4 nm at a force of 0.22 mN m^{-1}, then at 5.4 nm and a force of -0.15 mN m^{-1}, before finally jumping from a deep minimum at 6.2 nm and a force of -0.2 mN m^{-1}. Finally, the discrepancy in the final jump suggests some curious aspects for the innermost regions of the force profile. This feature could imply that the squeeze-out transition of this final layer occurs in a stepwise manner, similar to the non-equilibrium jump-out transitions seen in pure ionic liquids (described in figure 5.8). This in turn could suggest that there are equilibrium maximum positions that are inherently unmeasurable in this technique because of the spring instability.

Similar features are seen at 10 % $[C_2C_1Im][NTf_2]$, with a close up of interesting features of the force profile shown in figure 5.12. Again we see an initial maximum in the force profile at $\approx$ 5.7 nm followed by a jump of $\approx$ 1.6 nm to a hard wall contact at a surface separation of $\approx$ 4.1 nm. Compression here eventually yields a two stage jump sim-

ilar to that seen in 30 % $[C_2C_1Im][NTf_2]$. In this case, the two stages are more clearly separate from each other, with an initial rapid jump of ≈ 0.5 nm followed by a slow jump of ≈ 0.9 nm. The total jump is ≈ 1.4 nm. Retraction from the innermost hard wall reveals a deep adhesive well, but retraction from the outer hard wall shows an initial transition of ≈ 0.3 nm before a final jump out to large separations is reached. Again, the force profile was found to be highly reproducible over an extended period of measurement. The similarities between the force profiles measured at 30 and 10 mole % $[C_2C_1Im][NTf_2]$ in $[C_{10}C_1Im][NTf_2]$ lend weight to these unusual measurements, and suggest that features in the 10 % case likely arise for similar reasons to those in the 30 % case.

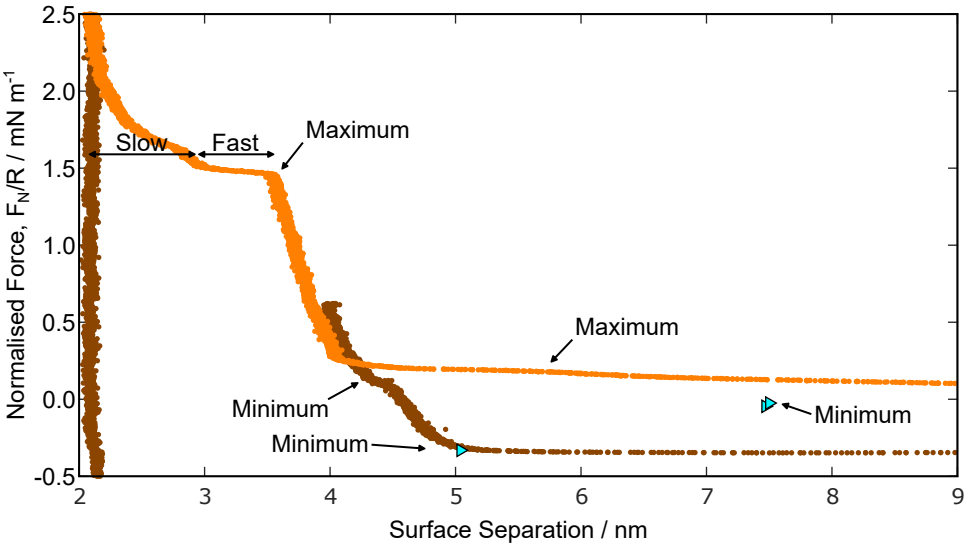


Figure 5.12: Enlarged force profile measured in 10 % $[C_2C_1Im][NTf_2]$. Forces measured on approach of the surfaces are shown in orange and those measured on retraction are shown in brown. Measured maxima and minima are highlighted. Several inner minima exist at lower adhesive force than minima observed at greater surface separations, so jumps are observed during retraction force measurements.

5.4.1 | Fitting Structural Forces

Although the forces seen at 50 mole % $[C_2C_1Im][NTf_2]$ could be considered as a simple oscillatory type picture, those profiles measured at 30 and 10 mole % $[C_2C_1Im][NTf_2]$ show clear deviations from the simple pictures of oscillations arising from either ABAB type layers or from the formation of bilayers. Instead, they show features of both forms of force profile, with small, ABAB type jumps and large, bilayer type jumps. In order to produce a simple model that can describe all the observed forces, we consider a linear combination of the fits obtained above for the pure ionic liquids. This is similar to the description of complex waveforms by the superposition of multiple simple waves. As the magnitude of the long range force is typically much lower than that of the structural force, we neglect any long range force contribution here and instead focus only on the fits of the structural forces. This gives an equation of the form

$$\frac{F_N}{R} = M\, e^{-D/\lambda_o'} \cos\left(\frac{2\pi}{\xi'}(D+m)\right) + N\, e^{-D/\lambda_o''} \cos\left(\frac{2\pi}{\xi''}(D+n)\right) \qquad (5.5)$$

where the superscript ′ refers to fixed parameters taking the values from pure $[C_2C_1Im][NTf_2]$ and ″ to fixed parameters from $[C_{10}C_1Im][NTf_2]$, as given in table 5.2. M and N are fitting parameters describing the magnitude of each oscillatory term , and m and n offsets for each oscillation. In this equation, the first term represents the total contribution to the force from $[C_2C_1Im][NTf_2]$ and the second term represents the contribution from $[C_{10}C_1Im][NTf_2]$ (note that $M/2\pi$ and $N/2\pi$ refer to energy contribution of each term). Using equation 5.5, we are able to produce fits for each mixture investigated in this study. These fits are shown in figure 5.13 and the values of M, N, m, and n are shown in

Table 5.3: Fitting parameters from equation 5.5 for forces measured in ionic liquid mixtures. Contributions to the free energy of interaction are also shown. Parameters calculated for the pure liquids from equation 3.1 are shown for comparison.

Mole % $[C_2C_1Im][NTf_2]$	M / mN m^{-1}	$M/2\pi$ / mJ m^{-2}	m / nm	N mN m^{-1}	$M/2\pi$ / mJ m^{-2}	n /nm
100	627	100	0.1	0	0	0
50	40	6.4	0.1	10	1.6	0
30	70	11	0.5	80	13	0
10	45	7.2	0.4	90	14	0.7
0	0	0	0	576	92	1.3

table 5.3.

Remarkably, the fits are able to capture many of the unusual features of the recorded force profiles, including minima at larger separations in deeper wells than those at smaller separations, and variations in the distances between hard walls. The fitting method can even succeed at describing the apparent simple decaying oscillation structure of 50 % $[C_2C_1Im][NTf_2]$ by minimising the contribution to the force from $[C_{10}C_1Im][NTf_2]$. The fits also suggest the existence of maxima that are inherently unmeasurable by the SFB owing to the spring instability, but which may be sensed during non-equilibrium regions of the measurement in a similar manner to the non-equilibrium transitions observed during the jump-outs in pure ionic liquids. Interestingly, the magnitudes of the forces in the mixed liquids are substantially lower than in the pure liquids, which could suggest that the two liquid structures are interfering with one another.

It is striking that this simple model is able to reasonably fit complex aspects of these force profiles. There are of course many imperfections in the fits, which may arise from interactions not accounted for in this model, as well as deviations away from ideal geometry (surface flatten-

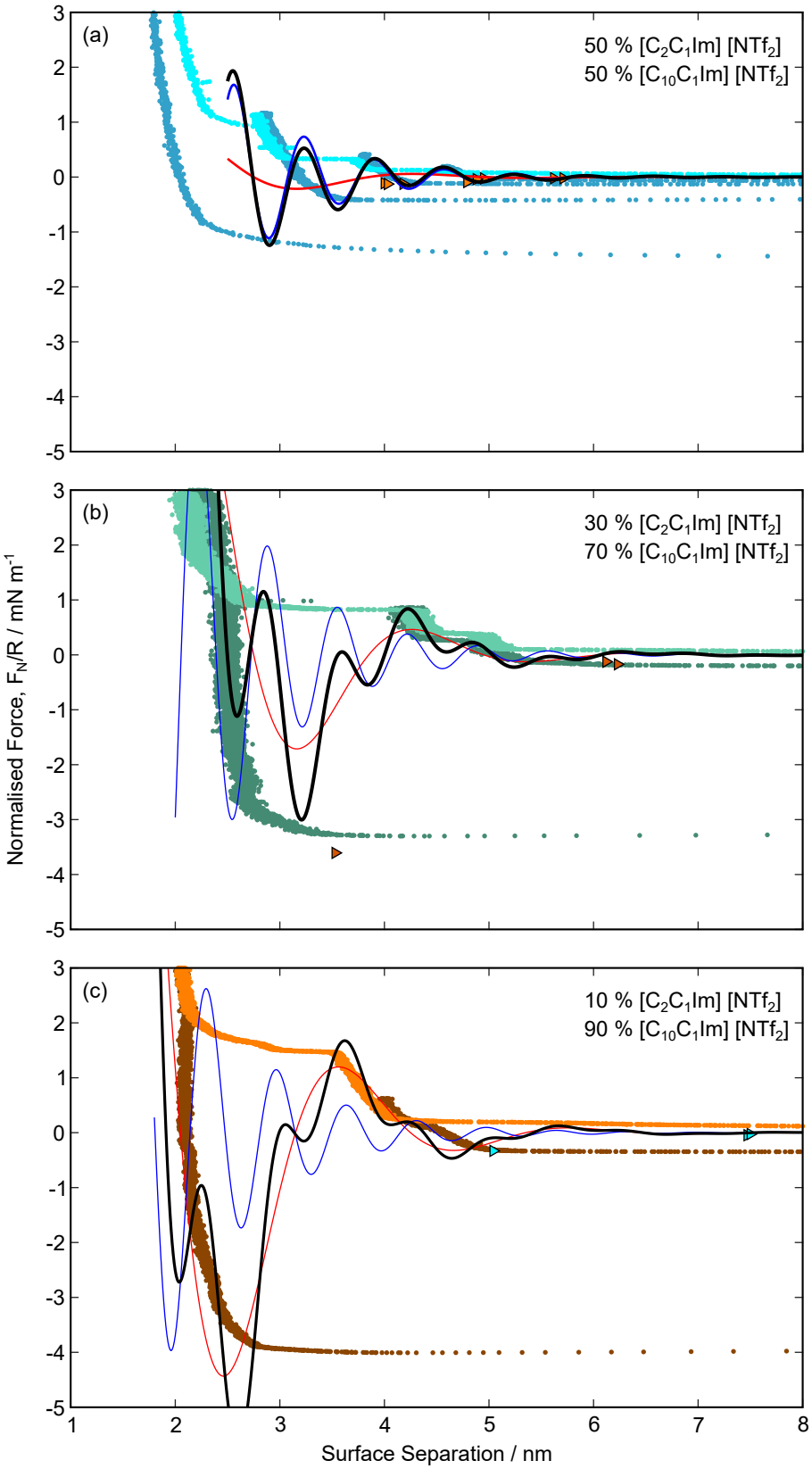


Figure 5.13: Force profiles of ionic liquid mixtures with fits as described in equation 5.5 overlaid. The total fit is shown in black, while the contribution to the total fit from $[C_2C_1Im][NTf_2]$ is shown in blue and the contribution from $[C_{10}C_1Im][NTf_2]$ is shown in red.

ing at high forces). However, it is hard to imagine a more simple model that can successfully reproduce the observed features, and the success of our model suggests that we are capturing some fundamental aspects of the liquid mixture.

It is important to consider why these fits are successful. In this ionic liquid mixture, there are three components: the $C_2C_1Im^+$ cation, the $C_{10}C_1Im^+$ cation, and the NTf_2^- anion. This gives rise to six individual interaction potentials that must combine to give the total force profile: those of the ions with themselves and those of the ions with each other species. In our simple model, which has its roots in the interaction potentials for the pure liquids, we consider five of these potentials: the anion interaction with itself, the cation anion interaction for each cation, and each of the interactions of the cations with themselves - these are captured in the contributions from the pure liquids. The only interaction missing is that between the different cations, and the inclusion of this interaction potential could result in a closer fit. As the fits appear reasonable without considering this interaction, it seems that the contribution to the total force from the cation-cation interaction is relatively low. This may imply some form of nano-scale separation between the two liquids, such that the majority of ions exist in an environment similar to that of a pure liquid, as has previously been observed in other ionic liquid mixtures[27,224].

However, it is hard to reconcile this picture with that of ordered stacks of ions giving rise to the discrete layering transitions. It is important to note that the SFB is not measuring the interaction between the surfaces and individual ions, as occurs with sharp-tip AFM measurements. Instead, owing to the relatively large area of contact between the two SFB surfaces, the SFB measures interactions across a molecu-

larly thin liquid film that contains many ions. The film behaves in a statistical manner, which may be described by the wavelengths and decays that we are able to measure with the SFB. This, as with underscreening, may be related to the work of Roland Kjellander[165], in which an electrolyte can be described by a sum of decay modes that may be monotonic or oscillatory. In the case of ionic liquid mixtures confined within the SFB, the magnitudes of multiple oscillatory decay modes remain large, and thus, complex force profiles are measurable, and may be fitted by equation 5.5. This interpretation suggests that it is always important to consider all decay modes that may be present in a liquid mixture when making measurements using statistical techniques such as the SFB, and will have important implications for the analysis of such data.

5.4.2 | Long Range and Total Forces

At each mixture concentration, we measure a long range monotonic exponential force. These forces can be fitted to the equation

$$\frac{F_N}{R} = B\ e^{-D/\lambda_s} \tag{5.6}$$

where B is the magnitude of the long range forces and λ_s is the decay length. This method is as described above for long range forces in pure ionic liquids and in chapter 3 for water-in-salt electrolytes. Examples of fits on individual runs at each concentration are shown in figure 5.14, and the mean fitted values for both force and interaction free energy magnitude, alongside the decay lengths, are shown in table 5.4.

It is clear that long range forces are present in ionic liquid mixtures, as in pure ionic liquids, and likely arise from a similar origin. The large deviations in underscreening forces from one run to the next give rise to

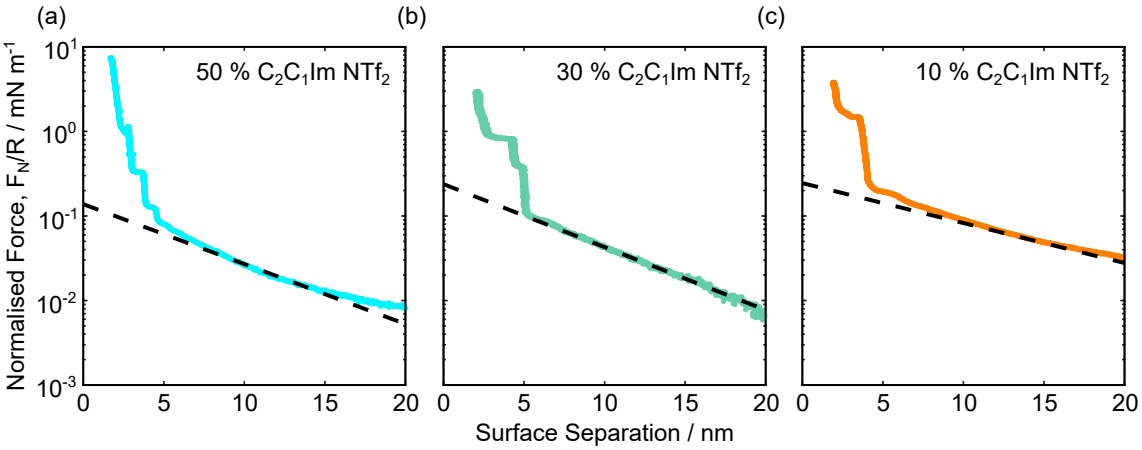


Figure 5.14: Force profiles of ionic liquid mixtures on a logarithmic force scale, with the monotonic long range exponential force shown. Exponential fits of these forces between 9 and 12 nm from surface contact are shown by the dashed black lines.

Table 5.4: Fitted parameters from the long range force in equation 5.6 for the measured range of mixture concentrations. B is also shown as an interaction free energy. Errors are taken as standard deviations from fits on multiple runs. Parameters for the pure liquids are also shown for comparison.

Mole % $[C_2C_1Im][NTf_2]$	B / mN m^{-1}	$B/2\pi$ / mJ m^{-2}	λ_s / nm
100	0.250 ± 0.069	0.040 ± 0.011	8.33 ± 2.40
50	0.159 ± 0.047	0.025 ± 0.007	6.37 ± 0.77
30	0.230 ± 0.047	0.036 ± 0.007	8.99 ± 2.07
10	0.341 ± 0.123	0.054 ± 0.020	9.87 ± 2.32
0	0.105 ± 0.042	0.017 ± 0.007	12.68 ± 2.32

the large errors shown in table 5.4. However if there is a trend present it appears that the decay length decreases to a certain value as the concentration of $[C_2C_1Im][NTf_2]$ is decreased, then increases again to the value for the pure $[C_{10}C_1Im][NTf_2]$. This is shown in figure 5.15. Considering again equation 5.2, as the concentration of $[C_{10}C_1Im][NTf_2]$ is increased, we expect the dielectric permittivity of the mixture to increase and the ion concentration to decrease, which should both contribute to a decrease in the screening length. However, we also expect an increase in the mean ion diameter a, which should lead to an increase

in the screening length. The interplay between these two effects could give rise to a minimum in the decay length of the liquid mixtures.

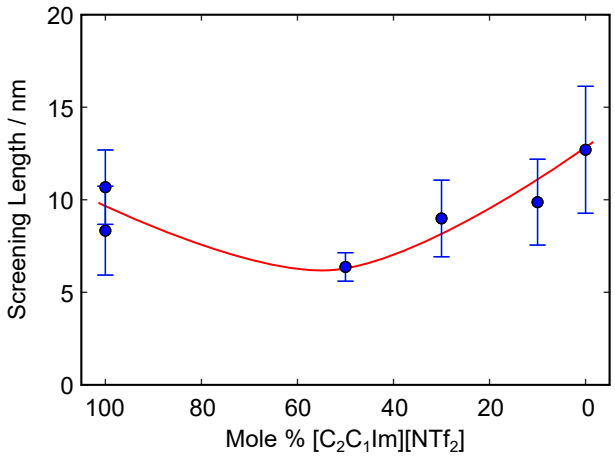


Figure 5.15: Screening lengths (blue circles) measured in pure and mixed ionic liquids as the mole % of $[C_2C_1Im][NTf_2]$ is decreased. The red line is drawn as a guide to the eye, and shows a possible trend.

In total, this means that the forces in ionic liquid mixtures can be relatively well captured by three decay modes: two decaying oscillating modes that describe the structural forces and arise from the contributions of each of the pure ionic liquids to the total force, and one monotonically decaying exponential mode that describes the long range force. This finding provides experimental evidence for the work of Roland Kjellander[165], and will be influential in further work aiming to understand the character of ionic liquid mixtures and complex electrolytes.

5.5 | Summary

In summary, we have performed high resolution surface force measurements across thin films of two structurally different ionic liquids and their mixtures. We observed near-surface structure that in the pure liquid cases could be interpreted molecularly as well defined layers of molecular ions, either in alternating anion cation ABAB layers or in

bilayers with alternating regions of charge density and charge scarcity. This was captured by fitting a wavelength that described the length scale of these layers. In ionic liquid mixtures, we observed more complex structural forces that could not be described by a simple molecular stacking argument, however we were able to fit these forces by considering a linear combination of the forces observed in the pure liquids, similar to the manner in which complex waveforms can be described by the superposition of multiple simple waves. This suggests that ionic liquid mixtures can be described by multiple oscillatory decay modes.

Further forces were found at large surface separations, similar to previous measurements in ionic liquids and other concentrated electrolyte systems. We attribute these forces to underscreening, and discuss the origin of underscreening in terms of an additional monotonic decay mode in the liquid that may arise from a reduced effective ion charge.

Overall, these observations will have implications for the design, use and application of ionic liquids and their mixtures in confined systems and at interfaces, and highlight the importance of considering all aspects of the constituents when considering the behaviour of a mixture.

6 | Guanidinium Ions at Charged Surfaces

The strong protein denaturing character of the guanidinium ion, Gdm^+, was first noticed by Jesse Greenstein in 1938 during his work at the Harvard Medical School[230]. Since this first work, aqueous guanidinium chloride (GdmCl) solutions at concentrations in excess of 1 M have been used by chemists, biochemists and biologists to aggregate and denature proteins. The structure of GdmCl is shown in figure 6.1. This chapter presents and discusses measurements of forces and structures present at charged interfaces in aqueous solutions of GdmCl and relates these results to the mechanisms of protein denaturing.

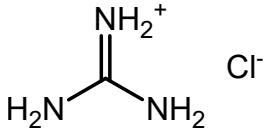


Figure 6.1: Structure of guanidinium chloride, GdmCl.

6.1 | Background and Motivation

Initial work by Franz Hofmeister and colleagues more than a century ago showed that certain ion combinations were more effective at precipitating proteins than others[29,231]. They began ordering these ions into a series, and today this series has become known as the Hofmeister series. Many additional ions, including guanidinium, have been added to the series since the work of Hofmeister, and the series has been found to be relevant to various phenomena, including biological processes[232–235], surface tensions[236,237], critical micelle concentrations[236,238], polymer stabilities,[239,240] and even water retention in wool[241]. The

Hofmeister series for some common ions is shown in figure 6.2. In the past more than 130 years of study, substantial effort has been devoted to uncovering the ordering of the series. However, despite a rich history of study and broad applicability across chemistry, biochemistry and biology, a complete understanding of the origins of the Hofmeister series is yet to be reached[30,234,242–245].

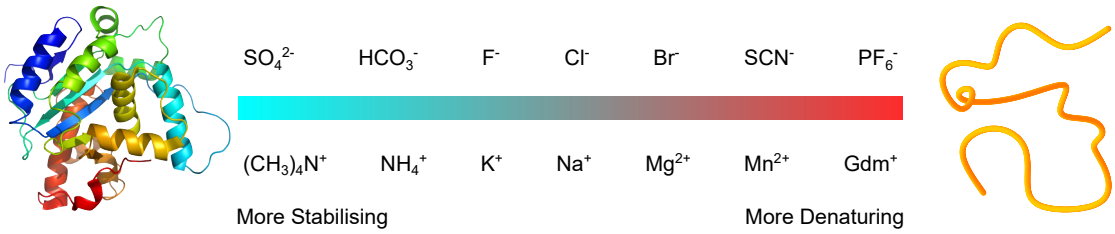


Figure 6.2: Various cations and anions, including guanidinium (Gdm^+), as found in the Hofmeister series. Those with more stabilising effects for proteins are shown to the left alongside a protein folded into its tertiary structure, while those with greater denaturing effects are shown to the right, alongside an unfolded protein. The protein structure is under a creative commons licence and created by Debstar[246].

6.1.1 | The Guanidinium Ion and Guanidinium Chloride

Guanidinium is a trigonal planar molecular cation consisting of a central carbon atom surrounded by three NH_2 groups[247]. The guanidinium group appears in nature, most notably in the amino acid L-arginine, which is found in all protein containing foods. The carbon atom of the guanidinium ion is sp^2 hybridised, which allows overlap of the remaining carbon p orbital with the nitrogen lone pairs. As a result, the positive charge is delocalised across both faces of the ion in an electron poor π system. At the equator, the three NH_2 groups provide six possible hydrogen bond donor sites, however the nitrogen atoms are unable to act as hydrogen bond acceptors owing to the delocalisation of their lone-pair electrons. The dimensions of the guanidinium ion and the structure of L-arginine are shown in figure 6.3.

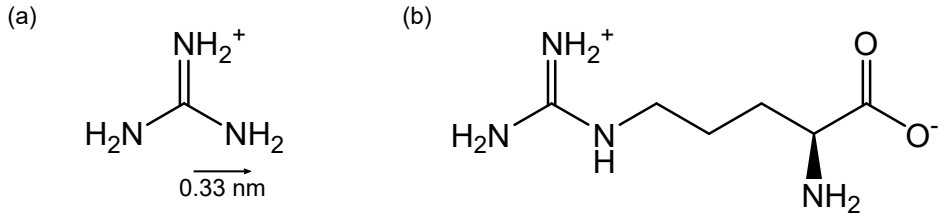


Figure 6.3: Structure and dimensions of the guanidinium cation and L-arginine. (a) The guanidinium cation may be thought of as a disk with radius 0.33 nm, calculated from crystallographic data[248]. (b) Structure of L-arginine, a naturally occurring amino acid containing a guanidinium group.

Despite the prevalence of hydrogen bond donor sites, the guanidinium ion is relatively poorly solvated in water. Steric interactions mean not all amine hydrogens may donate hydrogen bonds at once, and the ion has been shown to be rather weakly hydrated at the equator in water, without a well defined hydration shell[247]. The delocalisation of the positive charge across the faces of the ion mean these regions are not charge dense, and behave hydrophobically, also without significant water solvation[249]. Indeed, the ion is thought to dissolve in water without causing significant change to the structure and dynamics of water[247,250]. This gives rise to measurable effects: the activity coefficient of guanidinium salts decrease continuously to saturation concentrations, whereas for the majority of common salts, activities are found to rise again beyond a certain concentration[251,252], as shown in figure 6.4. The activity coefficient tracks non-ideality in solute behaviour, including ion correlations, excluded volume, and solvation effects, but as the solvation and excluded volume behaviour of the Gdm^+ ion is so different to other common salts, so too is the activity coefficient.

This poor solvation has been suggested to lead to the formation of like-charged ion pairs, trimers and higher n-mers via face-to-face stacking. Such behaviour has been shown in experimental and computational studies[249,253–256], and examples of these n-mers taken from snapshots of molecular dynamics simulations are shown in figure 6.5.

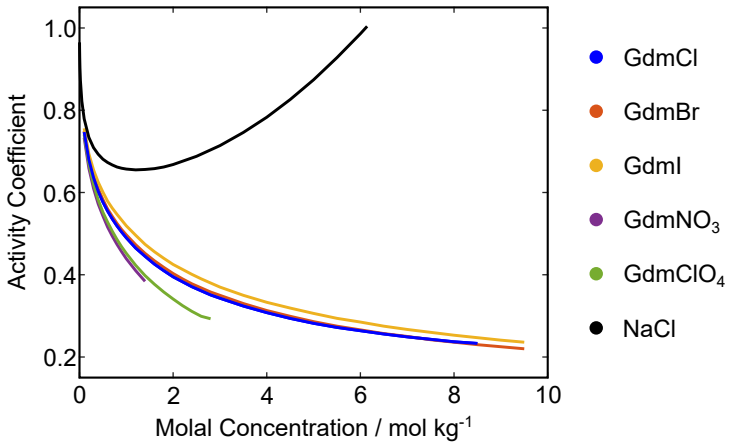


Figure 6.4: Activity coefficients of aqueous guanidinium salts and sodium chloride. The activity of guanidinium salts decreases to the saturation concentration, whereas sodium chloride shows a minimum in the activity coefficient at around 1 m. Data taken from works by Bonner[251] and Hamer *et al*[252].

Stacks between guanidinium groups in arginine amino acids can even contribute to protein function and shape[254,257]. It has also been suggested that extended ion clusters are present in guanidinium chloride, but this finding remains controversial[249,250]. Spatial density functions showing the Gdm^+ solvation environment, alongside clustering snapshots, as calculated from molecular dynamics simulations in the literature[249], are shown in figure 6.5.

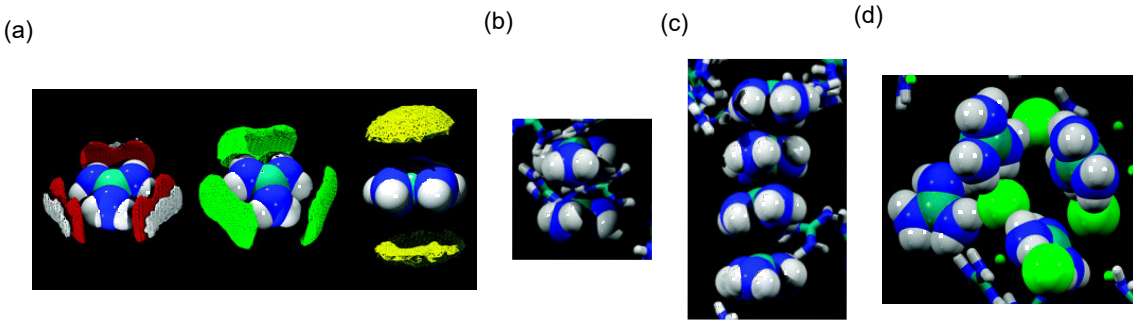


Figure 6.5: Spatial distribution functions and ion aggregates found in molecular dynamics simulations matched to neutron scattering data in aqueous GdmCl at 3 mol kg^{-1}, reproduced from a work by Mason *et al*[249]. (a) Density maps about the guanidinium ion with (i) water (oxygen in red, hydrogen in white, all at 3.7 times the average number density), (ii) carbon (4 times the average number density), and (iii) chlorine (6.8 times the average number density). (b)-(d) Molecular dynamics snapshots showing (b) Gdm dimers, (c) tetramers, and (d) extended ion aggregates between Gdm^+ and Cl^- ions.

Salts based on the guanidinium ion are routinely used in the field of biochemistry to denature, or unfold, proteins[258–260]. Most commonly, these are guanidinium thiocyanate, GdmSCN, and guanidinium chloride, GdmCl. As the SCN^- anion is itself poorly understood in its interactions with proteins, here we investigate GdmCl in order to isolate the effects of the guanidinium cation.

6.1.2 | Behaviour of Guanidinium Chloride

The unique geometry and hydration behaviour of the guanidinium ion leads to many interesting properties of guanidinium chloride solutions, including the ability of the ion to denature proteins. In cells, proteins typically fold into a structure with a hydrophilic, negatively charged exterior surrounding an internal hydrophobic core. It is the interplay between the hydrophilic and hydrophobic areas of the amino acid chain that allows the protein to fold into its active shape. The guanidinium ion, with the hydrogen bonding equator and hydrophobic faces, is thought to be able to disrupt protein structure at both the exterior and the interior, leading to unfolding.

In order to quantify these effects, research has investigated how the solubility of systems is affected in the presence of guanidinium chloride. GdmCl solutions have been shown to reduce the hydrophobic interactions between small hydrophobic molecules such as methane, and to favour the transference of larger alkanes from pure water environments to those containing GdmCl[261,262]. This disfavouring of hydrophobic interactions has been shown to lead to unfolding of model hydrophobic polymers[262] and prevents the onset of dewetting between parallel hydrophobic plates[263], suggesting a mechanism for the unfolding of the internal protein structure. The extended π electron cloud that sits over

the faces of the guanidinium ion also allows for interactions between Gdm^+ and aromatic molecules and groups. GdmCl has been shown to increase the solubility of benzene, and to interact favourably with planar aromatic residues within polypeptides[264,265]. Some of these solubility effects are shown in figure 6.6.

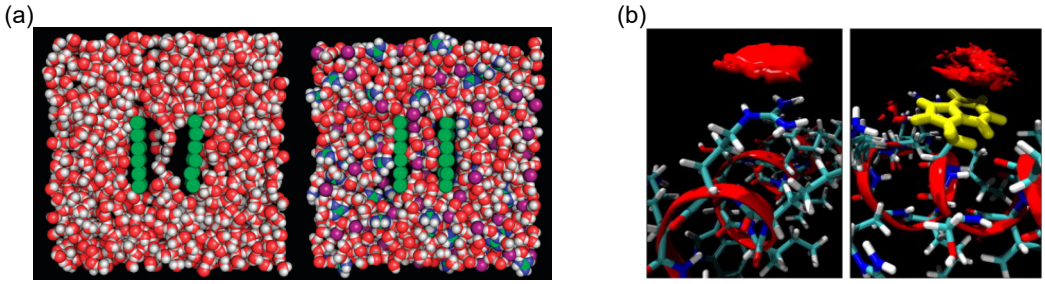


Figure 6.6: Snapshots from simulations investigating the solubility of hydrophobic and aromatic regions of molecules in GdmCl. (a) Cavitation between parallel hydrophobic plates is inhibited in the presence of GdmCl. (b) Spatial distribution functions of Gdm^+ around arginine (guanidinium containing, analogous to ion stacks) and tryptophan (aromatic) residues in a model polypeptide. Data reproduced from works by England *et al*[263]. and Mason *et al*[265].

The studies discussed above focus on the hydrophobic and aromatic interactions of GdmCl, but considering the behaviour of GdmCl in hydrophilic environments is also vital in the denaturing mechanism, as such environments form the exterior of proteins and contribute to protein form and function. The role of guanidinium ions in these regions is less clear[266], and additional work will be needed to fully understand how GdmCl effects the interactions in these hydrophilic environments. The surface force balance represents a system in which the effect of GdmCl on hydrophilic environments may be probed. Once immersed in aqueous electrolytes, the potassium ions on the mica surfaces dissolve, leaving a negatively charged, hydrophilic surface, similar to the protein exterior. Thus, the SFB can be used as a very minimal model to infer how guanidinium ions behave at protein surfaces, and the modification of forces within the SFB is related to the modifications of interactions

between proteins and between hydrophilic residues.

6.2 | Experimental Details

We investigated the surface forces present in aqueous GdmCl over a broad concentration range using the SFB as described in chapter 2. Due to the low viscosity and high vapour pressure of GdmCl solutions at concentrations 1 - 6 mol kg^{-1}, external vibrations and evaporative cooling effects were found to cause significant drifts in the surface separations. Therefore, the majority of force profiles shown here were recorded at at greater speeds than those shown in chapters 3 and 5, and were collected using the fine motor, rather than the piezo. The force profiles were collected using approach and retraction velocities of 1.0 - 20 nm s^{-1}. Here, details specific to these measurements are discussed.

6.2.1 | Materials and Solution Preparation

Solutions of aqueous GdmCl were prepared from freshly opened bottles (Sigma-Aldrich, > 99%) in ultrapure water (Millipore, 18.2 MΩ cm, TOC < 3 ppb). Preparation took place in an LFH using acid-cleaned tools and glassware to minimise contamination as described in chapter 2.

Measurements were made over a broad range of concentrations, from 1 to 6 m (molal, moles of salt per kilogram of solvent). These concentrations were chosen to span those relevant to common denaturing solutions, which are typically at around 3 m. A comparison of concentration units is shown in table 6.1. Whilst these aqueous ion concentrations are lower than those studied in chapters 3 and 4, they remain substantially higher than those for which the behaviour of electrolytes is well understood.

Table 6.1: Concentrations of aqueous GdmCl studied in this work on different concentration scales

Molal Concentration, m / mol kg^{-1}	Molar Concentration, M / mol dm^{-3}	GdmCl mole fraction	H_2O/Gdm molar ratio
1	1.1	0.017	55.5
3	2.5	0.051	18.5
6	4.2	0.098	9.25

6.2.2 | Refractive Indices

Refractive indices for guanidinium chloride solutions were measured as described in chapter 2. The results are shown in figure 6.7, and show excellent agreement with literature measurements[267], validating this technique as used throughout this thesis. For each measurement made, the refractive index is recorded and used for that data set.

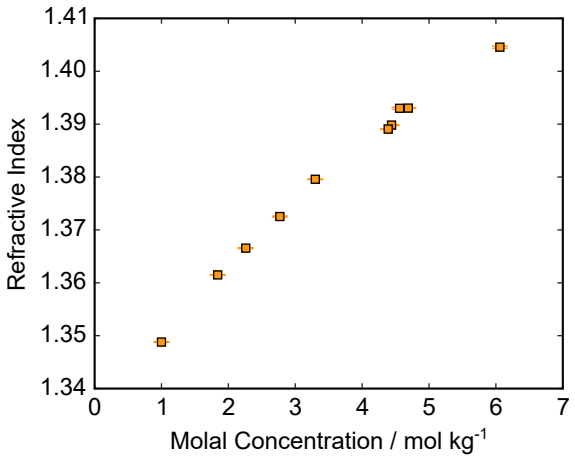


Figure 6.7: Refractive index of guanidinium chloride solution against concentration. Error bars are shown, and are typically ≈ 0.0001.

6.3 | Surface Force Measurements and Discussion

Examples of normal forces recorded at three concentrations in aqueous GdmCl are shown in figure 6.8 for small surface separations. Forces are normalised by the radius of curvature of the measurement spot such

that the recorded forces are independent of the precise surface geometry (see equation 2.1), and forces are distinguished by whether they are measured during an approach of the surfaces or during a retraction.

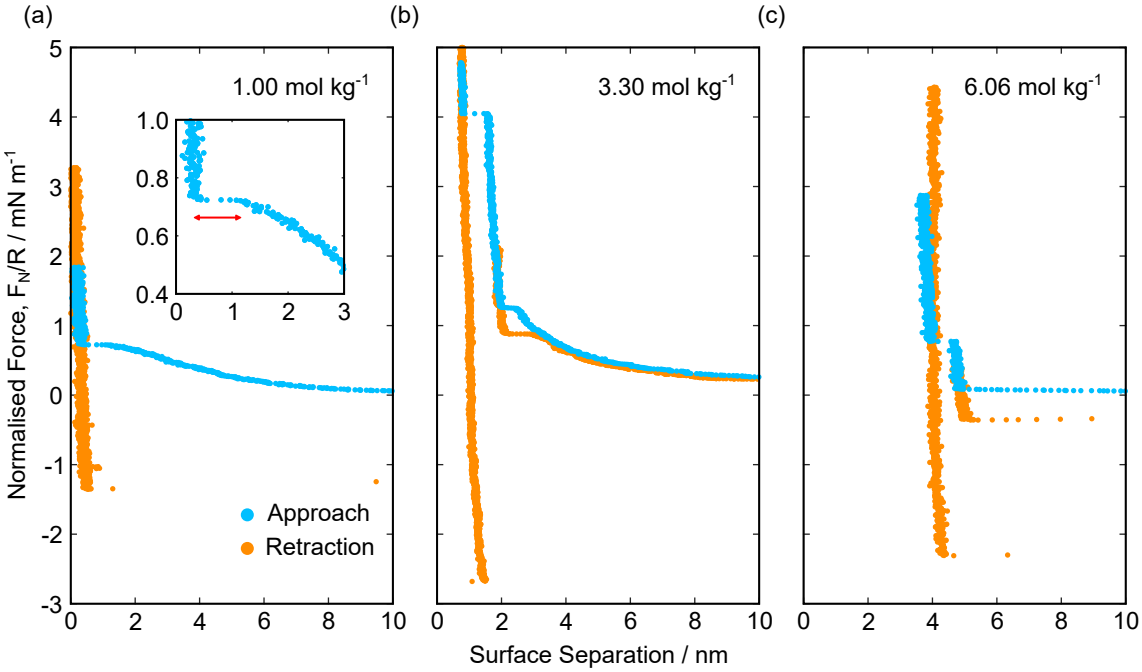


Figure 6.8: Force profiles of increasing concentrations of aqueous solutions of GdmCl. Forces are normalised by the radius of curvature of the lenses at the measurement spot. Forces measured on approach of the SFB surfaces are shown in blue while those measured on retraction are shown in orange. The exact concentrations of each system is shown - (a): 1.00 m, (b): 3.30 m, (c): 6.06 m. In (a), a long range repulsive force is seen, followed by a jump into adhesive contact as highlighted in the inset. In (b), a long range repulsive force followed by a jump is again seen. Further compression results in layering transitions. In (c), the magnitude of any long range force is greatly reduced, and only layering transitions are seen.

We see a transition in the forms of the forces measured as the concentration is increased. At the lowest concentration measured we see a long range repulsive force with a large magnitude extending several nanometres away from the surface, followed by a sudden jump of the surfaces into close adhesive contact. As the concentration is increased, this long range repulsive force is maintained, but further compression after the initial jump results in a further jump, similar to the layering transitions discussed for the water-in-salt electrolyte in chapter 3 and

the pure ionic liquids in chapter 5. At the highest concentration investigated, a simple oscillatory force profile is observed with a long range force whose magnitude is much reduced. An incompressible region close to the surfaces also builds up as the surface separation is increased: at the lowest concentration studied, the surfaces reach near mica-mica contact, but at the highest concentration, the surfaces approach only to separations of ≈ 4 nm.

This observed range of behaviours is curious, and suggests interactions of guanidinium chloride with charged surfaces is highly dependent on the ion concentration. In the following sections, the forces observed at each concentration will be discussed individually, with possible interpretations proposed for the observed features and the implications these suggestions have for the general character of GdmCl solutions and their effects on proteins.

6.3.1 | 1-2 molal GdmCl

At the lowest concentrations investigated, we see a long range repulsive force extending several tens of nanometres from the surfaces. As the surfaces approach, the magnitude of this force increases, eventually reaching a maximum. The spring instability then causes the surfaces to jump together. At the 1.00 m concentration shown in figure 6.8 (a), the jump is typically ≈ 0.8 nm, and the surfaces jump to a separation of ≈ 0.3 nm. No further maxima are observed in the force profile on continuing to push the surfaces together. Retracting the surfaces from this hard wall contact reveals an adhesive well. This form of force profile is very reproducible, and could be measured at GdmCl concentrations between 1 and 2 m in multiple experiments.

Although very qualitatively reproducible, we find large quantitat-

ive variation between runs even within the same measurement, which leads to substantial margins of uncertainty when carrying out a quantitative analysis. The apparent decay length of the long range force is highly variable, as is the magnitude of the repulsive force. The form of the repulsive force also shows two behaviours: forces may either appear convex, as would be expected in a charge regulation model[61], or concave, similar to the layering transitions seen in chapters 3 and 5. Some behaviours also show a clear time dependence: initial measurements see no maximum or jump-in, while adhesive forces are seen to develop systematically throughout the measurement. These differences are highlighted in figure 6.9 for a single set of measurements at 1.00 m.

Previous measurements with the SFB have observed long time scales as the system relaxes to equilibrium. Measurements between mica surfaces in pure water have shown that the surface charge can develop over the course of 1-2 hours as a result of ion dissolution and readsorbtion[268], whilst recent measurements on ionic liquids have shown similar timescales before a steady state is reached[157]. In the present experiments at 1-2 m GdmCl, we find that no steady state is reached over $\sim$ 8 hours of measurement time, indicating even slower evolution towards equilibrium than previously observed. During this time, the magnitude and range of the long-range part of the measured interactions fluctuate substantially and non-linearly.

In order to quantify these variations, we attempt to fit the force profiles to a charge regulation type equation of the form

$$\frac{F_N}{R} = -\frac{A}{6D^2} + \frac{Be^{-D/\lambda_s}}{1+(1-2p)e^{-D/\lambda_s}} \tag{6.1}$$

where A is the mica-electrolyte-mica Hamaker constant, B is the mag-

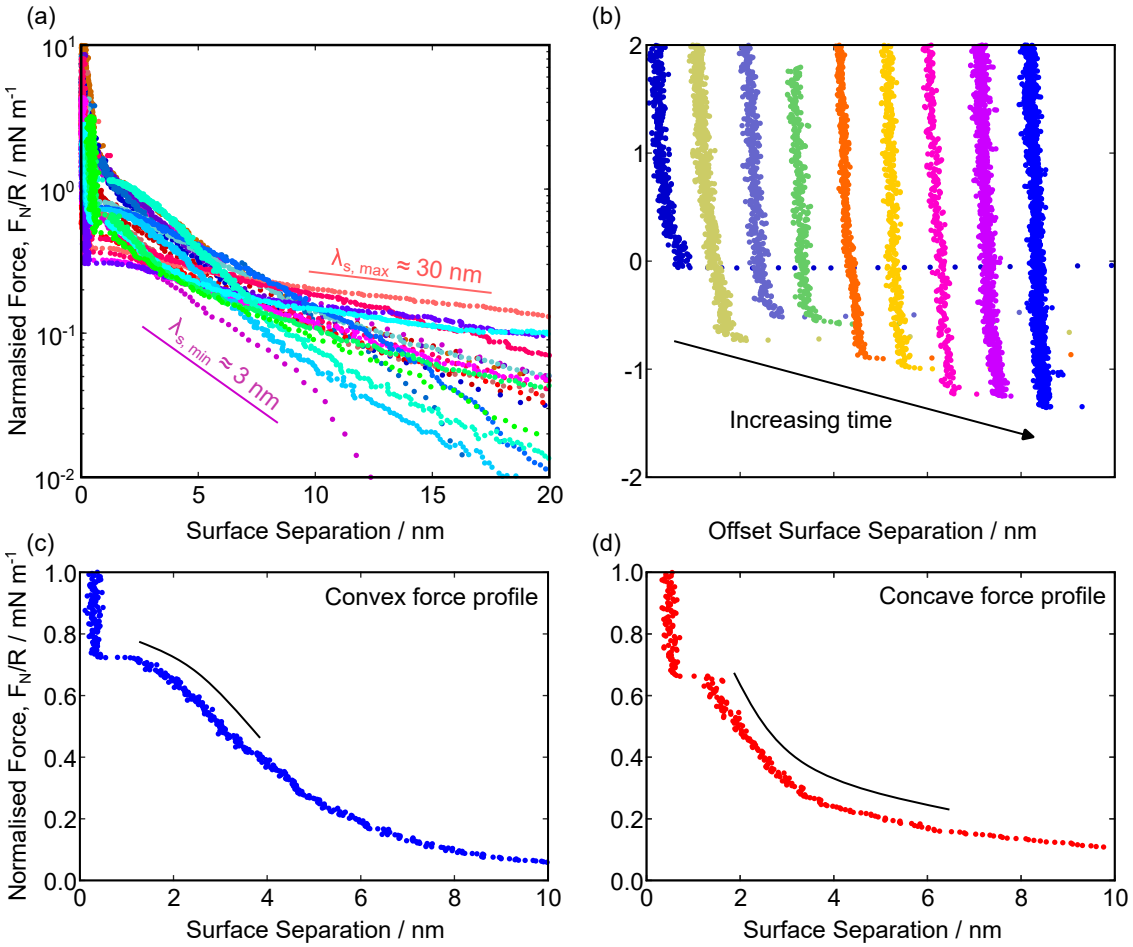


Figure 6.9: Variability in the measurements of 1.00 m GdmCl aqueous solution. (a): Variations seen in approach runs, plotted on a logarithmic force scale. Different approach runs are shown in different colours. The decay of the long range force at large surface separations and the maximum of the force before the jump in show high variability. (b): Variations seen on retraction. Retractions are offset from each other and ordered left to right by time since the start of the experiment. There is a clear increase in the magnitude of the adhesive force as the experiment goes on. (c): Some force profiles show a convex form at small separations, similar to a charge regulation model. (d): Some force profiles show a concave form at small separations, similar to the approaches seen in WiS electrolytes and ionic liquids.

nitude of the long range part of the force, λ_s is the screening length, and p is a dimensionless charge regulation parameter ranging from $p = 0$, at constant potential, to $p = 1$, at constant charge. We estimate the value of A to be 20×10^{-20} J from the refractive index (our measurement) and the dielectric constant of the electrolyte at 1.00 m using dielectric data from Hunger *et al*[6,250]. An example fit is shown in figure 6.10.

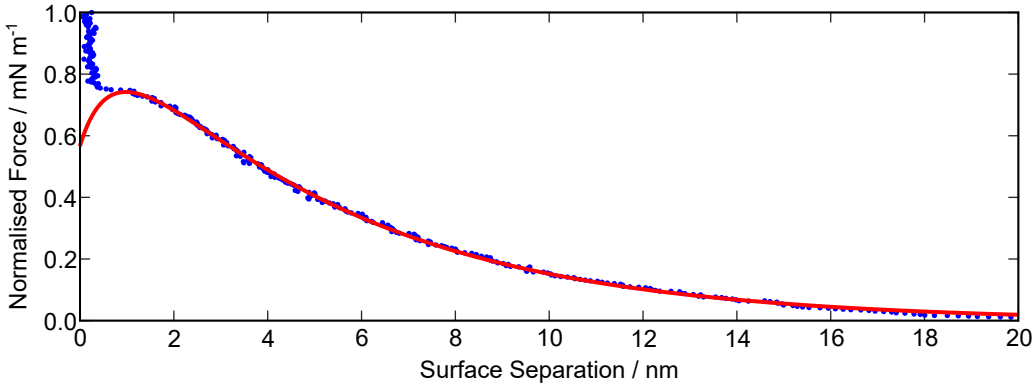


Figure 6.10: Data of a single convex force measurement on 1.00 m GdmCl with a fit according to equation 6.1 overlaid in red. In this case, B = 1.64 mN m^{-1}, λ_s = 5.29 nm, and p = 0.644, indicating charge regulation behaviour. Note that D_0 is set at -2 nm to ensure a good fit for the attractive part of equation 6.1.

This form of equation is able to well fit the convex type force profiles as shown in figure 6.9 (c) but struggles to fit the concave type force profiles shown in figure 6.9 (d). We report here only those values for which the fit is successful, but note that this spread encompasses the magnitudes and decay lengths of the concave force profiles. We find that B ranges from 0.11 to 3.3 mN m^{-1}, with a mean value of 0.78 ± 0.98 mN m^{-1}, while λ_s ranges from 2.9 to 31 nm, with a mean value of 14 ± 9.6 nm. These fitted parameters do not appear to vary with either approach velocity or time over the course of this measurement. However the variation could be due to consistently fluctuating surface and near-surface properties as the system evolves. These fluctuations could also give rise to the varying convex or concave behaviours.

6.3.2 | 2-4.5 molal GdmCl

As the concentration of aqueous GdmCl is increased, additional behaviours begin to emerge. We again see a long range repulsive force extending several tens of nanometres from the surfaces. As the surfaces

approach, the magnitude of this force increases, eventually reaching a maximum, followed by a jump of the surfaces together. At the 3.30 m concentration shown in figure 6.8, the initial jump into contact is typically ≈ 0.5 nm, and the surfaces jump to a separation of ≈ 1.9 nm. Further compression of the surfaces gives rise to a layering transition, similar to previously described structural forces in chapters 3 and 5, as well as in the literature[24,62,67,148]. The inner transition is typically ≈ 0.8 nm, and the surfaces jump to a separation of ≈ 0.8 nm. No further transitions could be observed on applying additional force. On retraction from the initial hard wall, we see a jump out into the repulsive region of the force profile that overlays well with the measured approach force. This indicates that the long range force is a thermodynamically reversible phenomenon, and does not arise from viscous effects. Retracting from the inner hard wall, we see an adhesive force that leads to a jump to large surface separations.

Again, we see high variability in the measurements. Surface structure as shown in figure 6.8 only emerges after ∼ 1-2 hours of measurement time. We also again see the systematic development of adhesion over the course of the measurement, with the inner layer becoming deeply adhesive over the course of several hours. We also note high variability in the magnitude and decay length of the observed long range force. Such observations are similar to the measurements made at lower concentrations as shown in figure 6.9, and reinforce the idea of long time scale effects present at charged surfaces in GdmCl solutions.

In order to quantify the variation of the long range force, we attempt to fit the long range region of the measured forces. Here we use a simple decaying exponential function, $F/R = Be^{-D/\lambda_s}$, as the shape of the force profiles measured at this concentration prior to the initial

jump into contact is convex rather than concave. This fitting process is similar to that used in chapters 3 and 5, and is shown in figure 6.11. We find the magnitude of the long range force to range from 0.41 to 0.85 mN m^{-1} with a mean value of 0.64 ± 0.18 mN m^{-1}, while the decay length of the long range force ranges from 4.8 to 18 nm with a mean value of 9.4 ± 4.8 nm. These parameters are similar to the magnitudes and decay lengths of the long range force found at the lower concentration, with a similar range of values also not clearly varying with time. This again suggests a consistently fluctuating surface and near surface liquid structure as the system evolves, and the similarities in the values and ranges of long range force magnitudes and decay lengths suggest similar effects are responsible here as in the lower concentrations.

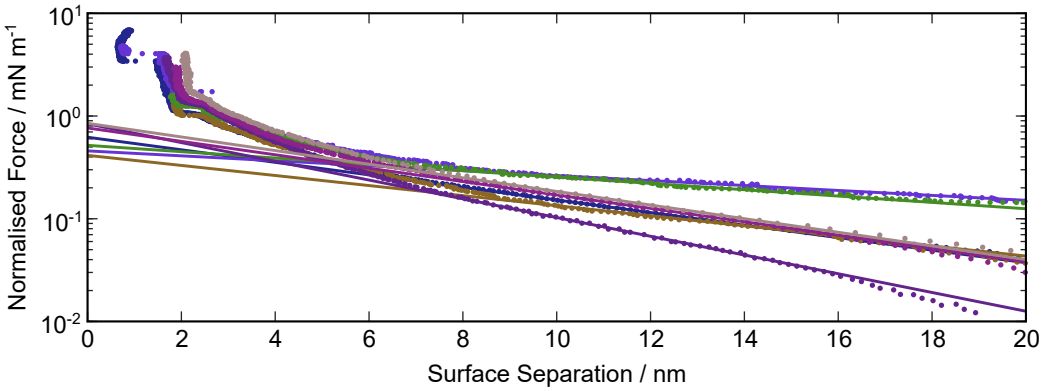


Figure 6.11: Exponential fits (solid lines) of the form $F/R = Be^{-D/\lambda_s}$ on measurement runs in 3.30 m GdmCl. The magnitude B was found to be 0.64 ± 0.18 mN m^{-1}, and the decay length λ_s was found to be 9.4 ± 4.8 nm.

6.3.3 | 6 molal GdmCl

At the highest concentration of GdmCl investigated, we again see changes in behaviour. In the 6.06 m measurement shown in figure 6.8 (c), the magnitude of the long range repulsive force appears much reduced, and the initial peak before the jump into contact appears at a much reduced force, though at larger surface separation. The initial jump into

contact is typically ≈ 0.5 nm to a surface separation of 4.5 nm. Further compression yields an inner transition of ≈ 0.7 nm. These transitions are similar in dimensions to those observed at 3.30 m, which suggests a common structure is squeezed out in each case. The final surface separation is 3.7 nm, much greater than that observed at the lower concentrations studied. Retraction from either hard wall yields a deep adhesive well. This form of force profile is much more similar to those discussed for the water-in-salt electrolytes in chapter 3 or the pure ionic liquids in chapter 5, and takes the form of a decaying oscillatory force profile.

Unlike at the lower concentrations, the forces observed at 6 m GdmCl appear to be in a steady state: no time dependence is seen over the course of the measurement, and far more consistent long range forces are observed. We again fit the measured long range force of each run to a decaying exponential function, as shown in figure 6.12. We find a magnitude B of the long range force to be 0.19 ± 0.07 mN m^{-1} with a decay length of 13.1 ± 3.4 nm.

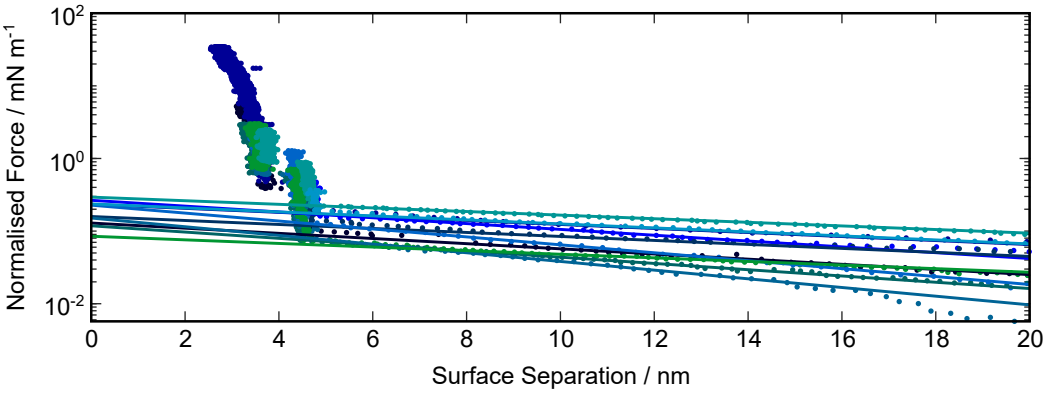


Figure 6.12: Exponential fits (solid lines) of the form $F/R = Be^{-D/\lambda_s}$ on measurement runs in 6.06 m GdmCl. The magnitude B was found to be 0.19 ± 0.07 mN m^{-1}, and the decay length λ_s was found to be 13.1 ± 3.4 nm.

6.3.4 | Interpretation of Forces

Over the range of concentrations studied, we see some clear differences in behaviour, with large variability between experimental runs within measurements and clear evolution in adhesive forces over long timescales. This points to fluctuating and slowly developing surface conditions with steady states not reached over the course of an entire measurement. However, we also observe clear trends and similarities between systems as the concentration is increased. At each concentration we observe a long range repulsive force, with a decay length of $\sim$ 10 nm. Once close to contact, we observe maxima, with additional structural force-like features emerging with increasing concentration and over time at the lower concentrations studied. The surface separation at which we see these maxima increases as the concentration is increased. Retracting from the closest contact yields an adhesive force that emerges over time.

Taken together, these observations imply a concentration and time dependent evolution of the surface character. In aqueous electrolytes, mica is expected to carry a negative charge, as potassium ions dissolve away from the surface. This should attract an electric double layer type structure of positively charged guanidinium ions. However, the solvation structure of the guanidinium ion is very different from those of more simple cations because of the shape and distribution of charge within the molecular ion. We suggest that this unique solvation and charge structure of Gdm^+ inhibits a rapid irreversible adsorption of the cations to the surface and instead they associate reversibly over a long timescale. A slow build up of cations at the surface will also cause anions to build up in a similarly slow and reversible manner. This leads to a fluctuating effective mica surface charge, σ_{eff}, which gives rise to

the observed differences in the force maximum that must be overcome in order to reach contact. Such slow dynamics could explain why previously it has been unclear how GdmCl solutions affect the solvation of hydrophilic groups in proteins and lead to denaturing[266], as simulations and models do not study large enough timescales to resolve this behaviour.

As the concentration is increased, adsorption to the mica surface requires desolvation from an increasingly ion rich environment. The process of adsorption therefore becomes more favourable and more rapid. Thus, a substantial region of ions builds up at the surface, causing the minimum surface separation to increase as the concentration is increased. Both at high concentrations and on long time scales, we expect a low σ_{eff}, as cations are adsorbed to counter the negative charge on the mica. These ideas are shown in figure 6.13. This large accumulation of ions at charge rich sites provides insight in the denaturing mechanisms: as this ion layer builds up, the interactions governed by such sites are dramatically altered, so the balance of forces that maintain the protein shape are disrupted, causing the protein to unravel.

The initial slow dynamics of guanidinium ion adsorption to the sur-

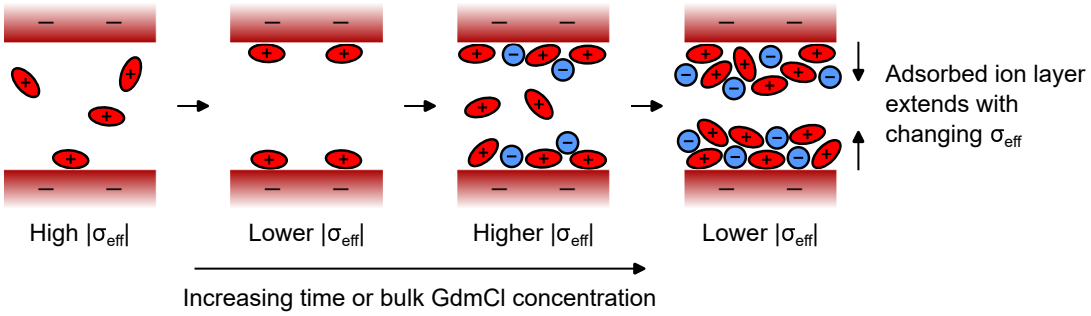


Figure 6.13: Cartoon showing a possible explanation for the origins of the high variability of the surface interaction and increasing minimum surface contact separation in thin films of aqueous GdmCl solutions. At low concentrations, initial ion adsorption to the surfaces occurs over a long timescale, leading to a fluctuating σ_{eff}. At high concentrations or long time scales, an adsorbed ion layer is built up and a steady state with low σ_{eff} is reached.

face could also be responsible for the time dependence of the adhesive forces. A very reversibly bound surface ion layer may allow easy and rapid exchange of water and ions between the surfaces and the bulk solution. On retracting the surfaces, this film can easily expand to fill the gap, and hence no adhesion is observed. As more ions become strongly adsorbed to the surface, this rapid exchange process is interrupted. Retracting the surfaces must now initially create a vacuum, which is strongly disfavoured and so a large adhesive force is observed.

The existence of a long range force in these systems is a surprising observation. The range of concentrations studied is far too high to expect any significant effect from classical Debye-Hückel screening[7], while the underscreening forces seen in previous high concentration surface force measurements, as described in this work and elsewhere[60,62,71,153–159], are expected to be very short ranged for all except the highest concentrations studied here. It has previously been noted that solutions of GdmCl may be able to form aggregates containing many ions[249,253–256]. One possibility for the origin of the long range force could be that there are actually very few free ions confined between the slit, with the majority of ions contained within large, neutral aggregates. The free ions, at a much lower effective concentration, could then be responsible for the long range force in a Debye-Hückel type screening mechanism. We observe decay lengths on the order of 10 nm, which corresponds to a 1:1 electrolyte concentration of $\sim 1 \times 10^{-3}$ mol kg^{-1}. In order to reach such an effective concentration, $>$ 99 % of the ions present in our system would need to be bound in neutral aggregates. Such extensive pairing of ions is unlikely as ion aggregates in GdmCl are difficult to detect and remain controversial[250], however it is possible that these aggregates are more favoured when

confined to nanometric films.

A second plausible explanation for the origin of this long range force again uses aggregates, however on a much smaller scale. In this interpretation, the decay lengths we observe arise primarily from underscreening. The origins of this force remain unclear, but have been discussed in chapters 3 and 5. In the current case of aqueous GdmCl, we suggest that small scale aggregates comprising a small fraction of the total ions dissolved in the liquid can act to enhance repulsive forces in the underscreening regime by hindering surface approach, and hence observable, and similar, decay lengths are observed at all concentrations. These aggregates could be very variable, with many possible permutations, which could give rise to the high variability in the decay lengths at lower concentrations. As the concentration is increased, the aggregates become more continuous and the role of underscreening becomes greater, so the variability in the decay length decreases as we have observed. This idea is shown in figure 6.14.

Finally, we discuss the origins of the maxima in the force profiles. At

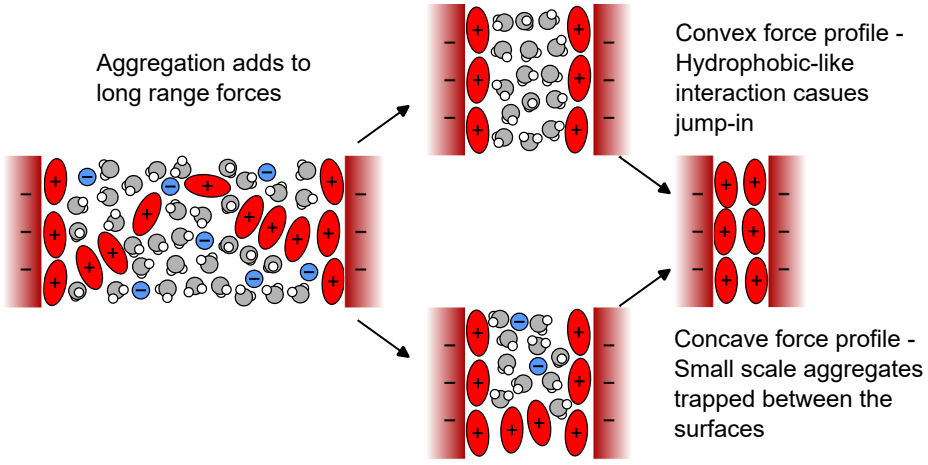


Figure 6.14: Cartoon showing a possible explanation for the origins of the long range force and the variations in force profile shape seen at low concentrations. At large separations, aggregates allow surfaces to repel each other over larger than expected distances. Close to contact, either a hydrophobic-like interaction between guanidinium ion faces (convex) or small scale aggregates (concave) can cause a jump-in.

the lowest concentrations investigated, we see competing behaviour between convex and concave force profiles. Again, the difference in these could be explained by the presence of aggregates in the liquid. The majority of large aggregates will be squeezed out as the surfaces approach, possibly giving rise to the long range force as discussed above. The convex force profiles show a similar shape to that measured in an approach characterised by DLVO forces, in which the slope of the repulsive force is much reduced compared to those seen in oscillatory force profiles. Thus, we do not suggest that this jump in is caused by the sudden squeeze out of an ion layer.

This force could arise from DLVO-like forces, with a long range force arising from underscreening and aggregate compression as discussed above, followed by a jump in to contact from Van der Waals forces. However, previous SFB measurements of simple salts at similar concentrations have revealed structural layering forces arising from hydrated ion layers, rather than the observed jump behaviour[57,59]. Instead we suggest that the jump could arise in a similar manner to the interaction that forms guanidinium ion stacks. Positively charged guanidinium ions could initially assemble with one face against the mica and the other pointing out into the gap between the surfaces. As the surfaces approach, the π electron clouds overlap, giving rise to a short range attractive force that causes the convex form of the force profile. However, if enough small scale aggregates remain between the surfaces, these could prevent the hydrophobic-like jump into contact and instead form a transient layer, giving rise to a layering like transition as described by the concave form of force profile, as shown in figure 6.14. As the concentration is increased or over long time scales, this face down Gdm^+ layer is covered with additional well defined layers of cations

and anions. These ion layers can be squeezed out in layering transitions as seen at 3.30 m and 6.06 m in figure 6.8. The layers have dimensions of ~ 0.8 nm. This could correspond to the diameter of a Gdm^+ ion (≈ 0.7 nm)[248], or the diameter of a hydrated chloride ion (≈ 0.7 nm)[269]. We therefore suggest that the ordered ion layers we observe correspond to a charge neutral 'chequer-board' pattern of Gdm^+ ions and chloride ions, as shown in figure 6.15. As the concentration is increased, water is removed from the system. This allows charged groups to get closer together, which strengthens the electrostatic interactions between them. As a result, at higher concentrations, inner layers are inaccessible even under high forces.

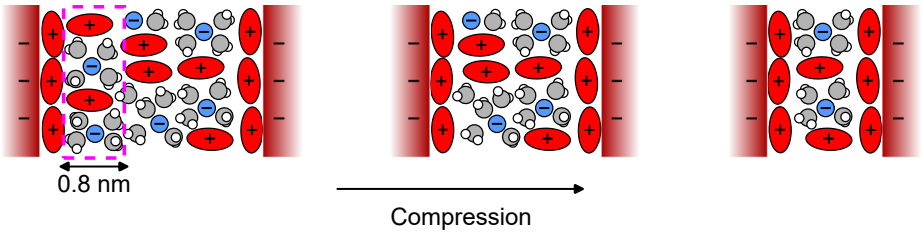


Figure 6.15: Cartoon showing a possible explanation for the origins of the structural forces observed at 3.30 and 6.06 m, as shown in figure 6.8. The squeeze out arises from of layers of 'chequer-board' Gdm^+ ions and hydrated Cl^- ions with a wavelength of ≈ 0.8 nm. As the concentration is increased, inner layers are held more tightly and become inaccessible.

6.4 | Summary

In summary, we have performed direct measurements of forces between charged surfaces across a range of denaturant concentrations in a basic model protein environment. We see forces that show strongly varying interactions across the concentration range measured, with significant differences between these observations and those made in similarly concentrated simple salts[57,59].

We propose mechanisms that give rise to these forces. We suggest that the unique hydration structure of the Gdm^+ ion leads to slow and

reversible evolution of the surface character at low concentration that leads to strongly varying force magnitudes. As the concentration is increased, the changing solvation environment of the cation speeds up adsorption to the surface. We also observe a long range force at all concentrations, which we propose is made possible by the presence of ion aggregates. We see evidence for the build up of a ‘chequer-board‘ type layering structure as the surface is left for long times or the salt concentration is increased.

These diverse behaviours likely arise from the dual character of the guanidinium cations, which can behave both as hydrophobic and as hydrophilic, depending on the location of the interaction about the guanidinium ion. The implication is that guanidinium chloride can influence the interactions within and between proteins across a wide range of concentrations in multiple and complex ways, driving misfolding and unfolding in different environments.

There remain many open questions as to the nature of interactions in solutions containing guanidinium ions, including the precise role played by aggregation in the observed interactions, the effect of confined guanidinium chloride solutions between hydrophobic surfaces, and the nature of the variation of the measured forces. However, it is clear that guanidinium ions show complex and varied behaviour that strongly modifies the interactions between charged surfaces, leading to the position of the ion as a strong protein denaturant in the Hofmeister series.

7 | Conclusions and Outlook

In this work, we have presented measurements investigating the forces and structures present in complex systems of high concentration electrolytes. Such systems remain poorly understood, yet are vital components in many modern technologies and play an important role in the chemistry of life. We have studied how these electrolytes behave close to surfaces using the surface force balance (SFB), and we have studied electrolytes in bulk environments using neutron scattering techniques. We have investigated aqueous water-in-salt (WiS) electrolytes and guanidinium chloride (GdmCl) solutions, and pure liquids and mixtures comprising solely of ions. Here, we briefly discuss our conclusions and the outlook from these investigations.

In chapter 3, we investigated the forces and structures present in confined films of the WiS electrolyte lithium bis(trifluoromethanesulfonyl)-imide, $LiNTf_2$. These salts are of interest both as model high concentration aqueous electrolytes and for their potential application in aqueous electrochemical energy storage devices with high energy density[26]. We found that the near-surface force behaviour of the electrolyte suggested the presence of a well defined, layered structure, similar to previous observations made in many other types of liquid[24,46,54,59,60,68–73]. The layers showed a wavelength of $\sim$ 1.5 nm across a wide range of concentrations, which is far larger than the individual ionic and molecular components of the solution. This leads to the suggestion that the liquid is able to organise into a nano-structure, in which there is a separation within the liquid into domains. We proposed a domain structure in which the water and majority of the lithium cations grouped together into a hydrated cation domain, while the anions and remaining cations

formed a non-aqueous anion domain.

In chapter 4, we continued to focus on $LiNTf_2$, now probing the bulk structure using elastic coherent neutron scattering techniques. These measurements revealed that the length scale of ~ 1.5 nm remained important in the bulk liquid, in agreement with previous small angle scattering work[167], suggesting that the domain structure observed at the surfaces was a consequence of an extensive domain network throughout the bulk. We used empirical potential structure refinement techniques within the Dissolve package to resolve the structure of the bulk liquid[39]. We found strong evidence for the existence of a domain structure, however the extent to which each domain was able to percolate fully through the bulk liquid, rather than exist as isolated pockets, was dependent on concentration. These results suggested that lithium ion transport must proceed via a mechanism by which they 'hop' from aqueous to anion domains rather than by a vehicular mechanism through the aqueous domains, in line with previous measurements[142]. We also showed that the wavelength of the domains remained largely unchanged between the 12 and 20 mol kg^{-1}, with the increased anions swelling the non-aqueous anion domains and thinning the hydrated cation domains but maintaining the ~ 1.5 nm correlation distance.

These results indicate the importance of hydrophilic and hydrophobic effects for the organisation and behaviour of ions in concentrated electrolytes. In the case of the WiS system studied here, it is the diverging affinity for water that drives the separation of the liquid into the observed domain structure. This is reminiscent of the microphase separation phenomena observed in antagonistic salts[270], in which the presence of salts with hydrophobic and hydrophilic ions prevent full phase separation in oil-water mixtures. It is the competition between the elec-

trostatic attraction between ions and the specific affinities of the ions that gives rise to these complex behaviours in high concentration electrolytes.

Ionic liquids are liquids composed solely of ions, and represent a clear departure from well understood theories of electrolytes. In chapter 5, we investigated the surface forces present in both pure and mixed ionic liquids to test whether surface properties of the resulting mixture could be optimised for specific applications. In the case of pure ionic liquids, we observed oscillating surface behaviour where the oscillation wavelength could be described by molecular arguments: for the short-chain ionic liquid [C_2C_1Im] [NTf_2], we saw evidence for well defined, alternating layers of cations and anions in an ABAB structure while for the long-chain ionic liquid [$C_{10}C_1$Im] [NTf_2] we saw a bilayer-type structure with charge rich domains and charge poor domains. We also saw a monotonically decaying exponential long range force, similar to the previously observed underscreening phenomenon[59,60,71,153–159]. We discussed how the structural and long range forces could arise from different decay modes within the pure liquids, as described in the recent work by Kjellander[165].

When investigating the ionic liquid mixtures, we saw far more complex forms of force profile, in which multiple correlation lengths appeared to be important. It is difficult to rationalise such force profiles in terms of the simple picture of stacks and layers of molecules and ions usually used to interpret surface force measurements. However, we found that these complex forces could be fitted through a linear combination of the oscillatory wave-like fits calculated for the pure ionic liquid components. This observation suggests that complex ionic mixtures can be described by considering wave superposition behaviour,

with multiple oscillatory modes required to describe observed forces that cannot be simply explained with molecular arguments. The mechanistic underpinnings of such phenomena are as yet unclear and it remains to be seen if such results can be reproduced in other mixtures, but these observations represent an exciting new insight into the behaviour of complex electrolyte mixtures.

The final experimental chapter, chapter 6, focused on the modifications to surface forces in the presence of high concentration aqueous guanidinium chloride, GdmCl. GdmCl solutions are used to denature proteins, however the mechanism by which these complex electrolytes achieve this is not well understood. We study a broad concentration range of GdmCl solutions using the SFB as a very basic model hydrophilic protein surface, and find a wide and varying array of behaviours that suggest great complexity in guanidinium-based ionic solutions. We observe a time dependence within our measurements at concentrations below 6 mol kg^{-1} that exceeds the $\sim$ 8 hour measurement time, which we suggest arises from a slowly developing surface charge. We also find evidence for long range interactions between surfaces enhanced by the possible presence of nano-scale ion aggregates. In total, these complex interactions between charged surfaces likely arise from the unique shape and charge distribution of the guanidinium ion, and the interplay between these features and the solvent. Such characteristics mean that guanidinium ions can show substantially different behaviours to those seen in salts containing simple spherical cations, as shown by the diverging activity coefficients between Gdm^+ salts and simple 1:1 aqueous salts (figure 6.4). It is these ion specific effects that allow for the denaturing behaviour seen in aqueous guanidinium chloride solutions.

Overall, our observations have shown the importance of considering specific ion effects when discussing concentrated electrolytes. While for electrolytes at infinite dilution, electrostatic interactions dominate, at higher concentrations, the unique properties of each ion can give rise to interactions that compete with and frustrate electrostatic effects, leading to a wide variety of complex properties and behaviours. This is an important strength of concentrated electrolytes: solutions can be designed and tuned in delicate ways to give desirable properties that cannot be predicted simply by considering the ion density. Such selection of ion specificity has been utilised by nature over evolutionary time scales, and now this information must be tuned to work for us in the design of new electrochemical technologies and applications.

Bibliography

[1] Pross, A. *What is Life?: How Chemistry Becomes Biology*; Oxford University Press.

[2] Bissantz, C.; Kuhn, B.; Stahl, M. *Journal of Medicinal Chemistry* **2010**, *53*, 5061–5084.

[3] Yadav, S.; Sharma, A. K.; Kumar, P. *Frontiers in Bioengineering and Biotechnology* **2020**, *8*, 127.

[4] Aurbach, D.; Markovsky, B.; Salitra, G.; Markevich, E.; Talyossef, Y.; Koltypin, M.; Nazar, L.; Ellis, B.; Kovacheva, D. *Journal of Power Sources* **2007**, *165*, 491–499.

[5] Encrenaz, T. *Annual Review of Astronomy and Astrophysics* **2008**, *46*, 57–87.

[6] Israelachvili, J. N. *Intermolecular and Surface Forces*, 3rd ed.; Academic Press.

[7] Debye, P.; Huckel, E. *Physikalische Zeitschrift* **1923**, *24*.

[8] Frank, H. S.; Thompson, P. T. *Journal of Chemical Physics* **1959**, *31*, 1086–1095.

[9] Kjellander, R. *Statistical Mechanics of Liquids and Solutions*; CRC Press, Vol. 1.

[10] Onsager, L. *Chemical Reviews* **1933**, *13*, 73–89.

[11] de Carvalho, R. L.; Evans, R. *Molecular Physics* **1994**, *83*, 619–654.

[12] Adar, R. M.; Safran, S. A.; Diamant, H.; Andelman, D. *Physical Review E* **2019**, *100*, 042615.

[13] Derjaguin, B.; Landau, L. *Progress in Surface Science* **1993**, *43*, 30–59.

[14] Verwey, E. J. W. *Journal of Physical and Colloid Chemistry* **1947**, *51*, 631–636.

[15] N., J.; Tabor, D. *Proceedings of the Royal Society of London. Series A, Mathematical and Physical Sciences* **1972**, *331*, 19–38.

[16] Israelachvili, J. N.; Adams, G. E. *Nature 262*, 774–776.

[17] Ducker, W. A.; Senden, T. J.; Pashley, R. M. *Langmuir* **1992**, *8*, 1831–1836.

[18] Ruiz-Cabello, F. J. M.; Maroni, P.; Borkovec, M. *Journal of Chemical Physics* **2013**, *138*, 234705.

[19] Yarnell, J. L.; Katz, M. J.; Wenzel, R. G.; Koenig, S. H. *Physical Review A* **1973**, *7*, 2130–2144.

[20] Pavlyukhin, Y. T. *Journal of Structural Chemistry* **2000**, *41*, 809–824.

[21] Brown, C. E.; Everett, D. H.; Powell, A. V.; Thorne, P. E. *Faraday Discussions of the Chemical Society* **1975**, *59*, 97–108.

[22] Horn, R. G.; Israelachvili, J. N. *Journal of Chemical Physics* **1981**, *75*, 1400–1411.

[23] Evans, R.; Henderson, J.; Hoyle, D.; Parry, A.; Sabeur, Z. *Molecular Physics* **1993**, *80*, 755–775.

[24] Smith, A. M.; Lovelock, K. R. J.; Perkin, S. *Faraday Discussions* **2013**, *167*, 279–292.
[25] Borodin, O.; Self, J.; Persson, K. A.; Wang, C.; Xu, K. *Joule* **2020**, *4*, 69–100.
[26] Suo, L.; Borodin, O.; Gao, T.; Olguin, M.; Ho, J.; Fan, X.; Luo, C.; Wang, C.; Xu, K. *Science* **2015**, *350*, 938–943.
[27] Niedermeyer, H.; Hallett, J. P.; Villar-Garcia, I. J.; Hunt, P. A.; Welton, T. *Chemical Society Reviews* **2012**, *41*, 7780–7802.
[28] Mao, X.; Brown, P.; Cervinka, C.; Hazell, G.; Li, H.; Ren, Y.; Chen, D.; Atkin, R.; Eastoe, J.; Padua, A. A. H.; Costa Gomes, M. F.; Hatton, T. A. *Nature Materials* **2019**, *18*, 1350–1357.
[29] Hofmeister, F. *Archiv für experimentelle Pathologie und Parmakologie* **1888**, *24*, 247–260.
[30] Kunz, W.; Lo Nostro, P.; Ninham, B. *Current Opinion in Colloid & Interface Science* **2004**, *9*, 1–18.
[31] Binnig, G.; Quate, C. F.; Gerber, C. *Physical Review Letters* **1986**, *56*, 930–933.
[32] Rutherford, E. *The London, Edinburgh, and Dublin Philosophical Magazine and Journal of Science* **1911**, *21*, 669–688.
[33] Metropolis, N.; Rosenbluth, A. W.; Rosenbluth, M. N.; Teller, A. H.; Teller, E. *Journal of Chemical Physics* **1953**, *21*, 1087–1092.
[34] Allen, M. P.; Tildesley, D. J. *Computer Simulation of Liquids*, 2nd ed.; Oxford University Press.
[35] Alder, B. J.; Ceperley, D. M.; Pollock, E. L. *Accounts of chemical research* **1985**, *18*, 268–273.
[36] Alder, B. J.; Wainwright, T. E. *Journal of Chemical Physics* **1957**, *27*, 1208–1209.
[37] Niethammer, C.; Becker, S.; Bernreuther, M.; Buchholz, M.; Eckhardt, W.; Heinecke, A.; Werth, S.; Bungartz, H.-J.; Glass, C. W.; Hasse, H.; Vrabec, J.; Horsch, M. *Journal of Chemical Theory and Computation* **2014**, *10*, 4455–4464.
[38] Piana, S.; Klepeis, J. L.; Shaw, D. E. *Current Opinion in Structural Biology* **2014**, *24*, 98–105.
[39] Youngs, T. *Molecular Physics* **2019**, *117*, 3464–3477.
[40] Bailey, A. I.; Courtney-Pratt, J. S. *Proceedings of the Royal Society of London. Series A. Mathematical and Physical Sciences* **1955**, *227*, 500–515.
[41] Tabor, D.; Winterton, R. H. S. *Proceedings of the Royal Society of London. A. Mathematical and Physical Sciences* **1969**, *312*, 435–450.
[42] Lin, W.; Klein, J. *Applied Physics Reviews* **2021**, *8*, 031316.
[43] Hayler, H. J.; Groves, T. S.; Guerrini, A.; Zheng, W.; Perkin, S. *In Preparation*.
[44] Christenson, H. K. *Journal of the Chemical Society, Faraday Transactions 1* **1984**, *80*, 1933–1946.
[45] Christenson, H. K.; Horn, R. G. *Journal of Colloid and Interface Science* **1985**, *103*, 50–55.

[46] Christenson, H.; Horn, R.; Israelachvili, J. *Journal of Colloid and Interface Science* **1982**, *88*, 79–88.
[47] Christenson, H. K. *Journal of Chemical Physics* **1983**, *78*, 6906–6913.
[48] Horn, R.; Israelachvili, J.; Perez, E. *Journal de Physique France* **1981**, *42*, 39–52.
[49] Idziak, S. H.; Safinya, C. R.; Hill, R. S.; Kraiser, K. E.; Ruths, M.; Warriner, H. E.; Steinberg, S.; Liang, K. S.; Israelachvili, J. N. *Science* **1994**, *264*, 1915–1918.
[50] Golan, Y.; Martin-Herranz, A.; Li, Y.; Safinya, C. R.; Israelachvili, J. *Physical Review Letters* **2001**, *86*, 1263–1266.
[51] Zheng, W.; Perez-Martinez, C. S.; Petriashvili, G.; Perkin, S.; Zappone, B. *Soft Matter* **2019**, *15*, 4905–4914.
[52] Israelachvili, J. N.; Adams, G. E. *Journal of the Chemical Society, Faraday Transactions 1* **1978**, *74*, 975–1001.
[53] McGuiggan, P. M.; Pashley, R. M. *Journal of Physical Chemistry* **1988**, *92*, 1235–1239.
[54] Pashley, R. *Journal of Colloid and Interface Science* **1981**, *80*, 153–162.
[55] Pashley, R. *Journal of Colloid and Interface Science* **1981**, *83*, 531–546.
[56] Israelachvili, J. N.; Pashley, R. *Nature* **1983**, *306*, 249–250.
[57] Pashley, R. M.; Israelachvili, J. N. *Journal of Colloid and Interface Science* **1984**, *101*, 511–523.
[58] Pashley, R.; Israelachvili, J. *Journal of Colloid and Interface Science* **1984**, *97*, 446–455.
[59] Baimpos, T.; Shrestha, B. R.; Raman, S.; Valtiner, M. *Langmuir* **2014**, *30*, 4322–4332.
[60] Smith, A. M.; Lee, A. A.; Perkin, S. *Journal of Physical Chemistry Letters* **2016**, *7*, 2157–2163.
[61] Hallett, J. E.; Agg, K. J.; Perkin, S. *Proceedings of the National Academy of Sciences* **2023**, *120*, e2215585120.
[62] Groves, T. S.; Perez-Martinez, C. S.; Lhermerout, R.; Perkin, S. *Journal of Physical Chemistry Letters* **2021**, *12*, 1702–1707.
[63] Han, M.; Zhang, R.; Gewirth, A. A.; Espinosa-Marzal, R. M. *Nano Letters* **2021**, *21*, 2304–2309.
[64] Hallett, J. E.; Hayler, H. J.; Perkin, S. *Physical Chemistry, Chemical Physics* **2020**, *22*, 20253–20264.
[65] Hayler, H. J. *Bulk and Surface Properties of Electrolytes at Eutectic Compositions*.
[66] Horn, R. G.; Evans, D. F.; Ninham, B. W. *Journal of Physical Chemistry* **1988**, *92*, 3531–3537.
[67] Perkin, S.; Albrecht, T.; Klein, J. *Physical Chemistry, Chemical Physics* **2010**, *12*, 1243–1247.
[68] Perkin, S.; Crowhurst, L.; Niedermeyer, H.; Welton, T.; Smith, A. M.; Gosvami, N. N. *Chemical Communications* **2011**, *47*, 6572–6574.

[69] Smith, A. M.; Lovelock, K. R. J.; Gosvami, N. N.; Licence, P.; Dolan, A.; Welton, T.; Perkin, S. *Journal of Physical Chemistry Letters* **2013**, *4*, 378–382.
[70] Espinosa-Marzal, R. M.; Arcifa, A.; Rossi, A.; Spencer, N. D. *Journal of Physical Chemistry Letters* **2014**, *5*, 179–184.
[71] Gebbie, M. A.; Dobbs, H. A.; Valtiner, M.; Israelachvili, J. N. *Proceedings of the National Academy of Sciences* **2015**, *112*, 7432–7437.
[72] Perez-Martinez, C. S.; Perkin, S. *Langmuir* **2019**, *35*, 15444–15450.
[73] Perez-Martinez, C. S.; Groves, T. S.; Perkin, S. *Journal of Physics: Condensed Matter* **2021**, *33*, 31LT02.
[74] Luengo, G.; Tsuchiya, M.; Heuberger, M.; Israelachvili, J. *Journal of Food Science* **1997**, *62*, 767–812.
[75] Giasson, S.; Israelachvili, J.; Yoshizawa, H. *Journal of Food Science* **1997**, *62*, 640–652.
[76] Klein, J.; Kumacheva, E. *Journal of Chemical Physics* **1998**, *108*, 6996–7009.
[77] Israelachvili, J. *Journal of Colloid and Interface Science* **1973**, *44*, 259–272.
[78] Israelachvili, J.; Pashley, R. *Journal of Colloid and Interface Science* **1984**, *98*, 500–514.
[79] Xiao, X.-D.; Liu, G.-y.; Charych, D. H.; Salmeron, M. *Langmuir* **1995**, *11*, 1600–1604.
[80] Horn, R. G.; Clarke, D. R.; Clarkson, M. T. *Journal of Materials Research* **1988**, *3*, 413–416.
[81] Horn, R.; Smith, D.; Haller, W. *Chemical Physics Letters* **1989**, *162*, 404–408.
[82] Ren, H.-Y.; Mizukami, M.; Kurihara, K. *Review of Scientific Instruments* **2017**, *88*, 095108.
[83] Chai, L.; Klein, J. *Langmuir* **2007**, *23*, 7777–7783.
[84] van Engers, C. D.; Balabajew, M.; Southam, A.; Perkin, S. *Review of Scientific Instruments* **2018**, *89*, 123901.
[85] Southam, A. *The Behaviour and Charging Dynamics of Concentrated Electrolytes in Confinement under Potential Control*.
[86] Britton, J.; Cousens, N. E. A.; Coles, S. W.; van Engers, C. D.; Babenko, V.; Murdock, A. T.; Koós, A.; Perkin, S.; Grobert, N. *Langmuir* **2014**, *30*, 11485–11492.
[87] van Engers, C. D.; Cousens, N. E. A.; Babenko, V.; Britton, J.; Zappone, B.; Grobert, N.; Perkin, S. *Nano Letters* **2017**, *17*, 3815–3821.
[88] Connor, J. N.; Horn, R. G. *Langmuir* **2001**, *17*, 7194–7197.
[89] Mizuno, H.; Luengo, G. S.; Rutland, M. W. *Langmuir* **2010**, *26*, 18909–18915.
[90] Israelachvili, J. N.; Alcantar, N. A.; Maeda, N.; Mates, T. E.; Ruths, M. *Langmuir* **2004**, *20*, 3616–3622.
[91] Perkin, S.; Chai, L.; Kampf, N.; Raviv, U.; Briscoe, W.; Dunlop, I.;

Titmuss, S.; Seo, M.; Kumacheva, E.; Klein, J. *Langmuir* **2006**, *22*, 6142–6152.
[92] Poppa, H.; Elliot, A. *Surface Science* **1971**, *24*, 149–163.
[93] Dowsett, M.; King, R.; Parker, E. *Journal of Vacuum Science and Technology* **1977**, *14*, 711–717.
[94] Christenson, H. K.; Thomson, N. H. *Surface Science Reports* **2016**, *71*, 367–390.
[95] Tolansky, S. *An Introduction to Interferometry*; Longmans, Green and Co Ltd.
[96] Chan, D. Y. C.; Horn, R. G. *The Journal of Chemical Physics* **1985**, *83*, 5311–5324.
[97] Chadwick, J. *Nature* **1932**, *129*, 312.
[98] Chadwick, J. *Proceedings of the Royal Society of London. A. Mathematical and Physical Sciences* **1932**, *136*, 692–708.
[99] Willis, B. T. M.; J., C. C. *Experimental Neutron Scattering*, 1st ed.; Oxford University Press.
[100] ISIS Neutron and Muon Source. `https://www.isis.stfc.ac.uk/Pages/home.aspx`.
[101] Young, T. *Philosophical Transactions of the Royal Society of London* **1804**, *94*, 1–16.
[102] Bragg, W. H.; Bragg, W. L. *Proceedings of the Royal Society of London. Series A, Containing Papers of a Mathematical and Physical Character* **1913**, *88*, 428–438.
[103] Narten, A. H.; Danford, M. D.; Levy, H. A. *Discussions of the Faraday Society* **1967**, *43*, 97–107.
[104] Kashyap, H. K.; Santos, C. S.; Annapureddy, H. V. R.; Murthy, N. S.; Margulis, C. J.; Castner, Jr, E. W. *Faraday Discussions* **2012**, *154*, 133–143.
[105] Benmore, C. J.; Neto, A. O.; Provis, J.; Benmore, C. J. *International Scholarly Research Notices* **2012**, *2012*, 852905–852924.
[106] De Broglie, Louis *Nature* **1923**, *112*, 540.
[107] De Broglie, Louis *Annales de Physique* **1925**, *10*, 22–128.
[108] Zeilinger, A.; Gähler, R.; Shull, C. G.; Treimer, W.; Mampe, W. *Reviews of Modern Physics* **1988**, *60*, 1067–1073.
[109] Bowron, D. T.; Soper, A. K.; Jones, K.; Ansell, S.; Birch, S.; Norris, J.; Perrott, L.; Riedel, D.; Rhodes, N. J.; Wakefield, S. R.; Botti, A.; Ricci, M.-A.; Grazzi, F.; Zoppi, M. *Review of Scientific Instruments* **2010**, *81*.
[110] Soper, A. K. GudrunN and GudrunX: programs for correcting raw neutron and X-ray diffraction data to differential scattering cross section.
[111] Young, T. *A course of lectures on natural philosophy and the mechanical arts*; Vol. 1.
[112] Tarascon, J. M.; Amrand, M. *Nature* **2001**, *414*, 259–367.
[113] Wagner, R.; Preschitschek, N.; Passerini, S.; Leker, J.; Winter, M. *Journal of Applied Electrochemistry* **2013**, *43*, 481–496.
[114] Kim, T.; Song, W.; Son, D.-Y.; Ono, L. K.; Qi, Y. *Journal of Materials*

Chemistry A **2019**, *7*, 2942–2964.
[115] Xu, K. *Chemical Reviews* **2004**, *104*, 4303–4418.
[116] Hammami, A.; Raymond, N.; Armand, M. *Nature* **2003**, *424*, 635–636.
[117] Goodenough, J. B.; Kim, Y. *Chemistry of Materials* **2010**, *22*, 587–603.
[118] Chen, Y.; Kang, Y.; Zhao, Y.; Wang, L.; Liu, J.; Li, Y.; Liang, Z.; He, X.; Li, X.; Tavajohi, N.; Li, B. *Journal of Energy Chemistry* **2021**, *59*, 83–99.
[119] Li, W.; Dahn, J. R.; Wainwright, D. S. *Science* **1994**, *264*, 1115–1118.
[120] Suo, L.; Borodin, O.; Sun, W.; Fan, X.; Yang, C.; Wang, F.; Gao, T.; Ma, Z.; Schroeder, M.; von Cresce, A.; Russell, S. M.; Armand, M.; Angell, A.; Xu, K.; Wang, C. *Angewandte Chemie International Edition* **2016**, *55*, 7136–7141.
[121] Yamada, Y.; Usui, K.; Sodeyama, K.; Ko, S.; Tateyama, Y.; Yamada, A. *Nature Energy* **2016**, *1*, 16129.
[122] Suo, L.; Han, F.; Fan, X.; Liu, H.; Xu, K.; Wang, C. *Journal of Materials Chemistry A* **2016**, *4*, 6639–6644.
[123] Yang, C.; Chen, J.; Qing, T.; Fan, X.; Sun, W.; von Cresce, A.; Ding, M. S.; Borodin, O.; Vatamanu, J.; Schroeder, M. A.; Eidson, N.; Wang, C.; Xu, K. *Joule* **2017**, *1*, 122–132.
[124] Ko, S.; Yamada, Y.; Miyazaki, K.; Shimada, T.; Watanabe, E.; Tateyama, Y.; Kamiya, T.; Honda, T.; Akikusa, J.; Yamada, A. *Electrochemistry Communications* **2019**, *104*, 106488.
[125] Jiang, L.; Liu, L.; Yue, J.; Zhang, Q.; Zhou, A.; Borodin, O.; Suo, L.; Li, H.; Chen, L.; Xu, K.; others *Advanced Materials* **2020**, *32*, 1904427.
[126] Kühnel, R.-S.; Reber, D.; Battaglia, C. *ACS Energy Letters* **2017**, *2*, 2005–2006.
[127] Suo, L.; Borodin, O.; Wang, Y.; Rong, X.; Sun, W.; Fan, X.; Xu, S.; Schroeder, M. A.; Cresce, A. V.; Wang, F.; Yang, C.; Hu, Y.-S.; Xu, K.; Wang, C. *Advanced Energy Materials* **2017**, *7*, 1701189.
[128] Leonard, D. P.; Wei, Z.; Chen, G.; Du, F.; Ji, X. *ACS Energy Letters* **2018**, *3*, 373–374.
[129] Li, Y.; Zhou, Z.; Deng, W.; Li, C.; Yuan, X.; Hu, J.; Zhang, M.; Chen, H.; Li, R. *ChemElectroChem* **2021**, *8*, 1451–1454.
[130] Pan, W.; Wang, Y.; Zhang, Y.; Kwok, H. Y. H.; Wu, M.; Zhao, X.; Leung, D. Y. *Journal of Materials Chemistry A* **2019**, *7*, 17420–17425.
[131] Wang, Y.; Pan, W.; Leong, K. W.; Xu, X.; Dong, G.; Ye, X.; Zhang, M.; Leung, D. Y. *Journal of Energy Storage* **2023**, *63*, 106983.
[132] Hu, P.; Yan, M.; Zhu, T.; Wang, X.; Wei, X.; Li, J.; Zhou, L.; Li, Z.; Chen, L.; Mai, L. *ACS Applied Materials & Interfaces* **2017**, *9*, 42717–42722.
[133] Kadam, N.; Sarkar, A. *Journal of Energy Storage* **2022**, *54*, 105265.

[134] Chen, M.; Feng, G.; Qiao, R. *Current Opinion in Colloid & Interface Science* **2020**, *47*, 99–110.
[135] Dubouis, N.; Lemaire, P.; Mirvaux, B.; Salager, E.; Deschamps, M.; Grimaud, A. *Energy & Environment Science* **2018**, *11*, 3491–3499.
[136] Quan, T.; Härk, E.; Xu, Y.; Ahmet, I.; Höhn, C.; Mei, S.; Lu, Y. *ACS Applied Materials & Interfaces* **2021**, *13*, 3979–3990.
[137] Vatamanu, J.; Borodin, O. *Journal of Physical Chemistry Letters* **2017**, *8*, 4362–4367.
[138] McEldrew, M.; Goodwin, Z. A. H.; Kornyshev, A. A.; Bazant, M. Z. *Journal of Physical Chemistry Letters* **2018**, *9*, 5840–5846.
[139] Patsahan, O.; Ciach, A. *ACS Omega* **2022**, *7*, 6655–6664.
[140] Ichii, T.; Ichikawa, S.; Yamada, Y.; Murata, M.; Utsunomiya, T.; Sugimura, H. *Japanese Journal of Applied Physics* **2020**, *59*, SN1003.
[141] Tsuyoshi, J.; Bao, Y.; Ichii, T.; Utsunomiya, T.; Sugimura, H. *Japanese Journal of Applied Physics* **2022**, *61*, SL1003.
[142] Zhang, R.; Han, M.; Ta, K.; Madsen, K. E.; Chen, X.; Zhang, X.; Espinosa-Marzal, R. M.; Gewirth, A. A. *ACS Applied Energy Materials* **2020**, *3*, 8086–8094.
[143] Mason, P.; Ansell, S.; Neilson, G.; Rempe, S. *Journal of Physical Chemistry B* **2015**, *119*, 2003–2009.
[144] Ding, M. S.; Xu, K. *Journal of Physical Chemistry C* **2018**, *122*, 16624–16629.
[145] Fisher, M. E.; Wiodm, B. *Journal of Chemical Physics* **1969**, *50*, 3756–3772.
[146] Attard, P. *Physical Review E* **1993**, *48*, 3604–3621.
[147] Lhermerout, R. *Lubricants* **2021**, *9*.
[148] Smith, A. M.; Hallett, J. E.; Perkin, S. *Proceedings of the National Academy of Sciences* **2019**, *116*, 25418–25423.
[149] Sakuma, H. *Journal of Geophysical Research: Solid Earth* **2013**, *118*, 6066–6075.
[150] Espinosa-Marzal, R. M.; Drobek, T.; Balmer, T.; Heuberger, M. P. *Physical Chemistry Chemical Physics* **2012**, *14*, 6085–6093.
[151] Bhargava, B. L.; Devane, R.; Klein, M. L.; Balasubramanian, S. *Soft Matter* **2007**, *3*, 1395–1400.
[152] Pott, T.; Méléard, P. *Physical Chemistry, Chemical Physics* **2009**, *11*, 5469–5475.
[153] Gebbie, M. A.; Valtiner, M.; Banquy, X.; Fox, E. T.; Henderson, W. A.; Israelachvili, J. N. *Proceedings of the National Academy of Sciences* **2013**, *110*, 9674–9679.
[154] Gebbie, M. A.; Smith, A. M.; Dobbs, H. A.; Warr, G. G.; Banquy, X.; Valtiner, M.; Rutland, M. W.; Israelachvili, J. N.; Perkin, S.; Atkin, R.; others *Chemical communications* **2017**, *53*, 1214–1224.
[155] Lee, A.; Perez-Martinez, C. S.; Smith, A. M.; Perkin, S. *Physical review letters* **2017**, *119*, 026002.
[156] Hjalmarsson, N.; Atkin, R.; Rutland, M. W. *Chemical Communica-*

tions **2017**, *53*, 647–650.
[157] Fung, C.; Perkin, S. *Faraday Discussions* **2023**, –.
[158] Gaddam, P.; Ducker, W. *Langmuir* **2019**, *35*, 5719–5727.
[159] Yuan, H.; Deng, W.; Zhu, X.; Liu, G.; Craig, V. S. J. *Langmuir* **2022**, *38*, 6164–6173.
[160] Lhermerout, R.; Perkin, S. *Physical Review Fluids* **2018**, *3*, 014201.
[161] Kumar, S.; Cats, P.; Alotaibi, M. B.; Ayirala, S. C.; Yousef, A. A.; van Roij, R.; Siretanu, I.; Mugele, F. *Journal of Colloid and Interface Science* **2022**, *622*, 819–827.
[162] Rotenberg, B.; Bernard, O.; Hansen, J.-P. *Journal of Physics: Condensed Matter* **2018**, *30*, 054005.
[163] Coles, S. W.; Park, C.; Nikam, R.; Kanduč, M.; Dzubiella, J.; Rotenberg, B. *Journal of Physical Chemistry B* **2020**, *124*, 1778–1786.
[164] Zeman, J.; Kondrat, S.; Holm, C. *Chemical Communications* **2020**, *56*, 15635–15638.
[165] Kjellander, R. *Soft Matter* **2019**, *15*, 5866–5895.
[166] Härtel, A.; Bültmann, M.; Coupette, F. *Physical Review Letters* **2023**, *130*, 108202.
[167] Borodin, O. et al. *ACS Nano* **2017**, *11*, 10462–10471.
[168] González, M. A.; Borodin, O.; Kofu, M.; Shibata, K.; Yamada, T.; Yamamuro, O.; Xu, K.; Price, D. L.; Saboungi, M.-L. *Journal of Physical Chemistry Letters* **2020**, *11*, 7279–7284.
[169] Triolo, A.; Di Lisio, V.; Lo Celso, F.; Appetecchi, G. B.; Fazio, B.; Chater, P.; Martinelli, A.; Sciubba, F.; Russina, O. *Journal of Physical Chemistry B* **2021**, *125*, 12500–12517.
[170] Tot, A.; Kloo, L. *Chemical Communications* **2022**, *58*, 9528–9531.
[171] Malaspina, T.; Colherinhas, G.; Weitzner, S. E.; Wood, B. C.; Eterno Fileti, E. *Journal of Molecular Liquids* **2023**, *383*, 122097.
[172] Zhang, Y.; Lewis, N. H. C.; Mars, J.; Wan, G.; Weadock, N. J.; Takacs, C. J.; Lukatskaya, M. R.; Steinrück, H.-G.; Toney, M. F.; Tokmakoff, A.; Maginn, E. J. *Journal of Physical Chemistry B* **2021**, *125*, 4501–4513.
[173] Zhang, Y.; Maginn, E. J. *Journal of Physical Chemistry B* **2021**, *125*, 13246–13254.
[174] González, M. A.; Akiba, H.; Borodin, O.; Cuello, G. J.; Hennet, L.; Kohara, S.; Maginn, E. J.; Mangin-Thro, L.; Yamamuro, O.; Zhang, Y.; Price, D. L.; Saboungi, M.-L. *Physical Chemistry, Chemical Physics* **2022**, *24*, 10727–10736.
[175] Liu, X.; Lee, S.-C.; Seifert, S.; He, L.; Do, C.; Winans, R. E.; Kwon, G.; Z, Y.; Li, T. *Chemistry of Materials* **2023**, *35*, 2088–2094.
[176] Dutta, R. C.; Bhatia, S. K. *Electrochimica Acta* **2023**, *462*, 142772.
[177] Kaplow, R.; Rowe, T. A.; Averbach, B. L. *Physical Reviews* **1968**, *168*, 1068–1079.
[178] Soper, A. K. *Physical Review B* **2005**, *72*, 104204.

[179] Alderman, O. L. G.; Hannon, A. C.; Holland, D.; Feller, S.; Lehr, G.; Vitale, A. J.; Hoppe, U.; Zimmerman, M. V.; Watenphul, A. *Physical Chemistry Chemical Physics* **2013**, *15*, 8506–8519.
[180] Soper, A. K. *International Scholarly Research Notices* **2013**, *2013*, 279463.
[181] McGregor, J.; Li, R.; Zeitler, J. A.; D'Agostino, C.; Collins, J. H. P.; Mantle, M. D.; Manyar, H.; Holbrey, J. D.; Falkowska, M.; Youngs, T. G. A.; Hardacre, C.; Stitt, E. H.; Gladden, L. F. *Physical Chemistry, Chemical Physics* **2015**, *17*, 30481–30491.
[182] Soper, A.; Edler, K. *Biochimica et Biophysica Acta (BBA) - General Subjects* **2017**, *1861*, 1652–1660.
[183] Miao, S.; Imberti, S.; Atkin, R.; Warr, G. *Journal of Molecular Liquids* **2022**, *351*, 118599.
[184] Laurent, H. S. T. *The Biological Role of Water in Extreme Conditions*.
[185] Pethes, I. *Journal of Molecular Liquids* **2017**, *242*, 845–858.
[186] Neumann, J.; Golub, B.; Odebrecht, L.-M.; Ludwig, R.; Paschek, D. *Journal of Chemical Physics* **2018**, *148*, 193828.
[187] Wu, Y.; Tepper, H. L.; Voth, G. A. *Journal of Chemical Physics* **2006**, *124*, 024503.
[188] Miao, S. *Structure, Dynamics, and Self-assembly in Ionic Liquids*.
[189] Lorenz, C. D.; Ziff, R. M. *Phys. Rev. E* **1998**, *57*, 230–236.
[190] Jan, N. *Physica A: Statistical Mechanics and its Applications* **1999**, *266*, 72–75.
[191] Koumakis, N.; Moghimi, E.; Besseling, R.; Poon, W. C. K.; Brady, J. F.; Petekidis, G. *Soft Matter* **2015**, *11*, 4640–4648.
[192] Welton, T. *Biophysical Reviews* **2018**, *10*, 691–706.
[193] Seddon, K. R. *Journal of Chemical Technology & Biotechnology* **1997**, *68*, 351–356.
[194] Welton, T. *Proceedings of the Royal Society A: Mathematical, Physical and Engineering Sciences* **2015**, *471*, 20150502.
[195] Swatloski, R. P.; Spear, S. K.; Holbrey, J. D.; Rogers, R. D. *Journal of the American Chemical Society* **2002**, *124*, 4974–4975.
[196] Kilpeläinen, I.; Xie, H.; King, A.; Granstrom, M.; Heikkinen, S.; Argyropoulos, D. S. *Journal of Agricultural and Food Chemistry* **2007**, *55*, 9142–9148.
[197] Brandt, A.; Gräsvik, J.; Hallett, J. P.; Welton, T. *Green Chemistry* **2013**, *15*, 550–583.
[198] Zeng, S.; , X.; Bai, L.; Zhang, X.; Wang, H.; Wang, J.; Bao, D.; Li, M.; Liu, X.; Zhang, S. *Chemical Reviews* **2017**, *117*, 9625–9673.
[199] Díaz, M.; Ortiz, A.; Ortiz, I. *Journal of Membrane Science* **2014**, *469*, 379–396.
[200] Watanabe, M.; Thomas, M. L.; Zhang, S.; Ueno, K.; Yasuda, T.; Dokko, K. *Chemical Reviews* **2017**, *117*, 7190–7239.
[201] Ye, C.; Liu, W.; Chen, Y.; Yu, L. *Chemical Communications* **2001**, 2244–2245.

[202] Smith, A. M.; Lovelock, K. R. J.; Gosvami, N. N.; Welton, T.; Perkin, S. *Physical Chemistry, Chemical Physics* **2013**, *15*, 15317–15320.
[203] Zhou, Y.; Qu, J. *ACS Applied Materials & Interfaces* **2017**, *9*, 3209–3222.
[204] Lei, Z.; Chen, B.; Koo, Y.-M.; MacFarlane, D. R. *Chemical Reviews* **2017**, *117*, 6633–6635.
[205] Newington, I.; Perez-Arlandis, J. M.; Welton, T. *Organic Letters* **2007**, *9*, 5247–5250.
[206] Greaves, T. L.; Drummond, C. J. *Chemical Reviews* **2008**, *108*, 206–237.
[207] Mecerreyes, D. *Progress in Polymer Science* **2011**, *36*, 1629–1648.
[208] Smith, E. L.; Abbott, A. P.; Ryder, K. S. *Chemical Reviews* **2014**, *114*, 11060–11082.
[209] Eyckens, D. J.; Henderson, L. C. *Frontiers in chemistry* **2019**, *7*, 263.
[210] Canongia Lopes, J. N. A.; Pádua, A. A. H. *Journal of Physical Chemistry B* **2006**, *110*, 3330–3335.
[211] Triolo, A.; Russina, O.; Bleif, H.-J.; Di Cola, E. *Journal of Physical Chemistry B* **2007**, *111*, 4641–4644.
[212] Annapureddy, H. V. R.; Kashyap, H. K.; De Biase, P. M.; Margulis, C. J. *Journal of Physical Chemistry B* **2010**, *114*, 16838–16846.
[213] Santos, C. S.; Murthy, N. S.; Baker, G. A.; Castner, J., Edward W. *Journal of Chemical Physics* **2011**, *134*, 121101.
[214] Atkin, R.; Warr, G. G. *Journal of Physical Chemistry C* **2007**, *111*, 5162–5168.
[215] Mezger, M.; Schröder, H.; Reichert, H.; Schramm, S.; Okasinski, J. S.; Schöder, S.; Honkimäki, V.; Deutsch, M.; Ocko, B. M.; Ralston, J.; Rohwerder, M.; Stratmann, M.; Dosch, H. *Science* **2008**, *322*, 424–428.
[216] Griffin, L. R.; Browning, K. L.; Clarke, S. M.; Smith, A. M.; Perkin, S.; Skoda, M. W. A.; Norman, S. E. *Physical Chemistry, Chemical Physics* **2017**, *19*, 297–304.
[217] Lux, S. F.; Schmuck, M.; Appetecchi, G. B.; Passerini, S.; Winter, M.; Balducci, A. *Journal of Power Sources* **2009**, *192*, 606–611.
[218] Castiglione, F.; Raos, G.; Battista Appetecchi, G.; Montanino, M.; Passerini, S.; Moreno, M.; Famulari, A.; Mele, A. *Physical Chemistry, Chemical Physics* **2010**, *12*, 1784–1792.
[219] Chatel, G.; Pereira, J. F. B.; Debbeti, V.; Wang, H.; Rogers, R. D. *Green Chemistry* **2014**, *16*, 2051–2083.
[220] Canongia Lopes, J. N.; Cordeiro, T. C.; Esperança, J. M. S. S.; Guedes, H. J. R.; Huq, S.; Rebelo, L. P. N.; Seddon, K. R. *Journal of Physical Chemistry B* **2005**, *109*, 3519–3525.
[221] Montanino, M.; Moreno, M.; Alessandrini, F.; Appetecchi, G.; Pas-

serini, S.; Zhou, Q.; Henderson, W. *Electrochimica Acta* **2012**, *60*, 163–169.
[222] Jarosik, A.; Krajewski, S. R.; Lewandowski, A.; Radzimski, P. *Journal of Molecular Liquids* **2006**, *123*, 43–50.
[223] Navia, P.; Troncoso, J.; Romani, L. *Journal of Solution Chemistry* **2009**, *37*, 677–688.
[224] Xiao, D.; Rajian, J. R.; Li, S.; Bartsch, R. A.; Quitevis, E. L. *Journal of Physical Chemistry B* **2006**, *110*, 16174–16178.
[225] Shimizu, K.; Tariq, M.; Rebelo, L. P.; Lopes, J. N. C. *Journal of Molecular Liquids* **2010**, *153*, 52–56.
[226] Andanson, J.-M.; Beier, M. J.; Baiker, A. *Journal of Physical Chemistry Letters* **2011**, *2*, 2959–2964.
[227] Tariq, M.; Forte, P.; Gomes, M. C.; Lopes, J. C.; Rebelo, L. *Journal of Chemical Thermodynamics* **2009**, *41*, 790–798.
[228] Ionic Liquid Data. `https://iolitec.de/en/products/ionic_liquids/catalogue`.
[229] Huang, M.-M.; Jiang, Y.; Sasisanker, P.; Driver, G. W.; Weingärtner, H. *Journal of Chemical & Engineering Data* **2011**, *56*, 1494–1499.
[230] Greenstein, J. P. *Journal of Biological Chemistry* **1938**, *125*, 501–513.
[231] Kunz, W.; Henle, J.; Ninham, B. *Current Opinion in Colloid & Interface Science* **2004**, *9*, 19–37.
[232] gellhorn, e. *Protoplasma* **1933**, *18*, 411–419.
[233] Zhang, Y.; Cremer, P. S. *Current Opinion in Chemical Biology* **2006**, *10*, 658–663.
[234] Lo Nostro, P.; Ninham, B. W. *Chemical Reviews* **2012**, *112*, 2286–2322.
[235] Okur, H. I.; Hladílková, J.; Rembert, K. B.; Cho, Y.; Heyda, J.; Dzubiella, J.; Cremer, P. S.; Jungwirth, P. *Journal of Physical Chemistry B* **2017**, *121*, 1997–2014.
[236] Wan, L. S.; Poon, P. K. *Journal of Pharmaceutical Sciences* **1969**, *58*, 1562–1567.
[237] dos Santos, A. P.; Diehl, A.; Levin, Y. *Langmuir* **2010**, *26*, 10778–10783.
[238] Roy, J. C. *Journal of Solution Chemistry* **2019**, *48*, 758–773.
[239] Zhang, Y.; Furyk, S.; Bergbreiter, D. E.; Cremer, P. S. *Journal of the American Chemical Society* **2005**, *127*, 14505–14510.
[240] Humphreys, B. A.; Willott, J. D.; Murdoch, T. J.; Webber, G. B.; Wanless, E. J. *Physical Chemistry, Chemical Physics* **2016**, *18*, 6037–6046.
[241] Lo Nostro, P.; Fratoni, L.; Ninham, B. W.; Baglioni, P. *Biomacromolecules* **2002**, *3*, 1217–1224.
[242] Ball, P. *Faraday Discussions* **2013**, *160*, 405–414.
[243] Jungwirth, P.; Cremer, P. S. *Nature Chemistry* **2014**, *6*, 261–263.
[244] Pollard, T. P.; Beck, T. L. *Current Opinion in Colloid & Interface Science* **2016**, *23*, 110–118.

[245] Gregory, K. P.; Elliott, G. R.; Robertson, H.; Kumar, A.; Wanless, E. J.; Webber, G. B.; Craig, V. S. J.; Andersson, G. G.; Page, A. J. *Physical Chemistry, Chemical Physics* **2022**, *24*, 12682–12718.
[246] Spombe Pop2p Protein Structure. https://commons.wikimedia.org/wiki/File:Spombe_Pop2p_protein_structure_rainbow.png.
[247] Mason, P. E.; Neilson, G. W.; Dempsey, C. E.; Barnes, A. C.; Cruickshank, J. M. *Proceedings of the National Academy of Sciences* **2003**, *100*, 4557–4561.
[248] Haas, D. J.; Harris, D. R.; Mills, H. H. *Acta Crystallographica* **1965**, *19*, 676–679.
[249] Mason, P. E.; Neilson, G. W.; Enderby, J. E.; Saboungi, M.-L.; Dempsey, C. E.; MacKerell, A. D. J.; Brady, J. W. *Journal of the American Chemical Society* **2004**, *126*, 11462–11470.
[250] Hunger, J.; Niedermayer, S.; Buchner, R.; Hefter, G. *Journal of Physical Chemistry B* **2010**, *114*, 13617–13627.
[251] Bonner, O. *Journal of Chemical Thermodynamics* **1976**, *8*, 1167–1172.
[252] Hamer, W. J.; Wu, Y. *Journal of Physical and Chemical Reference Data* **2009**, *1*, 1047–1100.
[253] Boudon, S.; Wipff, G.; Maigret, B. *Journal of Physical Chemistry* **1990**, *94*, 6056–6061.
[254] Vazdar, M.; Vymětal, J.; Heyda, J.; Vondrášek, J.; Jungwirth, P. *Journal of Physical Chemistry A* **2011**, *115*, 11193–11201.
[255] Shih, O.; England, A. H.; Dallinger, G. C.; Smith, J. W.; Duffey, K. C.; Cohen, R. C.; Prendergast, D.; Saykally, R. J. *Journal of Chemical Physics* **2013**, *139*, 035104.
[256] Inagaki, T.; Aono, S.; Nakano, H.; Yamamoto, T. *Journal of Physical Chemistry B* **2014**, *118*, 5499–5508.
[257] Sumowski, C. V.; Schmitt, B. B. T.; Schweizer, S.; Ochsenfeld, C. *Angewandte Chemie International Edition* **2010**, *49*, 9951–9955.
[258] Gordon, J. A. *Biochemistry* **1972**, *11*, 1862–1870.
[259] Dunbar, J.; Yennawar, H. P.; Banerjee, S.; Luo, J.; Farber, G. K. *Protein Science* **1997**, *6*, 1727–1733.
[260] Azuaga, A. I.; Canet, D.; Smeenk, G.; Berends, R.; Titgemeijer, F.; Duurkens, R.; Mateo, P. L.; Scheek, R. M.; Robillard, G. T.; Dobson, C. M.; van Nuland, N. A. J. *Biochemistry* **2003**, *42*, 4883–4895.
[261] Watlaufer, D. B.; Malik, S. K.; Stoller, L.; Coffin, R. L. *Journal of the American Chemical Society* **1964**, *86*, 508–514.
[262] Godawat, R.; Jamadagni, S. N.; Garde, S. *Journal of Physical Chemistry B* **2010**, *114*, 2246–2254.
[263] England, J. L.; Pande, V. S.; Haran, G. *Journal of the American Chemical Society* **2008**, *130*, 11854–11855.
[264] Breslow, R.; Guo, T. *Proceedings of the National Academy of Sciences* **1990**, *87*, 167–169.

[265] Mason, P. E.; Brady, J. W.; Neilson, G. W.; Dempsey, C. E. *Biophysical Journal* **2007**, *93*, L04–L06.
[266] Lim, W. K.; Rösgen, J.; Englander, S. W. *Proceedings of the National Academy of Sciences* **2009**, *106*, 2595–2600.
[267] Nozaki, Y. *Enzyme Structure, Part C*; Methods in Enzymology; Academic Press, 1972; Vol. 26; pp 43–50.
[268] Raviv, U.; Laurat, P.; Klein, J. *Journal of Chemical Physics* **2002**, *116*, 5167–5172.
[269] Nightingale Jr, E. *Journal of Physical Chemistry* **1959**, *63*, 1381–1387.
[270] Tasios, N.; Samin, S.; van Roij, R.; Dijkstra, M. *Physical Review Letters* **2017**, *119*, 218001.